

This is to certify that the

dissertation entitled

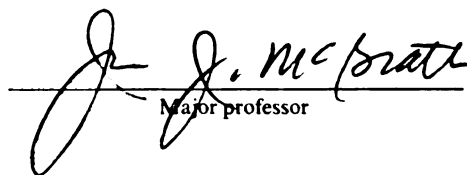
Fluorescent Emission Ratio Imaging Thermography and
Its Applications in Heat Transfer Analysis

presented by

Bin Lian

has been accepted towards fulfillment
of the requirements for

Ph.D. degree in Mechanical Engineering


Major professor

Date 8/24/99

LIBRARY
Michigan State
University

PLACE IN RETURN BOX to remove this checkout from your record.
TO AVOID FINES return on or before date due.
MAY BE RECALLED with earlier due date if requested.

DATE DUE	DATE DUE	DATE DUE

Fluorescent Emission Ratio Imaging Thermography and Its Application
in Heat Transfer Analysis

By

Bin Lian

A DISSERTATION

Submitted to
Michigan State University
in partial fulfillment of the requirements
for the degree of

DOCTOR OF PHILOSOPHY

Department of Mechanical Engineering

1999

ABSTRACT

Fluorescent Emission Ratio Imaging Thermography and Its Application in Heat Transfer Analysis

By

Bin Lian

This research seeks to develop and evaluate the fluorescent imaging thermographic technique for applications in surface temperature measurements. As opposed to two other thermographic technologies - the infrared and liquid crystal methods, fluorescent thermography has not been studied systematically even though some progress has been made in the last twenty years. This research investigated the technique with respect to several important aspects that determine its performance, which include imaging equipment characterization, test condition evaluation and temperature rendering. Windows-based custom application software has been successfully developed for integrating necessary tasks to obtain surface temperature distribution, including imaging, processing, and temperature rendering. Through this study, potential advantages of the fluorescent thermographic techniques are assessed in terms of temperature and spatial resolution, cost, operating convenience and other factors, as compared with infrared and liquid crystal techniques. The new system was shown to be advantageous over the infrared method in cost and spatial resolution, as well as data interpretation. It has wider operating range than the liquid crystal method and is more convenient to apply to the surface. This work also demonstrated the advantages of the new probe/solvent

system for improved photo-bleaching behavior which is a drawback for systems previously developed. In addition, a better calibration model and an efficient temperature rendering algorithm improve the fluorescent emission imaging technique from its previous qualitative/semi-quantitative nature to a truly quantitative method. The contributing factors to the measurement accuracy of the fluorescent thermographic technique were identified and estimated. Recommendations were made for configuring such a system including defining the required equipment and test conditions for given constraints of costs and performance criteria. This technique was successfully tested in several heat transfer applications to demonstrate its capabilities.

Copyright by

Bin Lian

1999

To my wife Bing, and my parents

ACKNOWLEDGMENTS

I would like to thank my advisor, Dr. John McGrath, for his invaluable guidance and constant support, for his encouragement, and for allowing me to freely develop my academic and professional skills in the duration of this study.

I would like to thank my committee members for their insightful guidance, advice and assistance. Dr. Blanchard and Dr. Scranton for their advice on chemical related work and their generosity for allowing me to use their facilities. Dr. Engeda, Dr. Somerton and Dr. Reinhard for their invaluable advice along the way.

I am grateful for having the opportunity to work with many graduate students and for their aide: Julie Pepper, Heidi Relyea, Paul Hoke, Gloria Elliot, Al Aksan, Qingtian Wang. I would like to thank Jeff Wille for his help in the early stage of my graduate research, Bo Zhang, Yang Wang, Qing Yang, Weiqing Zhong, Jing Wang, Nengjiu, Ju, Bing Ren, Jun Sheng, Qun Jiang and many other fellows who made my stay at MSU a joyful experience.

Especially, I would like to thank my wife Bing, whom I love more than she can imagine, for her love and support in the duration of this dissertation. I would also like to thank my parents and grandparents for encouraging me to continuously pursue academic excellence.

I would also like to thank the Composite Materials and Structures Center of Michigan State University for its support.

TABLE OF CONTENTS

TABLE OF CONTENTS.....	VII
LIST OF TABLES.....	XII
LIST OF FIGURES	XIII
LIST OF ABBREVIATIONS.....	XVIII
INTRODUCTION	1
CHAPTER 1	4
REVIEW OF THERMAL INSTRUMENTATION.....	4
1.1 Single Point Measurement Devices	4
1.1.1 Thermocouples	4
1.1.2 RTD Thermometer	6
1.2 Thermographic Instruments	7
1.2.1 Infrared Thermal Imaging	7
1.2.2 Liquid Crystal Thermography	15
1.2.3 Fluorescent/Phosphorescent Thermography	17
1.3 Description of Current Technique (FERIT)	21
CHAPTER 2	28
REVIEW OF FLUORESCENCE BASED THERMOGRAPHY.....	28
2.1 Theory of Molecular Fluorescent Emissions	28

CHAPTER 3	35
SYSTEM DEVELOPMENT.....	35
3.1 Temperature-Sensitive Fluorescent Probe	35
3.2 Coating Techniques	36
3.2.1 Brushes, Pads, and Hand Rollers.....	36
3.2.2 Spray Application.....	37
3.2.3 Electrostatic Spraying	39
3.3 Solvent-Based Fluorescent Film Fabrication	39
3.4 Fluorescent Imaging System	41
3.5 System Characterization	43
3.5.1 Noise Characteristics of ORBIS Cooled Digital Camera	43
3.5.2 Linearity Study of UV Excitation and Fluorescent Intensity	45
3.5.3 Photo Bleaching Study	45
3.5.4 Influence of Moisture	46
3.5.5 Effects of Quenching.....	46
3.5.6 Reproducibility.....	47
3.5.7 Effect of Fluorescent Probe Concentration	47
3.5.8 Aging Effect	48
3.5.9 System Dynamic Response	48
3.6 Custom Software Development	49
3.7 Algorithm for Temperature Rendering	53
CHAPTER 4	59
RESULTS AND DISCUSSION.....	59
4.1 CCD Camera Characterizations	59
4.1.1 CCD Read Noise Characterization	59

4.1.2	CCD Dark Noise Characterization	61
4.1.3	Shot Noise	65
4.2	UV Light Source Characterization	66
4.3	Photo-Bleaching Study	69
4.4	Linearity Study of UV Excitation and Fluorescent Emission Intensity	71
4.5	Calibration Curve for Fluorescent Emission Intensity and Temperature	75
4.6	Estimate of Temperature Measurement Errors	81
4.7	Moisture Effects	87
4.8	Reproducibility Study	90
4.8.1	Reproducibility between Neighboring Pixels	90
4.8.2	Reproducibility Tests Before and After Annealing	92
4.8.3	Hysteresis	95
4.9	Annealing Effects	96
4.10	Effect of Fluorescent Probe Concentration	97
4.11	Aging Effect	100
4.12	System Dynamic Response	100
CHAPTER 5	104
APPLICATIONS	104
5.1	Temperature Distribution of Fin Cooled by Natural Convection	104
5.2	Temperature Distribution of Micro-Structure by Joule Heating	108
5.3	Non-Destructive Evaluation	121
CHAPTER 6	126
RECOMMENDATIONS	126
6.1	System Considerations	126

6.1.1	Camera	126
6.1.2	UV Source	134
6.1.3	Photodiode.....	134
6.1.4	Total System Cost	135
6.2	The Influence of Film, Surface Dimension, and UV Intensity	135
6.2.1	Fluorescent Films	136
6.2.2	Optical Consideration	137
6.2.3	UV Intensity	139
CHAPTER 7		140
FUTURE WORK.....		140
7.1	Application Extensions	140
7.2	Fluorescent Probes for Low and High Temperature Applications	142
7.3	Further Study in Microscopic Scale	143
CHAPTER 8		145
CONCLUSIONS.....		145
APPENDICES		148
APPENDIX A.....		149
PROCEDURES FOR SYNTHESIS OF TEMPERATURE SENSITIVE PROBE		149
APPENDIX B		150
FLUORESCENT FILM FABRICATION		150
APPENDIX C		152
SYSTEM ELECTRONICS WIRING DIAGRAM.....		152

APPENDIX D.....	154
PHOTO-DETECTOR AND WIRING DIAGRAM.....	154
Burr-Brown Integrated Photodiode and Amplifier – Model OPT301M	154
APPENDIX E	156
ERROR OF MATHEMATICAL MODEL.....	156
APPENDIX F.....	158
EXCITATION FILTER AND ADAPTER	158
APPENDIX G.....	160
EMISSION FILTER AND ADAPTER	160
APPENDIX H.....	161
CALIBRATION BLOCK FOR THERMOCOUPLES.....	161
APPENDIX I	162
SOFTWARE USER’S GUIDE	162
FERIT – An Imaging, Temperature Rendering and Visualization Software	162
TCDAQ – A Temperature Measurement Virtual Instrument	167
DAQ – A General Purpose Data Acquisition Virtual Instrument	171
APPENDIX J	176
INSTRUCTIONS FOR TEMPERATURE MEASUREMENT WITH FERIT	176

LIST OF TABLES

Table 1. Dark Signals of CCD Sensor at Different Exposure Time.	61
Table 2. Transmittance and Optical Density of Neutral Density Filters.	71
Table 3. Temperature Measurement Difference at Different Temperature Ranges.	107
Table 4. Digital Camera Manufacturers.	131
Table 5. Dynamic Response as a Function of Film Thickness.	135
Table 6. Errors of Polynomial Fits.	156

LIST OF FIGURES

FIGURE 1. THERMOCOUPLE TEMPERATURE MEASUREMENT.....	5
FIGURE 2. PIXEL ELEMENT OF MICROBOLOMETER ARRAYS.....	13
FIGURE 3. JABLONSKI DIAGRAM. DEACTIVATION PROCESSES FOR AN EXCITED MOLECULE. A: ABSORPTION; B: VIBRATIONAL RELAXATION; C: INTERNAL CONVERSION; D: FLUORESCENCE; E: EXTERNAL CONVERSION; F: INTERSYSTEM CROSSING; G: PHOSPHORESCENCE.	29
FIGURE 4. FLUORESCENT EMISSION INTENSITY AS A FUNCTION OF TEMPERATURE FOR EU(HFA) ₃	31
FIGURE 5. FLUORESCENT EMISSION INTENSITY AS A FUNCTION OF EXCITATION INTENSITY.	33
FIGURE 6. TEMPERATURE SENSITIVE FLUORESCENT PROBE.....	35
FIGURE 7. CROSS-SECTIONAL VIEW OF AIRBRUSH.	38
FIGURE 8. FLUORESCENT FILM FORMING PROCESS: (A) INITIAL SOLVENT EVAPORATION AND DIFFUSION; (B) INTERMEDIATE STEP; (C) SOLID FILM FORMATION.....	40
FIGURE 9. FERIT SYSTEM SCHEMATIC.	41
FIGURE 10. STRUCTURE OF CUSTOM DEVELOPED APPLICATION SOFTWARE FOR FERIT. .	50
FIGURE 11. FERIT APPLICATION SOFTWARE INTERFACE.....	51
FIGURE 12. CALIBRATION DATA AND TEMPERATURE DETERMINATION.....	58
FIGURE 13. FLOW CHART FOR TEMPERATURE DETERMINATION.	58
FIGURE 14. CCD DARK NOISE AS A FUNCTION OF EXPOSURE TIME.	62

FIGURE 15. DARK NOISE: COMPARISON OF EXPERIMENTAL DATA AND LINEAR MODEL. .	63
FIGURE 16. ORBIS CAMERA SHOT NOISE (DETECTOR UNIT).	65
FIGURE 17. LONG AND SHORT TERM STABILITY OF 100W NIKON MERCURY LAMP.	68
FIGURE 18. LONG TERM AND SHORT TERM STABILITY OF OPTI-QUIP XENON/MERCURY LAMP.	69
FIGURE 19. FLUORESCENT EMISSION INTENSITY AS A FUNCTION OF TIME.	71
FIGURE 20. EXPERIMENTAL STUDY OF LINEARITY BETWEEN FLUORESCENT EMISSION AND UV EXCITATION.	72
FIGURE 21. FLUORESCENT EMISSION INTENSITIES AS A FUNCTION OF UV EXCITATION INTENSITIES.	73
FIGURE 22. CALIBRATION RIG.	76
FIGURE 23. SETUP FOR THERMOCOUPLE CALIBRATION.	77
FIGURE 24. ATTACHMENT METHODS FOR THERMOCOUPLES.	78
FIGURE 25. THERMAL RESISTIVE NETWORK REPRESENTATION OF CALIBRATION BLOCK. .	79
FIGURE 26. CALIBRATION FOR FLUORESCENT EMISSION AS A FUNCTION OF TEMPERATURE.	81
FIGURE 27. COMPARISON OF MEASUREMENT ERRORS AND ERROR ESTIMATE MODEL.	84
FIGURE 28. SCHEMATIC OF MOISTURE EFFECT EXPERIMENT.	88
FIGURE 29. MOISTURE EFFECT ON FLUORESCENT EMISSION INTENSITY.	89
FIGURE 30. MEASUREMENT LOCATIONS FOR NEIGHBORING PIXELS.	90
FIGURE 31. REPRODUCIBILITY AMONG NEIGHBORING TEN PIXELS.	91
FIGURE 32. REPRODUCIBILITY OF CALIBRATION RELATION BEFORE ANNEALING.....	92
FIGURE 33. REPRODUCIBILITY OF CALIBRATION RELATION AFTER ANNEALING.....	93

FIGURE 34. EFFECT OF ANNEALING.	95
FIGURE 35. FLUORESCENT EMISSION AS A FUNCTION OF TEMPERATURE FOR A HEAT-UP AND COOL-DOWN PROCESS.....	96
FIGURE 36. CALIBRATION FOR FLUORESCENT FILM OF 50WT% CONCENTRATION.	98
FIGURE 37. CALIBRATION FOR FLUORESCENT FILM OF 12.5WT% CONCENTRATION.	99
FIGURE 38. EFFECT OF TEMPERATURE PROBE CONCENTRATION.	100
FIGURE 39. DYNAMIC RESPONSE EXPERIMENT.....	101
FIGURE 40. TIME-DEPENDENT SURFACE TEMPERATURES - PULSE PERIOD = 10.0s.....	102
FIGURE 41. TIME-DEPENDENT SURFACE TEMPERATURES - PULSE PERIOD = 5.0s.....	102
FIGURE 42. TIME-DEPENDENT SURFACE TEMPERATURES - PULSE PERIOD = 1.0s.....	103
FIGURE 43. EXTENDED SURFACE COOLED BY NATURAL CONVECTION.	104
FIGURE 44. TEMPERATURE DISTRIBUTION ALONG ALUMINUM FIN - $T_{\text{BASE}} = 40^{\circ}\text{C}$	105
FIGURE 45. TEMPERATURE DISTRIBUTION ALONG ALUMINUM FIN - $T_{\text{BASE}} = 80^{\circ}\text{C}$	106
FIGURE 46. COMPARISON OF TC AND FERIT MEASUREMENTS.	107
FIGURE 47. UCB MICROSTRUCTURE (COURTESY OF PROF. A. MAJUMDAR OF UC BERKELEY).	109
FIGURE 48. SCHEMATIC OF MICROSCOPIC HEATING STUDY OF UCB MICROSTRUCTURE ON A NIKON INVERTED MICROSCOPE.	110
FIGURE 49. FLUORESCENT INTENSITY DISTRIBUTION OF MICROSTRUCTURE AT UNIFORM ROOM TEMPERATURE (IMAGE FILE: REF.TIF).	111
FIGURE 50. TEMPERATURE DISTRIBUTION OF ITO MICROSTRUCTURE MEASURED BY FERIT AT $T=1.0\text{s}$	112

FIGURE 51. TEMPERATURE DISTRIBUTION OF ITO MICROSTRUCTURE MEASURED BY FERIT AT T=8.0s.	112
FIGURE 52. TEMPERATURE DISTRIBUTION OF ITO MICROSTRUCTURE MEASURED BY FERIT AT T=15.0s.	113
FIGURE 53. FINITE ELEMENT MODEL FOR ITO STRUCTURES.	114
FIGURE 54. COMPARISON OF TEMPERATURE DISTRIBUTION - FERIT AND ANSYS54 AT T=1.0s.....	115
FIGURE 55. COMPARISON OF TEMPERATURE DISTRIBUTION - FERIT AND ANSYS54 AT T=8.0s.....	115
FIGURE 56. COMPARISON OF TEMPERATURE DISTRIBUTION - FERIT AND ANSYS54 AT T=15.0s.....	116
FIGURE 57. SURFACE TEMPERATURE DISTRIBUTION AT T=15.0s (SIMULATION - ANSYS54).	116
FIGURE 58. EMISSIVITY MAP OF ITO STRUCTURE.....	118
FIGURE 59. TEMPERATURE DISTRIBUTIONS MEASURED BY INFRARED METHOD.....	120
FIGURE 60. PRODUCT DEFECTS OF REACTION-INJECTION-MOLDED COMPOSITES.....	122
FIGURE 61. COMPOSITE SURFACE TEMPERATURE DISTRIBUTION AT T = 0.0s.	123
FIGURE 62. COMPOSITES SURFACE TEMPERATURE DISTRIBUTION AT T = 21 s.....	124
FIGURE 63. COMPOSITES SURFACE TEMPERATURE DISTRIBUTION AT T = 45.5 s.....	124
FIGURE 64. FRAME CYCLE OF FULL FRAME DEVICE.....	127
FIGURE 65. FRAME CYCLE OF FRAME TRANSFER DEVICE.	129
FIGURE 66. WIRING DIAGRAM FOR OPT301M INTEGRATED PHOTODIODE AND AMPLIFIER.	155

FIGURE 67. SPECTRAL TRANSMITTANCE OF EXCITATION FILTER (UV).....	158
FIGURE 68. SPECTRAL TRANSMITTANCE OF RED FILTER (620NM).	160

LIST OF ABBREVIATIONS

CCD:	Charge Coupled Device
DAQ:	Data Acquisition
DU:	Detector Unit
FERIT:	Fluorescent Emission Ratio Imaging Thermography
FF:	Full Frame
FT:	Frame Transfer
IR:	Infrared
LC:	Liquid Crystal
QE:	Quantum Efficiency
RTD:	Resistance Temperature Detector
TC:	Thermocouple
TEC:	Thermal-Electric Cooling
UV:	Ultra-Violet

INTRODUCTION

Thermal instrumentation has been playing a vital role in energy-related industries and advancement in this area is expected to favorably impact virtually all seven areas identified in a NSF workshop held in early the 90's as critical technology areas affecting the future economic strength of the nation [Jacobs and Hartnett, 1991].

Continuing developments in thermographic imaging techniques in recent decades have made it possible and affordable to apply these techniques to various areas in industrial and academic research, plant floor monitoring and surveillance, and many other applications.

The first thermometer was invented by Galileo (1564-1642). It was an air thermometer consisting of a glass bulb with a long tube attached. The tube was dipped into a cooled liquid, then the bulb was warmed, expanding the air inside. As the air continued to expand, some of it escaped. When the heat was removed, the remaining air contracted causing the liquid to rise in the tube indicating a change in temperature. This type of thermometer is quite sensitive, but not too practical since it can be affected by the slightest change in atmospheric pressure.

In 1714, a gentleman by the name of Gabriel D. Fahrenheit invented both the mercury and the alcohol thermometer with which we are all quite familiar. Fahrenheit's mercury thermometer consists of a capillary tube which after being filled with mercury is heated

to expand the mercury and expel the air from the tube. The tube is then sealed, leaving the mercury free to expand and contract with temperature changes. Although the mercury thermometer is not as sensitive as the air thermometer, it is not affected by atmospheric pressure changes.

The mercury thermometer has a serious drawback, however. Mercury freezes at -39° Celsius, so it cannot be used to measure temperature below this point. Alcohol, on the other hand, freezes at -113° Celsius. Therefore, by substituting alcohol for mercury, much lower temperatures may be measured.

Many industrial thermometers register temperature by means of a pointer on a calibrated dial. These kinds of thermometers contain no liquid but operate on the principle of unequal thermal expansion of metals. Since different metals expand at different rates, one metal can be bonded to another and when heated, the bonded metal will bend in one direction and when cooled it will bend in the opposite direction (therefore the term "Bimetallic Thermometer" BiMet). This bending motion is transmitted by a suitable mechanical linkage to a pointer that moves across a calibrated scale. Although not as accurate as liquid in glass thermometers, BiMets are much more rugged, easy to read, and have a wider span making them ideal for many industrial applications.

Thermal instrumentation development has progressed at a faster pace as microscopic phenomena have been explored and unveiled by modern quantum theory for various materials beginning at the turn of the century. Material properties such as electrical,

thermal, and mechanical behaviors are investigated and much insight has been obtained. People began to realize that all matter is comprised of tiny particles called atoms, with characteristic sizes which are on the order of angstroms. Atoms can further be resolved and consist of even smaller structures called nuclei and electrons. Electrons are negatively charged and form orbits around the nucleus. The nucleus is composed of positively charged protons and neutrons which carry no electrical charges. The number of protons, neutrons and electrons of each atom determines the identity of the atom. The same kind of atoms can bond together to produce a pure substance or they can be bonded to other kinds to form different molecules. The identities of the atoms and many other factors such as geometric arrangement and inter-atomic interaction of the molecules determine the properties of the material.

Such understanding created a tremendous opportunity for a wide range of thermal instrumentation development. Thermocouple, Resistance Temperature Detectors (RTD), infrared, liquid crystal, fluorescence/phosphorescence, to name just a few, are the major players in the field of temperature measurements. Generally, thermocouples and RTDs are limited to single point temperature measurement, while IR, liquid crystal and fluorescent/phosphorescent techniques can be applied to situations which are single point or two-dimensional. The above techniques will be described and reviewed in the following chapter.

Chapter 1

Review of Thermal Instrumentation

1.1 Single Point Measurement Devices

1.1.1 Thermocouples

Thermocouples have been widely used in industrial process control and monitoring as well as in the research laboratory. It is attractive primarily due to its low cost, good reproducibility, and availability as standardized industrial products. An example is the T type thermocouple made of copper and constantan wires. At the time of application, the two ends of the two-wire thermocouple are joined together to create electrical contact between the two materials, the common joining techniques include soldering, spot welding, or simply by twisting two bare wires.

Metals are one common and special kind of material having one or more electrons from the outer shell of each atom, that can move freely from one atom to the other. That is to say these electrons are not bonded to individual atoms any more. Metal can be perceived as positively charged nuclei immersed in a sea of electrons. When two different materials are joined together, due to the fact that electrons from different materials have different energies, there will be a net electron flow across the boundary until a potential/electric

field is establish at the interface of the two materials to offset and balance the electron flow. The electric field or potential difference across the dissimilar metal/metal interface results in a measurable voltage characterizing the interface. Two dissimilar metals joined together and heated at the junction will develop a thermoelectric potential difference (voltage) between the unconnected ends (Seebeck effect). The voltage will change with temperature since different materials respond differently to temperature change. Such a phenomenon is the operating principle of the most commonly used single point temperature measurement method – thermocouple temperature measurement. Typical responsivities of thermocouples are 10-40 $\mu\text{V/K}$ [Hudson, 1991].

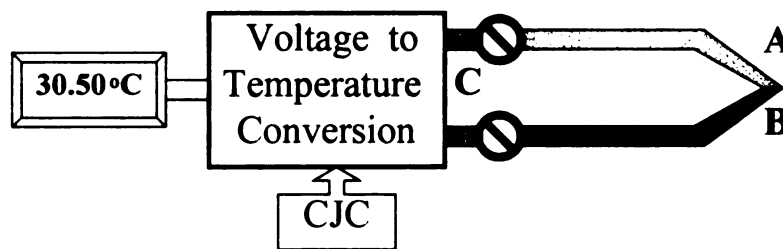


Figure 1. Thermocouple Temperature Measurement.

When voltage measurement equipment is connected to the two wires at their free ends, two additional dissimilar metal/metal interfaces are created. Let A and B denote the materials that make up the thermocouple and the terminal of the voltmeter is material C (Figure 1). The voltage measured will be $V_{cc} = V_{ca}^* + V_{ab} + V_{bc}^*$, where the stars denote the temperature condition of the voltmeter terminal. Since $V_{ab} = V_{ac} + V_{cb}$ and $V_{ij} = -V_{ji}$, V_{cc} will be zero if the thermal couple is also at room temperature as is the measuring equipment since $V_{ac}=V_{ac}^*$, and $V_{cb}=V_{cb}^*$. V_{cc} is non-zero only when the

two ends are at different temperatures, i.e., the voltage measured corresponds to the temperature difference between the two ends. Usually, a temperature sensitive resistive element (cold junction compensation - CJC) is used to provide an absolute measure of the room temperature. In this case, both the CJC reading and the thermocouple could introduce errors into the measurement. The error associated with the CJC could be the deviation from factory calibration, or a possible temperature difference between the CJC and thermocouple terminal connectors if they are far apart. Thermocouple wires are prone to error due to batch to batch variation of the materials: impurity, inhomogeneity and thickness. Another way to obtain an absolute temperature reading without a CJC device is to provide a temperature reference, e.g., an ice point. Carefully calibrated thermocouples can achieve accuracy to 0.1°C . Temperature reading obtained from poorly calibrated thermocouples or those without calibration could be off by several degrees.

1.1.2 RTD Thermometer

The Resistance Temperature Detectors (RTD) method is also a single point measurement technique that usually yields better measurement accuracy than thermocouples. This method takes advantage of the fact that the electrical resistance of certain metallic materials changes with temperature. Usually the measuring wire makes up one of the four arms of an electric bridge circuit. A voltage is applied at two diagonal junctions while the voltage between the other diagonal junctions is monitored. The output is adjusted to zero when all elements are at the same temperature. When the measuring arm is changed to

another temperature, its electric resistance changes as well, which will then result in a non-zero voltage output. Even though the RTD method could possibly provide very accurate reading (to 0.01°C), the complexity of the required circuitry makes it more expensive and inconvenient to use. The probe is also more bulky than a thermocouple thus making it awkward to apply to certain measurement situations.

There are also some other types of temperature measurement devices such as the thermistor, whose electric resistance changes with temperature.

Single point temperature measurement tools such as thermocouples and RTD thermometers are still widely being used for industrial process control and monitoring. It is most suitable for measurements in which spatial temperature variation is not a concern. Even though it is possible to install several thermocouples to obtain field information, in many situations, such an approach proves to be tedious and insufficient.

1.2 Thermographic Instruments

1.2.1 Infrared Thermal Imaging

Two decades ago, Infrared (IR) arrays were for the most part an exotic product of defense research and application. It is widely used by the military to conduct surveillance, and to develop heat seeking or laser guided missiles. Today, such imaging arrays are commonplace in the form of products ranging from hand-held IR cameras for industry

and security uses, to ultra-sophisticated devices for IR astronomy. Infrared arrays sense thermal energy, or heat irradiated from a surface. They are able to capture a two-dimensional image of a scene that emits thermal radiation. Continuing efforts to produce IR cameras with better performance and low cost have made this technique a popular investigation tool in both industrial and academic research.

Infrared detectors cover a fairly wide range of the electromagnetic spectrum: the near and mid infrared region, from 0.8 to 20 μm , and the far infrared region, from 20 μm to 400 μm .

There are four main classes of IR-sensitive quantum detectors that are based on semiconductor materials. The dominant approach today uses intrinsic semiconductors, such as mercury cadmium telluride (HgCdTe), which consist of pure, undoped materials. Extrinsic semiconductor detectors made from doped silicon or germanium, photo-emissive detectors, and quantum-well detectors are several other popular choices. In all these devices, incoming photons bounce electrons from the valence to the conducting band across an energy gap and change the electrical conductivity of the materials. The band gap defines the longest wavelength that a semiconductor can detect [Lerner, 1996].

HgCdTe Sensor: The HgCdTe compound has a band gap that can be varied to give a long-wavelength cutoff from 2 to 30 μm , providing great versatility. In many applications, these detectors are cooled to liquid-nitrogen temperature (77K) to obtain desirable high efficiency and low-noise performance. However, HgCdTe probably has

the most serious technical problems of any semiconductor in mass production today. Aside from using highly toxic materials that create environmental and occupational hazards during manufacturing, the compound is extremely difficult to grow reliably and repeatedly. These factors significantly increase their cost. In addition, varying sensitivity from pixel to pixel within an array can still be a serious problem for some applications involving quantitative analysis.

Extrinsic Materials: For sensing far-IR radiation, the band gap is so small that the ternary intrinsic semiconductor cannot work. The main alternatives are extrinsic semiconductors, generally based on silicon or germanium doped with impurities that can provide extra valence electrons. Those extra valence electrons, lying in the host material band gap, can be knocked off by photons with energy far below the band gap cutoff for the silicon or germanium itself. The drawbacks are they need to be cooled well below liquid nitrogen temperature, and the reliability is also an issue.

Photo-Emissive Detectors: In these detectors, a metallic compound, for example, platinum silicide (PtSi), is overlaid by doped silicon. A photon bounces an electron or, a hole, out of the conductor into the silicon. The advantage of such a device is that the response does not depend on the characteristics of the semiconductor but on those of the metal, which are extremely uniform. However, photon absorption is proportional to the square of the wavelength, so for wavelengths of a few microns, its efficiency and sensitivity are much less than that of the extrinsic devices.

Quantum Well IR Photo-Conductors (QWIP): The operating principle is similar to that for extrinsic detectors - the dopants are used to alter the band structure. But in QWIPs, the dopants are concentrated into microscopic regions, creating a quantum well. QWIPs can be tailored to reduce the energy a photon needs for detection. However, it is much more sensitive than extrinsic types, since the entire quantum well, not just an individual dopant atom, acts as an absorber. QWIPs use the manufacturing techniques of the mature GaAs chip technology and detector performance has been approaching that of HgCdTe. Just like the extrinsic detectors, QWIPs generally have to be cooled below liquid nitrogen temperature [Gunapala, et al, 1996].

Hybrid arrays: The most common IR imaging arrays are based on quantum detectors such as photodiodes or photoemissive detectors. In such IR arrays, as in any imaging array, the basic technical problem is to get the signals from each individual detector element, or pixel, to an output register in an efficient manner. For all materials except near-IR arrays, functioning at wavelengths shorter than $1\mu\text{m}$, this readout creates a problem, because the circuitry needed to amplify and process the signals is made of silicon, while the detectors themselves are generally made of other semiconductors. In the near-IR region, platinum silicide (PtSi) and Indium antimonide (InSb) arrays are available. Ternary compounds such as indium gallium arsenide (InGaAs) can be also fabricated into imaging arrays. For longer wavelength infrared sensing, the dominant material system is based on ternary compounds, especially mercury cadmium telluride. The processing requirement for these very different materials are in general incompatible, so the detectors are fabricated on one chip and the silicon processing circuitry on another.

These two arrays are then carefully aligned and bonded together by bumps of indium protruding from each detector and processing circuit. This results in a hybrid array.

Hybrid arrays have the advantage that nearly the entire area of the wafer is covered by the detectors because the circuitry lies on top of the detector elements. However, large area arrays are not easy to manufacture. Because two separate chips have to be made and then bonded together, there are many steps in the manufacturing process, and yields tend to be low, which forces the cost up. In addition, extreme dimensional accuracy is required to ensure that the indium bumps bond to each other correctly. Hybrid arrays typically are cooled to liquid nitrogen temperature (77K), which is another cost factor. Cryogenic cooling also introduces serious thermal stress for the two disparate materials which are bonded together and repeatedly cooled and warmed.

Readout circuits can cause complications with radiation detection. Silicon circuitry emits a small amount of radiation itself, which can add to the noise level in low level IR application. This problem can be avoided by using MOSFET circuits and turning them off while the detectors are collecting a signal. The circuit is turned on only briefly while a particular pixel is actually being read out, so extraneous radiation from the silicon circuitry is minimized. Conversely, the requirements of the readout circuits put demands on the detectors. The detectors have to be thin enough so that charge carriers can migrate efficiently to the other side where they are collected by the readout circuitry. This thickness is typically about 10 μm , and the wafer is not very strong. Often transparent substrates are added to provide the needed sturdiness.

A Monolithic array, as an alternative to the hybrid design, has the detector and readout circuitry fabricated on the same wafer. Such devices, while inefficient at short wavelengths, are useful for wavelengths beyond the 30 μm that limits intrinsic devices. Monolithic manufacturing techniques allow large numbers of pixels to be made on the same chip. Nevertheless, since the detector and circuit share space, the fill factor is well below 100%, reducing its efficiency.

In both types of arrays, signals are generally multiplexed, i.e., read out in such a way that the signals from all pixels are eventually funneled through a single output. Typically, in a given readout cycle, power is applied to each column of pixels in turn. Each pixel in the column is read out in sequence, and the cycle is then applied to the next column, so the entire array is represented as a sequence of signals in the final readout. Because each individual pixel can be addressed by this method, subsets of the array can be accessed, for example, for faster time response [Lerner, 1995].

Microbolometer arrays: With the advancement of fabrication technology, arrays of microbolometers, the leading thermal-array type, are challenging the more mature and developed quantum arrays for many application areas, leading to the development of room temperature thermal imagers.

Compared with the electronic sophistication of quantum detectors, bolometers are based on an extremely simple physical principle: the electrical resistance of certain materials

varies with temperature. For a given thermally isolated object (minimum heat conduction), any increase in absorbed radiation must lead to an increase in emitted radiation to reach equilibrium, and this can only be achieved by an increase in its temperature. At room temperature, a radiation intensity of only 1mW/cm^2 will lead, at equilibrium, to an increase in temperature of 1 degree, and one-tenth of that change in temperature can produce an easily detectable change in resistance. Bolometers are quite sensitive even at room temperature, and because they do not need to be cooled, costs can eventually be cut significantly.

A picture of pixel elements of a 320×240 microbolometer arrays [Santa Barbara Research Center, 1999] is Shown in Figure 2. Each pixel is $48\mu\text{m} \times 48\mu\text{m}$ and is made of thermistor materials VOx and fabricated monolithically on the silicon readout circuit. These arrays use a thermally isolated mechanical bridge to support a thin resistive film with a high temperature coefficient of resistance.

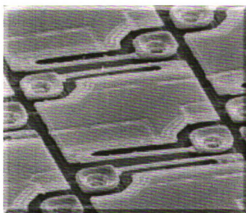


Figure 2. Pixel Element of Microbolometer Arrays.

The disadvantage of a bolometer, at the present stage of development, is a slow response time, because of the finite thermal mass of the detector, the device has to absorb enough heat to reach equilibrium before an accurate measurement can be made. The answer is miniaturization. The response time is proportional to the thickness of the absorber, and for a thickness of about 0.5 μm , response times drop to tens of milliseconds, fast enough for normal video-camera operation at 30 frame per second. For a typical microbolometer array, silicon is etched away from around and under a 50 μm square absorbing element, which is supported by two electrical conductors where each is only 0.1 μm thick and 5 μm wide. The thermal conduction through these tiny electrical conductors is sufficiently small that thermal sensitivities are within a factor of four of the theoretical maximum for a perfectly isolated device. The individual microbolometers are formed as part of a 256 x 256 array (typical). Because ordinary silicon and integrated-circuit materials and processing techniques are used, yields are relatively high and the costs of production are far lower than for quantum thermal arrays. A sensitivity of 0.07°C has been reported. Another drawback of the bolometer is that to achieve heat insulation, a vacuum dewar is required. Since their sensitivity is not as good as that of ternary hybrids, larger optics are required to compensate, which drives the costs back up [Lerner, 1995].

Near Field IR Thermography: To resolve the inherent diffraction-limited spatial resolution of the infrared technique, near field IR thermography is under development and evaluation in several academic and industrial research labs. Similar to its NSOM (Near-field Scanning Optical Microscope) counterpart for visible application, the near field IR method constrains the IR radiation in a region well below the diffraction limit by

utilizing a very fine probe tip and the collected thermal radiation is detected by a liquid nitrogen cooled IR detector. Two dimensional scanning is realized by a piezo-electric X-Y scanner.

Since the probe tip is very close to the scanning surface (a distance of approximate one probe tip diameter), this method is limited to investigation of surface temperature in the conduction or radiation mode. The current state of the art can push the spatial resolution to about 0.1 micron.

Currently, this technique can only be used to measure relative heating instead of absolute temperature. The limitations of this technique include low optical throughput due to the small aperture of the probe tip, complicated image interpretation, and probe non-uniformity, as well as slow scan speed. Since precision probe tip motion control, IR optics and high-speed electronics are necessary for such investigation, cost remains very high (based on email correspondence with Daniel Fletcher of Stanford University, October 98).

1.2.2 Liquid Crystal Thermography

Liquid crystal is a unique material that exhibits the behavior of both solid crystal and liquid. Liquid crystals can be classified into three categories according to their molecular arrangements: smectic, nematic, and cholesteric. The Liquid crystal material consists of

rod-like macromolecules and the orientation preferences of these macromolecules shows different diffraction behaviors, while subjected to changes of its environmental conditions, such as temperature, electric and magnetic fields, pressure, shear stress, etc. In the presence of white light, these changes create a change of the spectral distribution of reflected light and produce perceivable changes of color of the material. The liquid crystals being used for thermographic purpose are derived from esters of cholesteric liquid crystals and they exhibit temperature dependent properties [Abuaf, 1985].

A series of experiments designed to study the non-invasive evaluation of temperature on solid surfaces using liquid crystals was proposed by Akino et al (1989). These experiments were conducted by several research groups around the world. These experiments included the narrow bandwidth filter method, the multiple regression method, and the hue-based method. A review paper by Moffat (1990) summarized development in this area.

Liquid crystal thermography has been around for almost three decades and it has been mostly used in different situations for surface temperature measurement. Its advantages include: 1) moderate accuracy ($\sim 0.2^{\circ}\text{C}$); 2) moderate operating cost. Its two major drawbacks are: 1) insufficient temperature range ($\sim 10^{\circ}\text{C}$). In order to satisfy a given measurement accuracy requirement, the liquid crystal material is tuned to change color in a narrow temperature window; even though several liquid crystals which respond to different temperature ranges can be utilized to cover wider range, they also create more complexity; 2) inconvenience could become a problem in some cases since the liquid

crystal is made in a sandwich structure, this limits its applications to relatively flat surfaces; even though product in the form of spray paint is available for liquid crystal film fabrication that could make it possible to apply the technique to curved surfaces; the color spectral response is dependent on the angle of view and specular reflections impose severe problems; 3) slow dynamic response, the finite thermal mass of the liquid crystal film corresponds to a typical time response of about 1 Hz. In addition, calibration and data interpretation also involve considerable effort.

Some advancement has been achieved in materials and measurement technique. For example, narrow bandwidth filters were used to extract more than one temperature contour and semi-automated image processing has been devised. However, the reliability of the calibration methods and the time response of the liquid crystals require improvement before this method will likely be more widely used [Akino, 1989].

Despite these problems, the liquid crystal technique clearly demonstrates the practicality of the optical sensor concept, and in the form of commercially available research instrumentation, has made possible thermal measurements in varied situations.

1.2.3 Fluorescent/Phosphorescent Thermography

The use of phosphor for observing surface temperature patterns has been known for some time. In 1951, Urbach patented the use of various thermographic phosphors for

qualitatively visualizing temperature distributions on the surfaces of solid bodies [Urbach, 1951]. Bradley extended these techniques to evaluate aerodynamic effects leading to changes in surface temperature patterns [Bradley, 1953]. Brenner later applied a similar technique to measure temperatures of operating electronic devices [Brenner, 1971].

In phosphor, once excited, the activator ion can relax to its initial (ground) state by a variety of processes. At low temperature, the luminescent process dominates. At higher temperatures, the phonon-induced non-radiative relaxation process becomes dominant. The primary non-radiative quenching process in most phosphors is via multiphonon relaxation (i.e., collective molecular vibration motion) to either a lower energy state or the ground state of the ion. As the temperature of the phosphor is increased, the efficiency of these transitions increases because thermal expansion of the lattice increases the vibratory motion necessary to dissipate the energy released by these transitions, which leads to a decrease in the luminescent intensity.

Incorporated with fiber optics, phosphorous temperature sensors have been commercially available for contact type single point temperature measurements.

In some applications, the characteristic that phosphor emits sharp lines whose relative intensities change with temperature is used for temperature measurement. By isolating two appropriate emission lines and determining the ratio of their intensities, measurements of phosphor temperature independent of the absolute intensities of the

emission can be obtained. The phosphor can be fixed to the end of a fiber or coated onto the surface of interest and viewed at a distance. Complexity such as spatial probe concentration variation can be introduced into these systems if two types of phosphors are mixed to get the desired characteristic [Wickersheim and Mei, 1985], or the surface has different spectral reflectance/absorbance at the two wavelengths.

Kolodner and Tyson reported the implementation of a microscopic fluorescent imaging system that promised 0.01°C resolution [Kolodner, Tyson, 1982]. Filtered chlorobenzene solution containing 1.2wt% EuTTA (thenoyltrifluoroacetate) and 1.8wt% by perdeutero-poly-(methylmethacrylate) (dPMMA) was placed on the sample surface, spun at 600rpm, dried and baked at 125°C for 30 minutes. A film 300nm thick is formed. The surface is illuminated with long wave UV light (345nm - 380nm) and the orange fluorescence is imaged onto a CCD camera. Digital image processing removes the optical features in the images, leaving a purely thermal map of the surface. The temperature resolution is limited mainly by shot noise and can be improved by collecting more light. An inherent drawback for this system is photo-bleaching, a process characterized by the decrease in the fluorescent luminescence over time under constant UV illumination, even when the film is maintained at constant temperature.

Chyu, et al developed a rare-earth phosphor laser-induced fluorescence thermal imaging system for surface temperature and heat transfer analysis [Chyu, Bizzak, 1994]. They measured the temperature-dependent luminescence decays of the 512nm and 620nm emissions of the $\text{La}_2\text{O}_2\text{S}:\text{Eu}^{+3}$ coating under the irradiation of the frequency-tripled

output of a pulsed Nd:YAG laser (355nm). A measurement accuracy of about 0.5 °C was reported. The surface coating, which consists of a 1.0 mol % europium-doped lanthanum oxysulfide formulation, is about 25 µm thick with an average phosphor particle size of 7 µm. Since this type of coating is extremely fragile and can be damaged by incidental contact, a thin transparent potassium silicate overcoat has to be applied onto the phosphor film. Fluorescent emission is split into two beams and passes through 512nm and 620nm filters respectively. A neutral density filter is used to reduce the intensity of the 620nm emission. The two beams are then imaged by an intensified CCD camera. The camera's integrating period for the decay time measurements is synchronized with the laser pulses. To obtain desirable accuracy at the given signal to noise level, area averaging was used and this limits the spatial resolution to about 2mm. In addition, the system uses laser and exotic optics and electronics, which inevitably leads to high cost for implementation (\$150,000 ~ \$200,000). The major advantage of such a system is its capability to work at relatively high temperature (~1000F).

An investigation conducted by Caffrey in the Heat Transfer Laboratory of MSU indicated that the presence of oxygen in the test is the main reason for photo bleaching of the EuTTA system [Caffrey, 1994]. Since the system used a single wavelength as its measurement quantity, in-situ calibration has to be done for each test.

The fluorescent technique was applied to heat transfer study of shock-turbulent boundary layer interaction by Sullivan's group [Liu, Campbell, and Sullivan, 1995]. They used the mixture of EuTTA and dope (for coating hobby model-airplane) to fabricate of the

temperature sensitive film. Temperature measurement error taking into account the CCD digitizing accuracy (8-bit), calibration model, and thermocouple accuracy was estimated to be a total error of 0.85°C , for a range of 20°C to 50°C . Additional error caused by UV excitation fluctuation was not included which could increase the total error to over one degree. No further comparison between experimental data obtained by the fluorescent method and that given by other methods such as thermocouple was provided. Due to photo-bleaching of the EuTTA system, the calibration was conducted within a vacuum enclosure.

Barton's group [1996] modified the original system developed by Kolodner and Tyson to make this technique easier to apply to electronics thermal management analysis. However, the inherent photo-bleaching problem remained unsolved. An exponential model was used to infer the temperature distribution which resulted in an error up to several degrees for a 30°C range temperature measurement.

1.3 Description of Current Technique (FERIT)

There have been increasing demands in modern energy related industrial process control and monitoring for two-dimensional thermographic information. With the dramatic increase in computing power and lower computational costs, complex 2-D and 3-D heat transfer problems can now be modeled to evaluate a product's performance before the designs are handed to the manufacturing floor. Such practice is crucial not only to ensure good performance of a product, but it also plays a vital role in cost reduction related to

the potential savings in prototyping. The accuracy of the computer model will ultimately determine the usefulness of the model itself. There have been continuing efforts devoted to verifying those computer models. Comparison of data created by the models with experimental measurements are necessary and critical. Such comparison requires as much experimental data as possible. In the case of temperature measurements, there have been increasing demands for field information which can only be offered by thermographic measurement tools such as infrared, liquid crystal, and fluorescent/phosphorescent techniques.

Unfortunately, it is still not quite possible to meet the measurement requirements using just one single kind of method currently available, while considering accuracy, ease of use, dynamic response and cost factors.

The infrared technique is quite versatile, but its high cost and relatively poor spatial resolution as well as the difficulty of obtaining accurate emissivity data make it less attractive to many users. Even though some systems for surveillance use become less expensive, systems with a scientific grade sensor still cost between \$50,000 to \$200,000. Take the 700 series IR cameras made by Inframetrics (Billerica, MA) as an example. The Model 740 operates at a normal range of -20°C to 400°C and has a measurement accuracy of $\pm 2^{\circ}\text{C}$ or $\pm 2\%$ over the full range with repeatability of $\pm 0.5^{\circ}\text{C}$ or $\pm 0.5\%$. The high end Model 760 can operate between the range of 2°C to 1000°C and has a measurement accuracy of $\pm 1^{\circ}\text{C}$ or $\pm 1\%$ and repeatability of $\pm 0.5^{\circ}\text{C}$ or $\pm 0.5\%$ (Inframetrics website, 1998). The Model 700 series costs \$60,000 or more depending on configuration. The 700

series scanner design incorporates a dual resonant galvanometer scanning mechanism and a single HgCdTe detector which produces images by raster scanning the scenes. New classes of IR cameras have become available using small format (320 x 240) PtSi sensor arrays or even the microbolometer arrays. Their temperature measurement accuracy is poorer than the scanning HgCdTe sensor even with calibration to account for the response non-uniformity of individual IR sensing element. There is some improvement in dynamic response (frame-rate) for these new devices but there isn't much improvement for its spatial resolution.

Moderately high temperature accuracy ($\sim 0.2^{\circ}\text{C}$) can be achieved utilizing the liquid crystal technique but this is only possible in a fairly narrow temperature range ($\sim 10^{\circ}\text{C}$). It has limited dynamic response and is useful mostly on flat surfaces. Calibration difficulty is still a problem for the liquid crystal technique. It has rarely been applied to application of microscopic scale ($\sim 1\text{ }\mu\text{m}$).

The phosphor technique, measuring the decay time of rare-earth chemical compounds, usually requires exotic optics and electronics. It has limited success in accurate temperature measurement with the disadvantage of high cost. Previous fluorescence-based techniques promised low cost, good accuracy and high spatial resolution. However, photo bleaching (intensity decaying over time) was encountered for the previous system (EuTTA) which makes it difficult to apply to transient phenomena or even steady state conditions. It also imposes difficulty for calibration since the sample has to be placed in a vacuum to prevent photo-bleaching over the several hours period of calibration (~ 3 hours).

for 7 calibration points). In addition, fluctuation of the UV source is a major determining factor in intensity measurement accuracy and it has not been considered in previous investigations. The EuTTA system also has a limited workable range ($\sim 30^{\circ}\text{C}$). The lack of systematic study has also prevented it from becoming a main stream competitor in the thermographic instrumentation market.

The Fluorescent Emission Ratio Imaging Thermography (FERIT) technique is currently under development at the Heat Transfer Laboratory of Michigan State University. Based upon the literature reviews of the current state-of-art technologies (Infrared, Liquid Crystal, Phosphors), this research work on Fluorescent Emission Ratio Imaging Thermography (FERIT) will address problems previously encountered and study its implementation systematically. The characteristics of such a system will be evaluated and applications to heat transfer problems will be used to demonstrate its capability.

The fluorescent imaging thermographic technique was proposed as early as the 70's but it hasn't received much attention and popularity compared to the infrared and liquid crystal techniques. One important reason is the lack of systematic study of the several important aspects as a scientific instrument. Limited progress has been achieved in areas such as temperature-sensitive film fabrication. However, much work has to be done to finally realize its potential and become a standard measurement apparatus. Such work is necessary and vital since this technique has begun to demonstrate its great potential in high power electronics thermal management analysis, especially at the microscopic level.

The work presented will address the key factors associated with fluorescent imaging thermography. Unlike infrared and liquid crystal thermographic techniques, where a substantial amount of work has been devoted to characterizing such a system in terms of measurement capability, there hasn't been much systematic study to look at fluorescent techniques in such a way, especially from the engineering point of view. Such study is especially important to the fluorescent technique because these factors which ultimately influence the measurement accuracy of this technique are related to each other. Methods for such characterization will be presented and discussed. The scope of work will cover film fabrication, imaging system development and temperature rendering, and error estimation. The new system of temperature-probe/solvent described here also has significant advantages over other systems currently used by other research groups in terms of morphology and photo-bleaching characteristics, which will significantly improve the ease of calibration and make it more applicable to studies of thermal transients. This work could be used as a benchmark for utilizing the fluorescent thermography for similar analysis. In contrast to qualitative or semi-quantitative temperature measurement/estimate done previously, examples of quantitative surface temperature measurements will be demonstrated to show the improvements realized using the system being developed in our lab. Recommendations for setting up such a system in terms of measurement requirements, costs and limitations will also be provided and discussed.

In summary, the developed system seeks to demonstrate potential advantages in the following areas compared with the current infrared, liquid crystal and fluorescent methods:

Comparing with infrared method:

- (1) Higher spatial resolution by working in the region of visible wavelengths.
- (2) Much lower costs.
- (3) Easier calibration and temperature interpretation.
- (4) Comparable or Higher temperature accuracy.
- (5) Lower operating and maintenance costs.

Comparing with liquid crystal method:

- (1) Higher spatial resolution since thinner films can be fabricated (sub-micron for FERIT comparing to $\sim 50\mu\text{m}$ for liquid crystal).
- (2) Wider operating range.
- (3) Easier calibration and temperature interpretation.

Comparing with other fluorescent techniques:

- (1) Solvent system is more environmentally friendly. It has lower surface tension than chlorobezene or acetone and has a higher evaporation rate.
- (2) The temperature probe is much less susceptible to photo-bleaching which makes calibration much easier.

- (3) The temperature probe also has a wider working range (80°C) compared to 30°C for the EuTTA system.
- (4) System characterization and UV fluctuation monitoring reduce the system error by more than half.

Chapter 2

Review of Fluorescence Based Thermography

2.1 Theory of Molecular Fluorescent Emissions

Molecular luminescence is the phenomenon where visible photons are emitted from excited molecules. It can be further classified into photoluminescence and chemiluminescence. Fluorescence and phosphorescence are the types of photoluminescence in which excitation is the result of absorption of photons. In chemiluminescence, emission occurs from the excited states produced by a chemical reaction.

Fluorescence involves photo-emission between states of the same multiplicity, usually from singlet to singlet electronic state. Phosphorescence involves radiational transitions between states of different multiplicity, usually from triplet to singlet.

Fluorescence has been known for centuries. In 1852, Stokes first introduced the term “fluorescence”. The terminology “Stokes Shift” named after him denoted the characteristic of fluorescence: the wavelength of the emission photon is longer than the wavelength of the absorbed excitation photon.

The internal electronic states of atoms or molecules determine if they are capable of fluorescing while energized by external excitation of incoming photons. A Jablonski diagram is useful to describe the possible energy pathways after radiational excitation is absorbed (Figure 3).

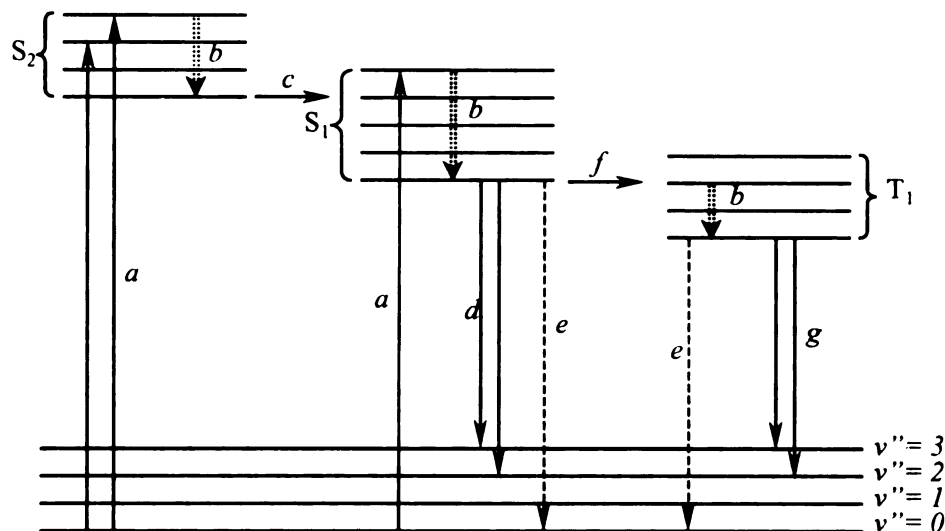


Figure 3. Jablonski Diagram. Deactivation Processes for an Excited Molecule. a: Absorption; b: Vibrational Relaxation; c: Internal Conversion; d: Fluorescence; e: External Conversion; f: Intersystem Crossing; g: Phosphorescence.

The absorption process (a) is very rapid and on the order of the period of oscillation of the electric field of the absorbed photon ($\sim 10^{-15}$ s). As illustrated in the figure, transitions can happen from the ground singlet state (S_0) to various vibrational states of the first or second excited electronic state (S_1 , S_2).

Atoms or molecules in excited vibrational states rapidly dissipate their excess vibrational energy and relax to the ground vibrational level of the excited electronic state (process b).

The energy goes into thermal or vibrational motion of its neighboring molecules through a vibrational relaxation process. The typical time scale is about 10^{-11} to 10^{-10} s, and many vibrations occur before the excessive energy is lost.

The crossover between two electronic states ($S_2 \Rightarrow S_1$) of the same multiplicity is a non-radiative electron state transition called “internal conversion” (process c). This is most likely to occur when the potential energy curves for two electronic states cross such that the lower vibrational levels of the higher electronic state are approximately the same as the higher vibrational levels of the lower electronic singlet state. Such a process converts excess electronic energy to excess vibrational energy and has a time scale about 10^{-12} s.

After the internal conversion, excess vibrational energy is rapidly dissipated through vibrational relaxation to the ground vibrational level of the lower electronic state.

Fluorescence is a radiational transition between electronic states of the same multiplicity (process d). For most molecules, the electrons are paired in the ground state so that fluorescence involves a singlet-singlet transition. Since internal conversion is a more rapid process than fluorescence, molecules in the higher excited state (S_2) are most likely to convert to the lower excited state (S_1) through internal conversion instead of going from S_2 to the ground state S_0 by emitting a photon. This results in a single fluorescent band even if absorption to different excited singlet states occurs. Fluorescence typically requires about 10^{-10} to 10^{-6} s to occur. The amount of Stokes shift is determined by the difference in energy between the excited higher electronic state or higher vibrational levels of absorption and the lower vibrational levels of the lower electronic singlet state.

Instead of relaxing to the ground state by fluorescing (emission of a photon), excited energy can also be transfer to other species such as a solvent through a non-radiational process denoted “external conversion”. One primary mechanism of external conversion is dynamic quenching. It involves the non-radiational transfer of energy from excited species to other molecules during collisions. This actually constitutes the operating principle of fluorescent emission thermography since temperature is a determining factor for such a quenching process.

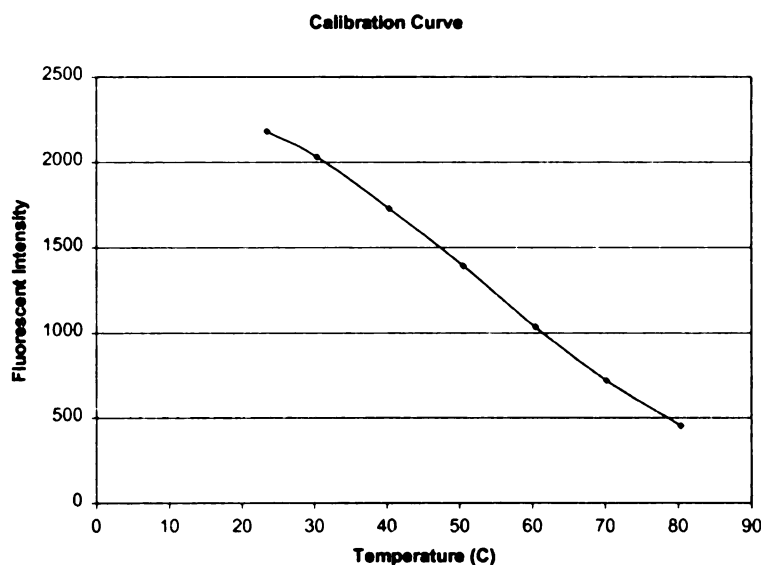


Figure 4. Fluorescent Emission Intensity as a Function of Temperature for Eu(hfa)_3 .

The relationship between fluorescent emission intensity and the temperature of the fluorescent probe being used for this study (Eu(hfa)_3) is illustrated in Figure 4. Due to thermal quenching, the fluorescent emission intensity decreases monotonically with increasing temperature.

Another possible path to lose the excited energy is through stimulated emission, which is likely to occur at much higher excitation intensity (laser induced fluorescence: a 1mW laser with 1mm² beam/spot size will produce 1 kW/m² output intensity, which is about three orders of magnitude higher than the excitation level used in this study). The fluorescent signal E_F is related to the incident irradiance $(E_P)_0$ as follows [Ingle and Crunch, 1988]:

$$E_F \propto \frac{ck_F}{1 + \frac{k_F}{\sigma(\lambda)(E_P)_0\phi_F}} \quad \text{Eqn. [1]}$$

For low $(E_P)_0$, the relation reduces to $E_F \propto (E_P)_0\phi_F\epsilon(\lambda)$, where the fluorescent signal is proportional to the incident irradiance. When $(E_P)_0$ becomes very high, $E_F \propto ck_F$, the fluorescent signal is independent of the source irradiance and the fluorescence quantum efficiency because the rates of stimulated absorption and emission are balanced. Non-radiational deactivation becomes negligible, i.e., the temperature dependent behavior is no longer observable. Such characteristics given by Eqn. [1] can be calculated and the relative intensity as a function of excitation intensity is plotted in Figure 5. In region towards saturation, the fluorescent emission intensity and excitation intensity relationships will thus be different for different excitation levels since stimulated relaxation could change the ratio of the fluorescent relaxation and the thermal quenching. Even though it is possible to derive calibration relation for various excitation levels; however, at time of application, non-uniformity of UV illumination will require absolute

measurement of the spatial distribution of the excitation and apply the calibration relation accordingly, which is a very difficult task. It is important to verify that tests of interest are conducted in the linear (low excitation level) region and no saturation condition is present.

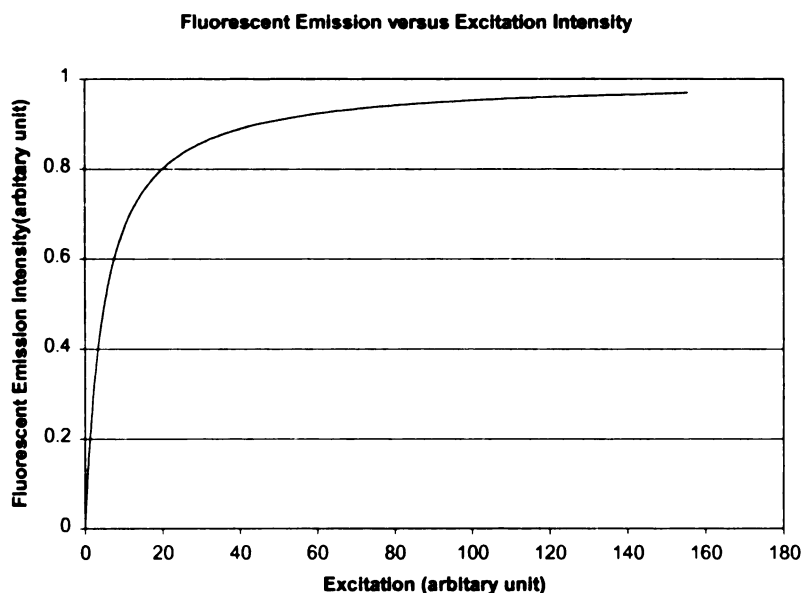


Figure 5. Fluorescent Emission Intensity as a Function of Excitation Intensity.

If the fluorescent film is in intimate contact with a metallic surface (silver, gold, aluminum, etc.), the interactions between the excited molecule and the metallic surface plasmon as well as its mirror reflection can change the lifetime of the excited state, introducing a new competing relaxation mechanism in addition to fluorescence and thermal quenching. At a distance very close to metallic surface ($< 200 \text{ \AA}$), the excited energy can be effectively transfer to the metal surface plasmon and the lifetime is reduced dramatically [Drexhage et al, 1968]. At larger distance (200 \AA to $1 \text{ }\mu\text{m}$), the mirror

effect is dominating and the lifetime is oscillating around a value corresponding to a free molecule [Chance, Prock, and Silbey, 1978]. The above effects are significant for situations with very thin films ($< 0.1 \mu\text{m}$).

The energy transfer within the Eu(hfa)_3 molecules has been extensively studied [Sager, et al, 1965; Halverson, et al, 1964] and can be described as the following steps: (1) ground singlet state absorption to the excited singlet state; (2) radiationless intersystem crossing from the excited singlet to the lowest lying triplet state; (3) transfer of energy to the chelated ion; (4) characteristic ionic fluorescent emission.

Chapter 3

System Development

3.1 Temperature-Sensitive Fluorescent Probe

The temperature sensitive fluorescent probe $\text{Eu}(\text{hfa})_3$ used in this study was synthesized using Europium(III) Chloride hexahydrate and ligand 1,1,1,5,5,5-hexafluoroacetylacetone. The chemical structure of the compound is shown in Figure 6.

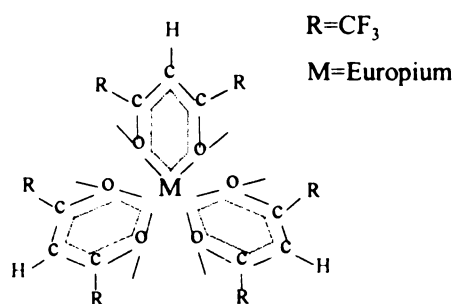


Figure 6. Temperature Sensitive Fluorescent Probe.

Europium chloride hexahydrate was first dissolved into 50ml of distilled water and the pH of the solution was increased to approximately 8.5 by adding ammonium hydroxide. Next, a stoichiometric amount of ligand (hfa) is added while stirring. The precipitate was filtered and dried for 24 hours at 70°C.

3.2 Coating Techniques

Film application methods are primarily determined by the costs, film thickness, appearance requirements, and structure of the object to be coated. Several commonly used methods are described in the following sections [Wicks, Jones, Pappas, 1994].

3.2.1 Brushes, Pads, and Hand Rollers

Brushes, pads, and hand rollers are frequently used for application in architectural coatings. The paints are usually thick (high viscosity) enough to prevent it from dripping and the resulting coatings are relatively thick.

Nylon bristles are appropriate for water-borne paints but might be swollen by some solvents. Hog bristles are appropriate for solvent-borne paints but not for water. Polyester bristles can be used with either. Paint is held in between the space of the bristles and forced out when applied onto the surface of the object. Paint viscosity is critical for paint pick-up. Too much paint will be brought out of the container if the viscosity is too high and too little will be on the brush if the viscosity is too low. Brush marks are a common problem for brush application where the newly applied wet film shows lines of thin and thick patterns.

A pad applicator can hold more paint than a brush and is more efficient on a large flat area. The resulting coating is also smoother. However, the use of trays could result in solvent loss, and the clean up is more difficult with pads than with brushes.

Hand rollers are the most efficient method and widely used in applying architectural paints to walls and ceilings. Viscosity requirements are similar to those for brush application. The main drawbacks are cavitation (formation of small bubbles) and spattering (droplets of loose paint fly off to land on the painter or the floor).

3.2.2 Spray Application

Spraying is widely used in architectural and especially industrial applications for applying paints and coatings. It is in general a much faster application method than brush or hand roller method. It is particularly suited for coating of irregularly shaped articles. The main disadvantage is its inefficiency of application since only a fraction of the spray particles are actually deposited on the surface. The transfer efficiency can vary from 25% for the compressed air method to 90% for the electrostatic rotary method for spray painting, where the transfer efficiency is defined as the percent of coating solids leaving the gun that is actually deposited on the coated product.

Since a compressed air spray gun is used in this study, the details of this method are described and a cross-sectional view of the Paasche 2P-VL#3 airbrush is illustrated in Figure 7.

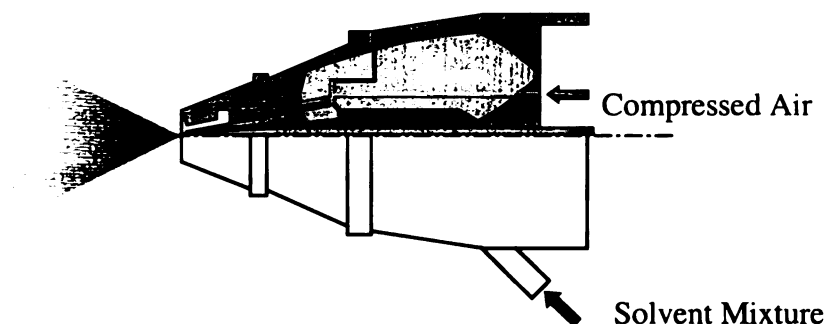


Figure 7. Cross-sectional View of Airbrush.

Compressed air or nitrogen (indicated by blue color) passes through an array of micro-channels and exits at the spray gun nozzle, forming a fan-shape flow profile. Due to the high velocity of gas flow between the gap at the nozzle exit, a low static pressure is realized in this region and the solvent (red) will be sucked from the storage bottle towards the nozzle exit. Atomization is realized while the solvent is mixed with the gas and breaks into small droplets, which eventually reach the surface of application. There is significant evaporation of solvent from the droplet surface which increases the droplet viscosity, but it is far from the conditions necessary to form solid pellets since the initial solid components concentration is very low ($\sim 1\%$). Those droplets strike the surface and form thin patches and the solvent evaporation is continued until a solid film is formed. Since the film is relatively thin, the trace amount of solvent in the deeper layer will eventually diffuse toward the film surface. Such a process can be speeded up by heating

the film above the polymer glass transition temperature for an extended period of time (~ 30 minutes).

3.2.3 Electrostatic Spraying

Paint transfer efficiency can be improved substantially with electrostatic spray units. A wire is built into the orifice of the spray gun and an electric charge of 50~125kV is applied to the wire. Electric discharge of the fine wire leads to ionization of the air. As the atomized paint particles pass through this zone of ionized air, they pick up a negative charge. Since the object to be painted is electrically grounded and the charged paint particles will be attracted to the surface. The drawbacks for this technique are higher equipment cost and the requirement for electrically conductive substrate.

3.3 Solvent-Based Fluorescent Film Fabrication

To produce fluorescent thin films for this study, a thin layer of solvent mixture is applied to the surface of interest using an artist's airbrush. Back and forth lateral motion of the airbrush is required to produce a uniform film that covers the whole surface. The film formation process is illustrated in Figure 8. Initially, solvent molecules evaporate from the air/solvent interface into the open air and reduce the solvent concentration near the interface and increase the film viscosity. Solvent molecules in the deeper layer move up to the interface driven by diffusion in the intermediate step. A solid film is formed where

the temperature probe is encapsulated by the polymer matrix (PMMA) in the finally stage. There will be trace amounts of solvent molecules being trapped in the solid film. The amount will be determined by the evaporation/diffusion dynamics and the film thickness, as well as post-fabrication treatment such as thermal quenching.

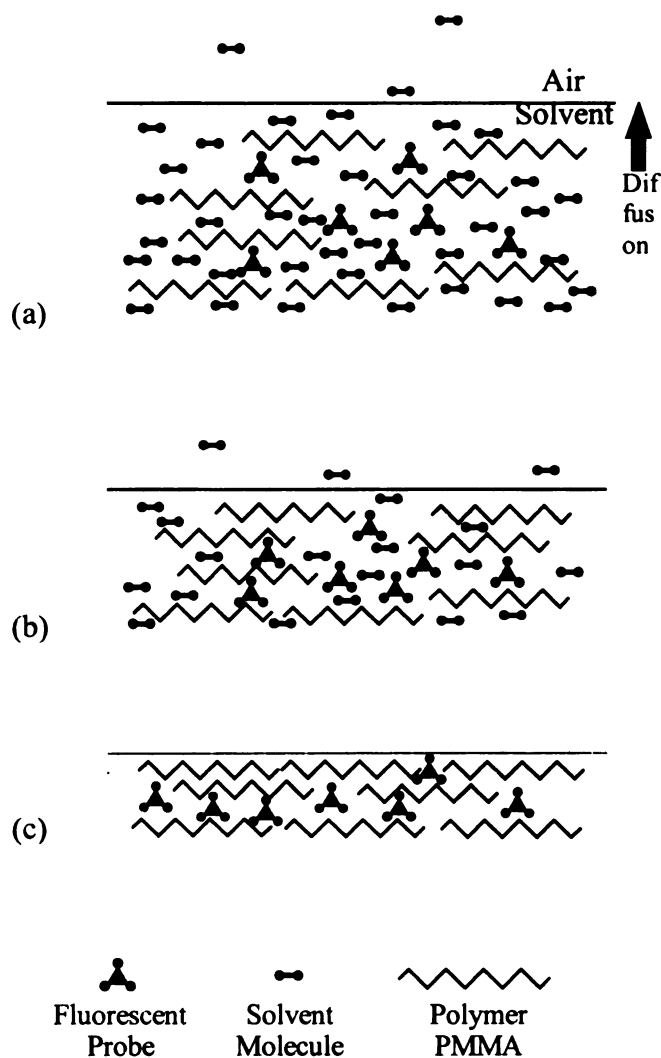


Figure 8. Fluorescent Film Forming Process: (a) Initial Solvent Evaporation and Diffusion; (b) Intermediate Step; (c) Solid Film Formation.

3.4 Fluorescent Imaging System

The fluorescent emission ratio imaging thermographic system developed (Figure 9) is comprised of the following components: ORBIS cooled digital CCD camera capable of outputting both 12 and 16 bit gray scale images, ultraviolet light source consisting of a Mercury/Xenon lamp and UV filter, Windows based Pentium computer (300 MHz) for overall system control and integration, data acquisition for UV intensity fluctuation monitoring, temperature measurement and digital control.

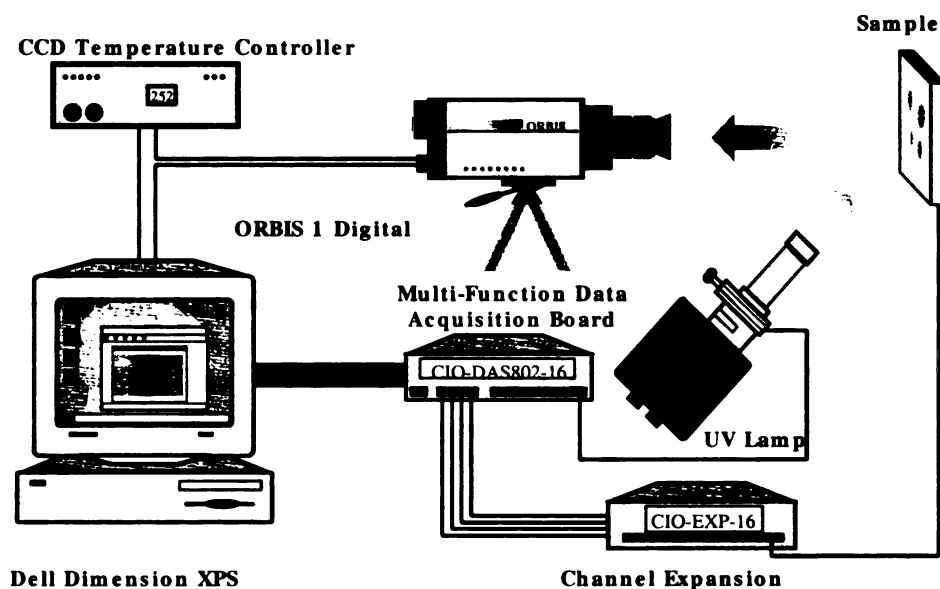


Figure 9. FERIT System Schematic.

The ORBIS camera was purchased from SpectraSource Instruments, Inc. The selected CCD sensor was manufactured by SITe Inc. (formerly Tektronix) and it is a back-illuminated 512 x 512 sensing array with 24 μ m x 24 μ m square pixel format. The CCD is

thermo-electrically cooled to -20°C to reduce dark current. The device operates in full frame mode and is capable of a frame rate up to 3 frames/second.

The optical lens used was a Rainbow G25 with adjustable IRIS and focus (focal length = 25mm, minimum working distance = 0.50m).

The highly stable UV source (STD <0.1%) was made by Opti-Quip. It features a 200W Mercury/Xenon lamp with 2000 hour life expectancy and 1.9mm arc length, according to the manufacturer (USHIO: UXM-S200KL, Opti-Quip: #BA-026). The UV filter was a high temperature bandpass filter (Model: 365HT25, central wavelength=365nm, bandwidth=25nm, 2 inches OD) from Omega Optical with high transmittance at 365nm (42%).

The red filter was also purchased from Omega Optical (Model: 620DF35, central wavelength=620nm, bandwidth=35nm, 1 inches OD) which features high transmittance at 620nm (~90%). The spectral transmittance of both filters is included in the Appendices.

A general purpose camera control and acquisition software was shipped with the camera which provides basic function control of the thermoelectric unit and the camera such as exposure time, binning, sub-area acquisition and basic arithmetic operations of images. Since the software only works with a self-contained file format (FTS) and lacks the

flexibility for image processing, the decision was made to develop custom application software to better suit our needs.

3.5 System Characterization

In order to give an estimate of errors of the measurement system as a whole, the performance of the individual system components were characterized and quantified, including the camera and UV source.

3.5.1 Noise Characteristics of ORBIS Cooled Digital Camera

The measurement noises of the CCD camera can be classified into the following groups: (1) read noise, (2) dark noise, (3) shot noise, (4) systematic offset. The importance of each noise source will be identified and used as criteria for estimating noise levels for future camera operation conditions. Such analysis applies to the full frame CCD camera and can also be applied to other CCD devices such as frame transfer CCD devices.

The read noise is the uncertainty introduced by the readout devices such as amplifiers and A/D circuitry while converting electronic charges to a digital value. The back-illuminated SI502AB normally operates up to 3 frames/sec with a serial pixel rate of about 800 K pixels/sec. Operating at higher readout rates results in a loss of full well in addition to increased noise. From bandwidth considerations we expect the noise to

increase by the square root of the pixel rate. For example, increasing the rate from 50 K pixels/s (the rate at which the readout noise is measured at SITe) to 800 K pixels/s (the readout rate of the ORBIS camera used in this study) would result in approximately 4.5 times more noise [Email correspondence with Dr. Ray Hayes of the CCD chip manufacturer, SITe Inc.], i.e., from 9 electrons to 41 electrons. Since the full well of SITe502AB is approximately 350,000 electrons, the above change would correspond to an error of 0.48 detector unit (DU) (12 bit mode, 0 ~ 4095) and is well below the digitizing resolution (1 out of 4095).

Dark noise is associated with the electric charges accumulated during the exposure period through thermal excitation. It is linearly related to the exposure time. For a fixed exposure time, the way to reduce the dark noise is to cool the CCD to lower temperature. The SI502AB CCD sensor has a dark noise of 12.75 e/pixel/s at -30°C (data from SITe Inc.). The ORBIS camera is cooled down to -20°C and the exposure-time dependent dark noise was re-evaluated here for this study.

The shot noise is the inherent uncertainty associated with the fluorescent signal strength. The relative error induced by this source (error to signal) is $1/\sqrt{N}$, where N is the number of photo-electrons collected and detected. The stronger the signal strength, the higher the accuracy. The simple way to reduce the noise is to average repeated measurements, essentially by increasing N .

System offset represents the difference between the measured value and real value without any other noise sources present. For a CCD imager, the offset is purposely pushed above zero to stay away from possible fluctuation below zero caused by other noise sources.

3.5.2 Linearity Study of UV Excitation and Fluorescent Intensity

As described in the section describing the fluorescent emission mechanism, fluorescent emission intensity is linearly related to UV excitation to a certain extent and then it will start to level off. Very high UV excitation will make stimulated emission become a competing energy relaxation mechanism, in addition to thermal quenching and fluorescence. In such a condition, the calibration relation between fluorescent emission intensity and UV excitation level will depend on the excitation intensity. Even though increasing UV excitation intensity has the benefit of enhancing fluorescent intensity, one could also run into the risk of inducing saturation and severe photo bleaching, as well as surface heating. It is important to verify that the measurement stays within the linear region.

3.5.3 Photo Bleaching Study

One potential advantage of the system we are developing is that it is less susceptible to photo-bleaching, which can severely limit the use of the fluorescent imaging technique.

The new combination of temperature probe and solvent has several advantages over the other systems tested to date. The fluorescent film at room temperature will be illuminated with an UV source over a period of one hour while the excitation intensity is monitored by a photodiode, and the fluorescent emission intensity will be measured at specified time interval. This study will define the extent of photo-bleaching for the excitation intensity used.

3.5.4 Influence of Moisture

Water molecules will compete with the ligands for the central ion and if such an effect becomes significant, it will drastically change the calibration behavior. On the other hand, since the polymer film (PMMA) is water-resistant and it will protect the fluorescent molecules from the moisture. Although the fluorescent probe wasn't shown to be susceptible to the presence of trace amount of moisture in the ambient air, it would be interesting to observe its behavior in extreme condition. The fluorescent film will be immersed in a water bath and the fluorescent intensity will be monitored over time. If significant change in behavior is found, the response of the fluorescent film to different humidity levels will also be investigated.

3.5.5 Effects of Quenching

Since there will be a certain amount of solvent molecules trapped in the deeper layer of the fluorescent film, quenching the film above the polymer's glass transition temperature (PMMA: $\sim 100^{\circ}\text{C}$) would enhance the diffusion process and leave fewer solvent

molecules within the film, it might also change the free volume experienced by the probe molecules. The effect of quenching will be studied in relation to its effect on the shape of the calibration curves.

3.5.6 Reproducibility

As a measurement system, it is important to demonstrate that the measurement produced by the system has good reproducibility. This will be verified in two ways: reproducibility of repeated tests and reproducibility between neighboring pixels in the same test. A test is defined here as a calibration measurement of fluorescent emission intensity as a function of temperature. In the first comparison, the fluorescent emission intensity as a function of temperature will be measured several times for the same sample before and after annealing at the same measurement location, and the shapes of the calibration relation are compared. The second comparison will focus on the same test, but the measurements are conducted for neighboring pixels that have experienced the same heating history. A sample will also be heated up from room temperature to 80°C and cooled back down to room temperature to investigate if there is any hysteric effect.

3.5.7 Effect of Fluorescent Probe Concentration

The solid fluorescent film fabricated consists of two components: the temperature-sensitive fluorescent probe and the polymer base (PMMA). Since the concentration of the temperature probe is very high (25wt%), the interaction between neighboring molecules might influence the temperature dependent behavior. Samples of different concentration

were fabricated and the calibration relations for these samples were compared. If the behaviors are concentration-dependent, local variation of probe concentration will result in temperature measurement variation even without the presence of any other system noise.

3.5.8 Aging Effect

Since FERIT utilizes chemical probe as sensing material and there might be aging effect associated with it, i.e., its temperature-dependent fluorescent emission behavior might change over time. The shape of calibration curve will be compared for two measurements made over extended period of time (~ one month).

3.5.9 System Dynamic Response

For time-dependent surface temperature measurements, dynamic response (frame rate) of the imaging system is an important factor that determines the system's temporal resolution.

The dynamic response of ORBIS camera will be evaluated for a metallic film heated by a pulse source. The pulse frequency/period will be varied and the temperature history of the film surface will be monitored.

3.6 Custom Software Development

Due to the limited data processing capability of the application software which came with the ORBIS camera, a Windows-based application has been developed using Microsoft Visual C++ version 5.0 to facilitate camera control, image acquisition and analysis, and conversion of gray scale intensity to temperature. The application also supports other electronic hardware for UV intensity monitoring, thermocouple temperature measurement and digital control, which makes them function as an integrated system.

The Application Wizard within Visual C++ was used to create the framework for a custom window application. It has a basic data structure that is called “Document/View paradigm” in which the Document class manages the data and storage while the View class handles data visualization, window messages and user interactions with the selected document. Similar to the word processing software, where text and formatting information are the primary data, our application mainly deals with gray scale images that are two-dimensional arrays of numerical data. Image data are copied into a document data buffer after they are obtained by the acquisition routine of the imaging library.

The overall structure of the software is illustrated in Figure 10. It has the following advantages over the software (Hpcwin32.exe) that came with the ORBIS camera:

- Compatible with Hpcwin32.exe in terms of camera control functions and enhanced in some functions such as multi-frame acquisition;

- Facilitates more common image file format (TIFF) which enables the possibility to use other image processing software for data processing;
- Incorporates other electronic hardware for system integration to accomplish analog and digital signal monitoring and control;
- Enhanced image processing capability such as temperature rendering.

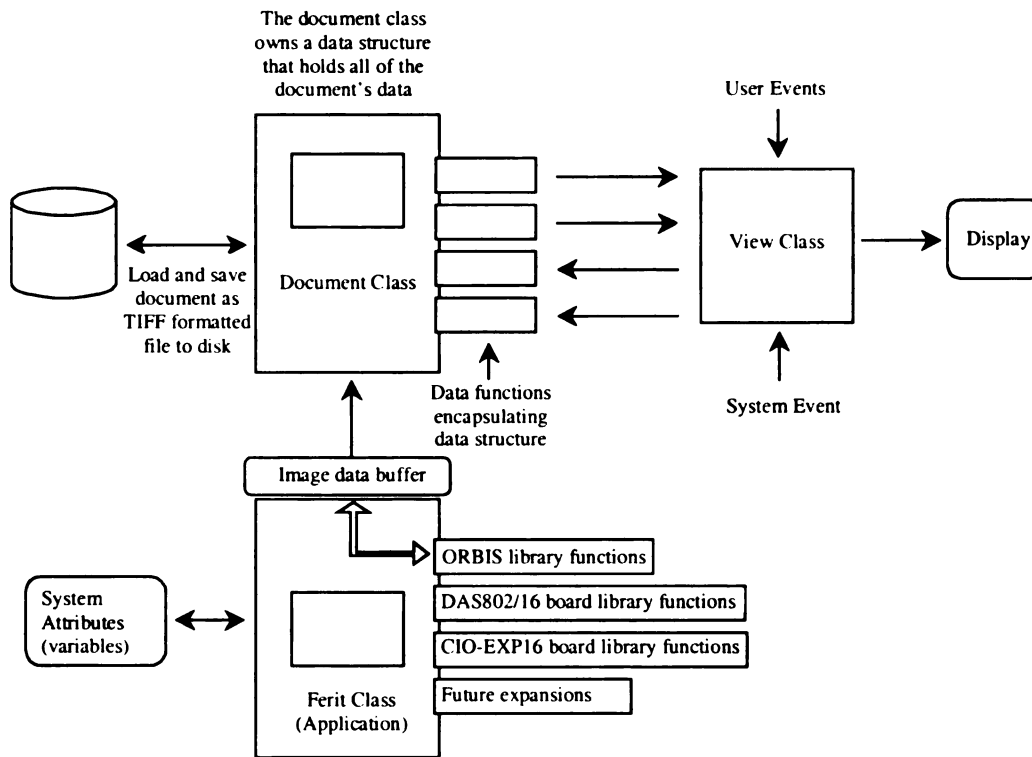


Figure 10. Structure of Custom Developed Application Software for FERIT.

The application software interface is illustrated in Figure 11. Operations are grouped together according to their functionality: hardware control, data processing, file handling, imaging and visualization modes.

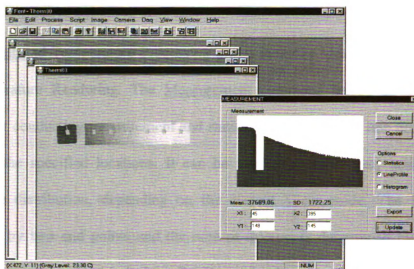


Figure 11. FERIT Application Software Interface.

The Camera Control group includes Camera Initialization, Configuration, and Single Image Acquisition. The initialization will check the camera control hardware to ensure they are connected and functioning properly. Configuration determines the operating parameters of the camera: TE cooler, image format (size), image offset and binning, exposure time, averaging, script mode control (number of frames, frame interval). Single Image Acquisition will capture one image at the specified configuration.

Script Mode group includes functions customized for FERIT: Background Image Acquisition, Reference Image Acquisition, and Multiple Images Acquisition at specified intervals. These commands are specific to thermography. Background Image refers to an image taken without UV excitation. Reference Image refers to an image taken with UV illumination at known temperature (usually room temperature). Multiple Images will start a sequence of acquisitions at a specified interval, with a File name "Image + index", where index is two digit contiguous and incrementing number starting from 00.

Measurement and Temperature Processing group includes Measurement, Configuration and Temperature Rendering. The Measurement command brings up a measurement template for conducting measurement and statistical analysis for a line profile or area of interest at the specified locations. It can be used to measure gray scale intensity or temperature distribution, depending on the current View mode. The line profile is determined by two end points and the area of interest is determined by two diagonal points. If the measurement is in Line Profile mode, the intensity (or temperature) along the line is plotted in the drawing windows (Figure 11). In Statistics mode, the averaged quantity (intensity or temperature) along the line or within the area of interest will be given as numerical values beneath the drawing window. The radio buttons are used to set different measurement modes. The Update button will take the end-points coordinates and execute measurements. The Export button is used to write the measurement results to an external ASCII file “output.txt” so that they can be imported to other plotting software.

View Options set different visualization modes that include Grayscale, Color, Default for intensity display and Temperature for temperature visualization. Since the Windows display system has a depth of 8 bits and our data are 12 bits or 16 bits, conversion is necessary so that they are properly scaled to the 8 bits system. No scaling is performed in Default mode and it saves some conversion time. Since selecting a different display mode doesn't change the internal data value, Default mode is recommended to realize highest

frame rate (the overhead introduced by conversion is about 0.1 second for a 512x512 image).

3.7 Algorithm for Temperature Rendering

The calibration provides the relationship between relative fluorescent emission intensity and absolute temperature. To obtain the surface temperature distribution of a particular experiment, an image containing the intensity distribution at a known (reference) temperature has to be obtained so that the temperature at other instants while the experiment is running can be inferred from the images taken at later times. Since the calibration is essentially non-linear, an efficient algorithm/method has to be developed to facilitate fast temperature rendering. Failure to do so will result in a significantly lower frame rate which would compromise the system ability to capture rapid dynamic situations.

Previously published qualitative work used a linear or exponential relationship to infer the temperature distribution, which usually results in several degrees in measurement error. A more elaborate mathematical model will be developed and used to obtain a much better fit for the calibration curve. Such a model will also provide an efficient way to convert fluorescent intensity to temperature.

One possible option is to use a high order polynomial function to represent the calibration relation. To obtain temperature information with such an approach, the following steps are required:

- Reference intensity at the reference temperature $I_{\text{calib}}(T_{\text{ref}})$ will be calculated with the calibration relation (polynomial: Intensity (Temperature)).
- The two measured intensities $I(T_{\text{ref}})$ and $I(T_{\text{unknown}})$ will be scaled proportionally so that $I^*(T_{\text{ref}}) = I_{\text{calib}}(T_{\text{ref}})$, and we obtain $I^*(T_{\text{unknown}})$ (the asterisk denotes scaled measurements).
- Apply $I^*(T_{\text{unknown}})$ to inverse polynomial relation (polynomial: Temperature (Intensity)) to obtain T_{unknown} .

It is obvious that a total of 16 multiplications is required ($16 = 14 + 2$) for seven calibration points. Such an approach will be very slow since multiplication is an expensive calculation. In addition, the temperature conversion time will depend on the number of calibration points, which is an undesirable feature.

A hybrid linear search model was developed. Instead of using a polynomial to represent the calibration relation, we tabulated in very small interval (0.01°C) the relation for the temperature range we have calibrated. Since seven calibration points were measured between room temperature up to 80°C (at 10°C intervals), a seventh degree polynomial was used to fit the seven calibration data and data are interpolated between calibration points with a 0.01°C interval. The error introduced is minimal (Appendix E) for the range

considered (<0.01 °C). To derive temperature measurement, the measured intensities are scaled to match the value of calibration at the reference temperature to obtain $I^*(T_{ref}) = I_{calib}(T_{ref})$ and $I^*(T_{unknown})$. Since the approximate slope in the intensity ~ temperature calibration curve is known, a linear search is done to get to the neighborhood of the final temperature where a sequential search starts until the final temperature is found. Since this approach uses only three multiplications and the sequential search is very efficient, the resulting speed is very good ($<0.2s$) and is independent of the number of calibration points.

The radiometric approach can be readily illustrated mathematically by the following derivation which starts with generic expression for fluorescent signal and its contributing factors:

Fluorescent intensity is determined by the following equation:

$$V_{out}(i, j) = [k(i, j) QE_{ccd}] * T_{optical} * \Omega * [1+R(\lambda)] * [I_{uv} D_{probe} A_{element} * QE_{probe}(T) * \Delta t]$$

Eqn. [2]

Where

$K(i, j)$: Digitizing conversion factor of Pixel (i, j).

QE_{ccd} : Quantum efficiency of CCD detector.

$T_{optical}$: Optical Transmittance optical elements (lenses, band-pass filters).

Ω : Solid angle subtended by the lens towards the fluorescent element.

$R(\lambda)$: Spectral Surface reflectance.

- I_{uv} : UV intensity.
- D_{probe} : Fluorescent probe density per unit area.
- $A_{element}$: Emitting area on sample surface that corresponding to pixel size.
- $QE_{probe}(T)$: Temperature dependent Fluorescent emission quantum efficiency.
- Δt : Exposure time.

Using the temporal ratiometric approach (ratioing of intensities derived at different times, with one of them at known reference temperature), the optical features caused by UV excitation non-uniformity, film non-uniformity, surface reflectance variation will be canceled out:

$$\frac{V(T_{unknown})}{V(T_{ref})} = \frac{QE(T_{unknown})}{QE(T_{ref})} \quad \text{Eqn. [3]}$$

since all of the other parameters remain unchanged except probe quantum efficiency induced by temperature change. The only assumption made using this ratiometric approach is that the probe fluorescent quantum efficiency is a function of temperature only while other parameters are kept constant. If a calibration relation for relative intensity change as a function of temperature is established, temperature distribution in future experiments can be obtained by comparing their relative intensity against the calibration.

The unknown temperature can be inferred from the following implicit ratiometric equation:

$$\frac{V(T_{unknown})}{V(T_{ref})} = \frac{V_{calib}(T_{unknown})}{V_{calib}(T_{ref})} \quad \text{Eqn. [4]}$$

- $V(T_{ref})$: gray scale intensity at $t=0$ at known startup temperature T_{ref} .
- $V(T_{unknown})$: gray scale intensity at time t at which point the temperature is to be determined.
- $V_{calib}(T_{ref})$: gray scale intensity at T_{ref} from calibration curve.
- $V_{calib}(T_{unknown})$: gray scale intensity determined from the implicit equation from which the unknown temperature is inferred.

Figure 12 and Figure 13 illustrate the temperature rendering method using the hybrid linear search approach.

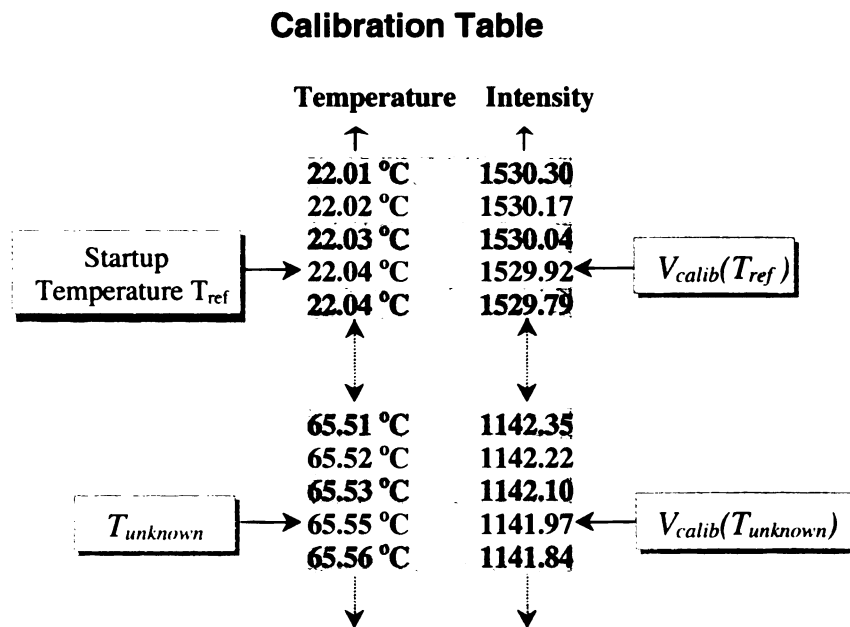


Figure 12. Calibration Data and Temperature Determination.

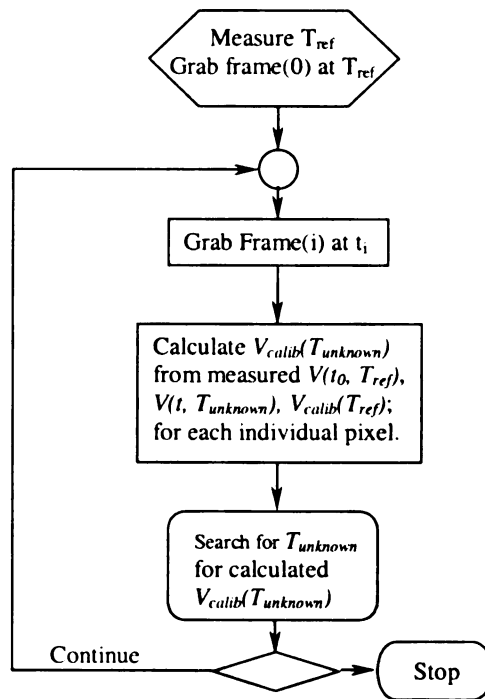


Figure 13. Flow Chart for Temperature Determination.

Chapter 4

Results and Discussion

4.1 CCD Camera Characterizations

The digital CCD camera is the most important part of the system and its noise characteristics have a direct impact on the measurement accuracy of the fluorescent emission intensity. The following tests evaluate the relative importance of various sources of uncertainty associated with the equipment.

The ORBIS camera was set to a default resolution of 12 bit to achieve better frame rate, thus all the quantities related to gray scale intensity measurements in the following experiments are in detector units (minimum: 0 DU, maximum: 4095 DU at 12 bit resolution).

4.1.1 CCD Read Noise Characterization

With no light input to the CCD sensor and minimal exposure time, the only contributing signal is the read noise. As shown in the next section, the dark noise with 10ms exposure time is $0.383 * 0.01 = 0.00383$ DU, which is negligible compared to other noise sources.

Other noises (shot noise, flicker noise) are zero since there is no light falling onto the CCD sensor.

The following procedure was used to determine the read noise:

- (1) Power up ORBIS camera, turn on thermo-electric cooler, and wait about 20 minutes for the CCD to reach steady low temperature (252K);
- (2) Set camera exposure time to minimum (10ms);
- (3) Close camera lens aperture or place a cover over the lens head to eliminate light input to CCD sensor;
- (4) Acquire two consecutive images;
- (5) Calculate the standard deviation between pixels from the two images, described as follows.

A group of pixels was selected from the center of the each image for which measurements were conducted. In this experiment, a 100 x 100 array of pixels at $(x_1, y_1) : (x_2, y_2) = (200, 200) : (299, 299)$ within the 512 x 512 sensing area were sampled. And the standard deviation is calculated with the following equation:

$$\sigma = \sqrt{\left(\sum_{i,j=1}^{100} \left(I_{ij}^{frame1} - I_{ij}^{frame2} \right)^2 \right) / 4(N-1)} \quad \text{Eqn. [5]}$$

Where I_{ij}^{frame} is the intensity of pixel measured at location (i, j). Such an approach is different from the standard way that measures many frames and performs measurement

for pixels in each frame which requires a substantial sample population (number of frames) to arrive at an acceptable value.

The experimentally determined read noise is 0.62 DU (detector unit), which is close to the estimate given by the CCD manufacturer (0.48). The discrepancy could come from the fact that the data provide by the CCD manufacturer was conducted at -30°C instead of -20°C . The measured read noise is close to one detector unit and can not be neglected.

4.1.2 CCD Dark Noise Characterization

In addition to the photoelectrons created by the absorbed photons, there is stochastic source of electrons in a CCD well through thermal excitation. Electrons can be freed from the CCD material itself through thermal vibration and then, trapped in the CCD well, be indistinguishable from "true" photoelectrons. The importance of this dark signal was evaluated by varying the exposure time and measuring the pixel outputs with the camera lens closed. The results are summarized in the following table and plotted in Figure 14. The pixel intensity is the average of 100×100 pixels at the same location $(x_1, y_1) : (x_2, y_2) = (200, 200) : (299, 299)$ and the CCD digitizing resolution was set to 12 bit.

Table 1. Dark Signals of CCD Sensor at Different Exposure Time.

Exposure Time (ms)	Signal Level (DU)
10	108.238
40	108.2635
160	108.2995
640	108.5285
2560	109.1215
10240	111.848
20480	115.5825
40960	123.4725
81920	139.4955
163840	170.906

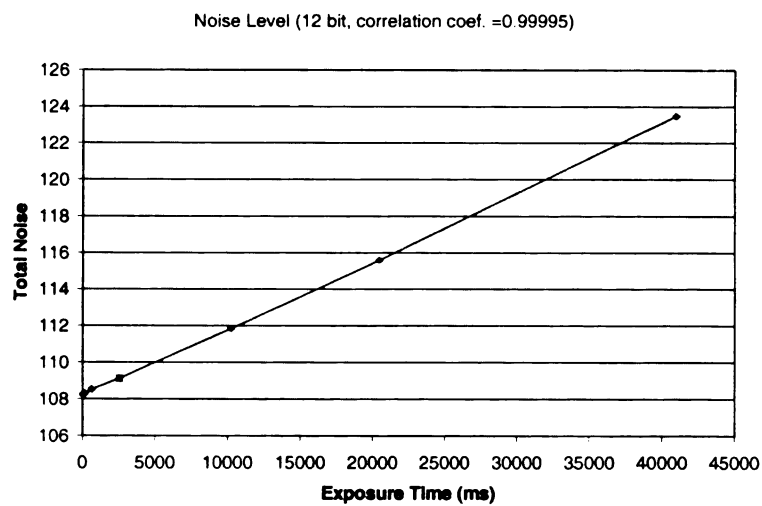


Figure 14. CCD Dark Noise as a function of Exposure Time.

The non-zero intercept at the abscissa is the result of systematic offset, which is a constant value. The intensity is expressed in detector units (0 ~ 4095 for 12 bit digitizing resolution, 0 ~ 65535 in 16 bit).

The data can be fit linearly by the following equation:

$$I = 108.096 + 0.382727 * \text{exposure_time(second)}$$

Eqn.[6]

The linear fit has a very high linear correlation coefficient of 0.99995 and Figure 15 compares the experimental data with the linear fit in logarithmic scale.

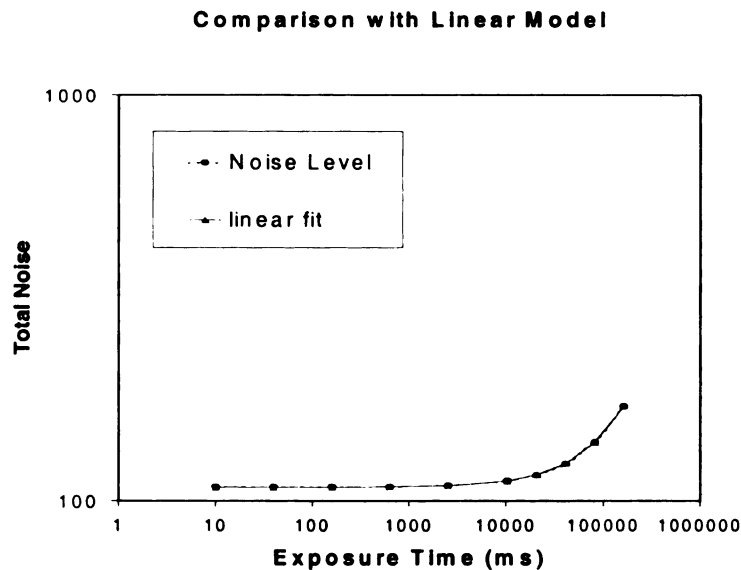


Figure 15. Dark Noise: Comparison of Experimental Data and Linear Model.

The equation suggests that the dark signal grows linearly with time as

$$I_{\text{dark}} (\text{DU}) = 0.383 * \text{Exposure_Time(s)}.$$

The linear equation suggests that for exposure time less than 2 seconds, the dark noise is not significant since it is smaller than the camera digitizing resolution. The dark electron creation rate can be calculated from the slope of the linear relation and is found to be about 32.76 e/pixel/seconds (based on the assumption that full well = 300,000 electrons, and full scale = 4095 for 12 bit), which is different from the Manufacturer's data (12.75 e/pixel/second) since their test was conducted at -30°C instead of -20°C , the operating temperature of our CCD. The above difference is quite consistent with the rule of thumb that CCD dark current doubles for every increase of 7 degrees in CCD temperature.

Even though the dark signal will be deducted from the total intensity by the subtracting the background image, there is still noise associated with the dark signal that is governed by Poisson distribution.

The magnitude of this noise can easily be evaluated as follows: For a typical exposure time of 1 second, the corresponding number of electrons is $N = (0.383 * 1) * 300,000 / 4095 = 28 \text{ e}$. The associated noise will be $\sqrt{N} = 5.3 \text{ e} = 4095 * 5.3 / 300,000 \text{ DU} = 0.072 \text{ DU}$, which is much smaller than the digitizing resolution (1 DU) and can be neglected. The above calculation assumes a full well of 300,000e and 12 bit digitization resolution.

4.1.3 Shot Noise

Shot noise is statistical uncertainty associated with a given signal of certain strength, which is described by the Poisson distribution. Shot noise is determined by the signal strength of the measurement and is proportional to the square-root of the total number of photoelectrons detected. The following calculation assumes the CCD sensor has a full well of approximately 300,000 electrons (for the SITe502AB CCD sensor used in this study, a TV CCD camera typically has a full well of approximately 30,000e). The signal shot noise of certain intensity (gray level in DU) is determined as:

$$\begin{aligned}\text{Shot_Noise (DU)} &= \text{gray_scale(DU)} / \sqrt{\text{num_of_photoelectrons}} \\ &= \text{gray_scale(DU)} / \sqrt{300,000 \cdot \frac{\text{gray_level(DU)}}{\text{full_scale(DU)}}} \\ &= \sqrt{\frac{\text{gray_level(DU)} * \text{full_scale(DU)}}{300,000}}\end{aligned}$$

which is plotted in Figure 16.

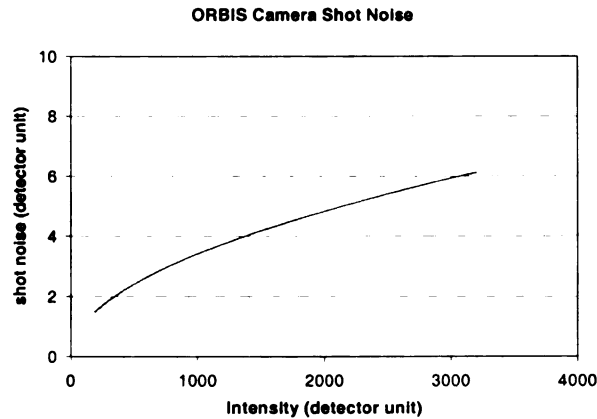


Figure 16. ORBIS camera Shot Noise (detector unit).

It can be seen that shot noise is proportional to square-root of N , with N being the number of photoelectrons detected in the CCD well. Even though the amplitude of shot noise grows with signal strength, the relative error (shot-noise/signal) is decreasing as $1/\sqrt{N}$.

4.2 UV Light Source Characterization

As an important component of the fluorescent emission imaging system, the UV light source is also a determining factor for the system performance. Since the system operates in the linear region regarding UV excitation relative to fluorescent emission, fluctuation in the UV excitation will be proportionally translated into the magnitude of noise in final intensity reading.

A Burr-Brown integrated photodiode (model: OPT301M) with amplifier was used to conduct UV light intensity measurements. The characteristics of the photodiode are summarized in Appendix D. The photodiode has good UV response and very low dark and read noise. With a full scale at about 8.0 volts ($\pm 9V$ power supply), the noise level of the integrated photodiode was measured to be less than 0.001 volts. The linearity with respect to intensity variation is 0.01% of full scale. The dynamic response ($\sim 5kHz$) is also fast enough to capture the rapid change in UV light intensity. The spectral response of the photodiode at 365nm is approximately 0.15A/W and the sensing area is 2.29 x 2.29 mm. The absolute excitation intensity can be obtained by dividing the output voltage by the value of the known feedback resistor:

$$I = \frac{U_{output}}{R_F \cdot R_p(\lambda) \cdot A} \quad \text{Eqn. [7]}$$

where U_{output} is the output voltage in volts, R_F is the feedback resistor ($1M\Omega$), $R_p(\lambda)$ is the spectral response ($0.15A/W$), and A is the active sensing area of the photodiode ($2.29 \times 2.29 \text{ mm}^2$).

Most UV sources have a power regulator to maintain steady output. This standard Silicon Controlled Rectifier (SCR) type of supply switches on and off only 120 times a second and can produce a significant amount of ripples.

The long-term and short-term intensity variations are illustrated in Figure 17 for a 100W Nikon high-pressure mercury lamp. The time units for the abscissa are minute and millisecond, respectively. Each data point in the long-term curve represents an average of 1000 intensity measurements sampled at 1 kHz. It can be seen that the power output stabilizes after 40 minutes but the fluctuation is still fairly high after that ($\sim 0.5\%$ standard deviation). The short-term behavior is characterized by 120 Hz output spikes. A sampling rate of 1 kHz is necessary to accurately capture the intensity fluctuation.

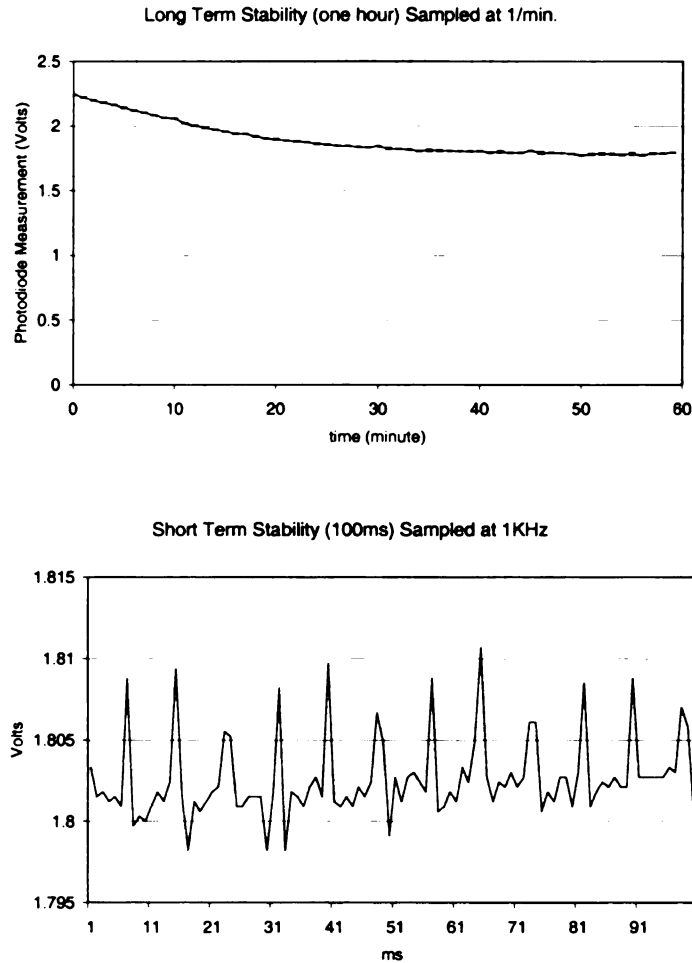


Figure 17. Long and Short Term Stability of 100W Nikon Mercury Lamp.

The Opti-Quip 1600 power supply uses MOSFET regulating circuit and switching at 30,000 times per second. Such an approach improves the short and long term behavior dramatically. The short-term ripple is less than 0.1%, as shown in Figure 9. The system uses a USHIO 1.9mm gap 200W Mercury-Xenon lamp (USHIO: UXM-S200KL, Opti-Quip: BA-026) as its source which features extended life span (2000 hour life) and good stability.

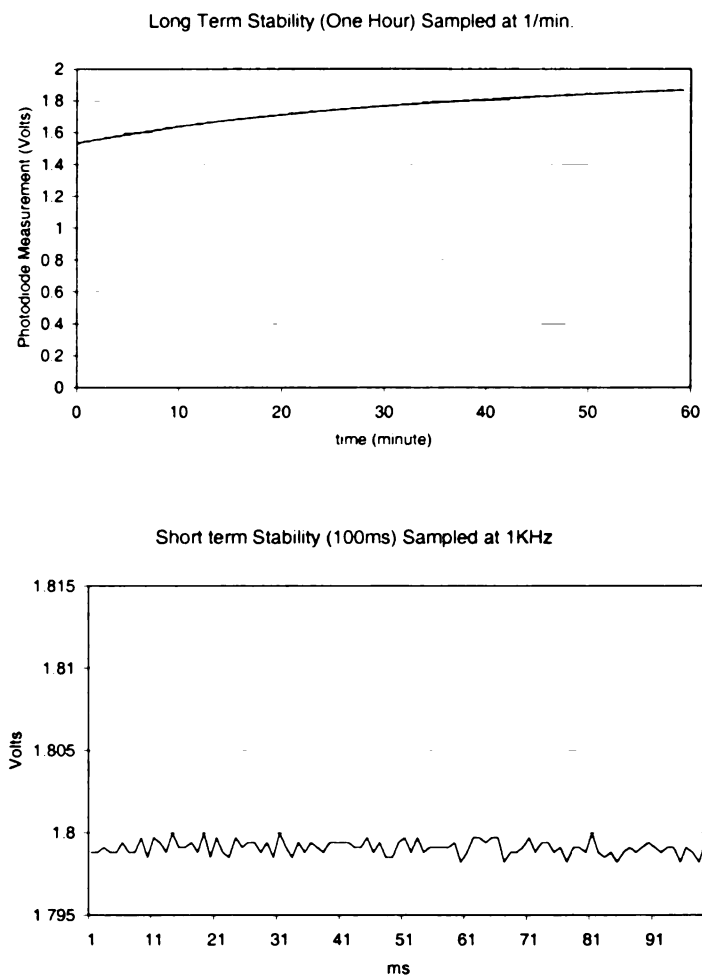


Figure 18. Long Term and Short Term Stability of Opti-Quip Xenon/Mercury Lamp.

It can be seen that the long-term and short-term stability is much better where the short-term fluctuation is less than 0.1% (standard deviation / amplitude). With such a stable source, tests conducted in a short period of time (< 1 minute) don't need to be UV-compensated.

4.3 Photo-Bleaching Study

One of the potential advantages of the FERIT system under development is that it is less susceptible to photo-bleaching. This phenomenon has been described in various publications for the EuTTA system where, under constant UV excitation, the fluorescent emission intensity decreases up to approximately 40% over a period of 30 minutes even though the sample is held at constant temperature [Tangyungyong and Barton, 1996; Caffrey, 1994]. Oxygen was identified as the main cause of this problem [Caffrey, 1994].

Such behavior not only imposes a problem for calibration, but also restricts the technique to be applied to transient processes or even steady state situations. To resolve the calibration difficulty, the sample has to be sealed inside a vacuum to prevent oxygen from interacting with temperature probe [Liu and Campbell, 1995].

The Eu(hfa)_3 system developed in our study was less susceptible to the above problem. A sample surface coated with the temperature probe was illuminated by UV light and held at room temperature. The gray scale intensity was imaged by the ORBIS camera. A photodiode was also used to monitor and compensate for excitation fluctuation. The tests were conducted over a period of one hour and one image was taken every two minutes. The results are shown in Figure 19. The initial fluorescent intensity was approximately 2500DU while the digitizing resolution was set to 12 bit. The percentile decreases are approximately 1.0% and 2.1% respectively for an annealed and an unannealed film. No significant decrease in intensity was observed. The UV excitation level applied was approximately 1W/m^2 which is similar to test conditions typically for the EuTTA system.

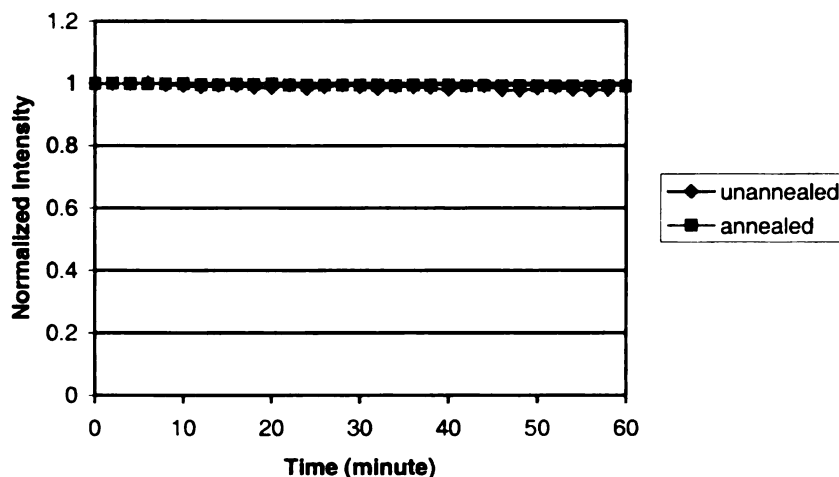


Figure 19. Fluorescent Emission Intensity as a Function of Time.

4.4 Linearity Study of UV Excitation and Fluorescent Emission Intensity

Different intensity levels of UV excitation were used to illuminate the fluorescent film at room temperature and the ORBIS camera was used to obtain images of the fluorescent emission. The Opti-Quip 200W Xenon-Mercury lamp was used as the light source. UV excitation was selected by an Omega band pass filter 365HT25. A set of Oriel neutral density filters was selected and placed between the UV source and UV band pass filter to realize various excitation levels (Figure 20). Actual excitation intensity was monitored by the OPT301M photodiode mounted next to the sample and voltage outputs were converted to UV intensities according to Equation 6.

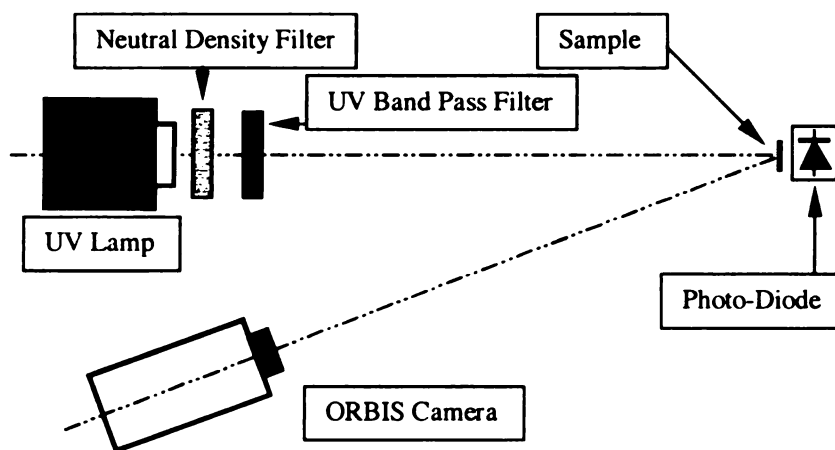


Figure 20. Experimental Study of Linearity between Fluorescent Emission and UV Excitation.

The optical densities and the corresponding transmittance of the neutral density filters selected are listed in the following table:

Table 2. Transmittance and Optical Density of Neutral Density Filters.

Optical Density (O.D.)	Transmittance
2.0	0.010
1.0	0.100
0.5	0.316
0.4	0.398
0.3	0.501
0.2	0.631

Where the quantities are related by:

$$O.D. = -\text{Log}_{10} T$$

Eqn. [8]

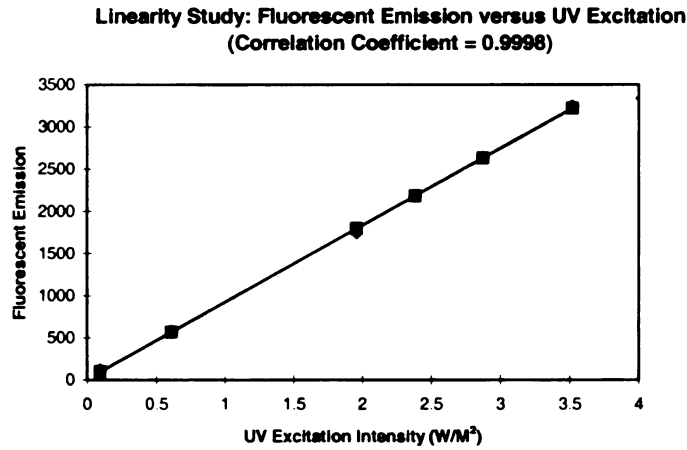


Figure 21. Fluorescent Emission Intensities as a Function of UV excitation Intensities.

A high degree of linearity was observed for the UV intensity range tested (Figure 21).

A higher frame rate can be achieved to a certain degree by increasing the UV excitation intensity since exposure time can be reduced accordingly. This is especially true for a frame transfer CCD sensor which doesn't have the data readout overhead. However, care must be taken to ensure that an increase in UV excitation intensity would not cause other problems:

- **Linearity:** Saturation effect will start to set in for increasing UV intensity, as described in Chapter 2. Measurements similar to the above study should be conducted to confirm that the linear relation is still valid.

- Photo-bleaching: High UV excitation has the potential of permanently destroying the chemical bonds of the fluorescing molecules, even if other environmental factors are not present.
- UV heating: Since the quantum efficiency of the fluorescent molecules is always less than 100%, the absorbed energy will be converted to electromagnetic energy by emitting photons or to thermal energy which causes a heating effect on the surface. The extra energy due to internal conversion and vibrational relaxation of the excited molecules will also be converted to thermal energy of the film. Such a heating effect has the potential to interfere with the designed experiments and to affect temperature measurement accuracy. An estimate of the energy flux across the surface is necessary and should be compared with UV heating to ensure the latter is negligible or its effect falls within the measurement accuracy tolerance. Such an effect is most likely to be not significant for experiments involving forced convection. However, an UV excitation intensity of 1.0W/m^2 could induce about 0.1°C surface temperature increase for a natural convection situation. The above estimate is derived from an energy balance analysis of a control volume enclosing a plate with one surface heated

by a 1.0W/m^2 energy flux and cooled on both surfaces by natural convection, assuming convective heat transfer coefficient of $5\text{W/m}^2\text{K}$ (natural convection). The UV excitation intensity used for our study is approximately $0.1 \sim 0.2 \text{ W/m}^2$ to minimize the heating effect.

4.5 Calibration Curve for Fluorescent Emission Intensity and Temperature

The relation between fluorescent emission intensity and temperature is determined experimentally for the temperature region of interest. A test rig was built to facilitate the experiment, as shown in Figure 22. Two low thermal conductivity (composite wood) frames hold the test plates together by four screws. The top frame is $1.5 \times 1.5 \text{ in}^2$ outside and $0.9 \times 0.9 \text{ in}^2$ for the inside, $\frac{1}{4}$ in thick. The bottom frame is $1.5 \times 1.5 \times \frac{1}{4} \text{ in}^3$. The two test plates are aluminum blocks ($1.0 \times 1.0 \times \frac{1}{16} \text{ in}^3$) to ensure uniform lateral temperature distribution. A MINCO thermofoil heater (model #: 2-HK5318R26.1L12A) is sandwiched between the aluminum plates to provide heating to desired temperatures. Steady temperature is reached when the energy generation and heat dissipation by natural convection is balanced for the rig.

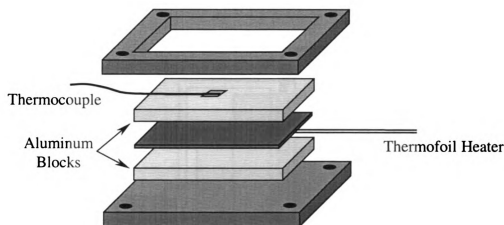


Figure 22. Calibration Rig.

An important factor that will determine the accuracy of the calibration relation is the ability to measure the surface temperature accurately by thermocouples or some other means as standard. The thermocouples used in the experiments were calibrated by an Omega DP95 digital RTD thermometer which was factory calibrated to an accuracy of 0.01°C (Figure 23). A cylindrical block was made of aluminum with drilled holes to accommodate the thermocouples and the RTD probe (Appendix H). The $1/8''$ holes for thermocouples are small enough to minimize the temperature gradient along the holes but large enough to accommodate most thermocouple types. Three-quarters of the aluminum cylinder are immersed in the coolant to maintain a uniform temperature around the thermocouple and the RTD tip region. A constant temperature bath (NESLAB RTE-140) was used to maintain the temperature of the block. The thermocouples were calibrated from 0°C to 90°C with a 5°C interval. The thermocouple data acquisition board (CIO-DAS802/16 and CIO-EXP16) has a temperature resolution of 0.125°C and the temperature fluctuation of the constant temperature bath is 0.1°C as specified by the manufacturer.

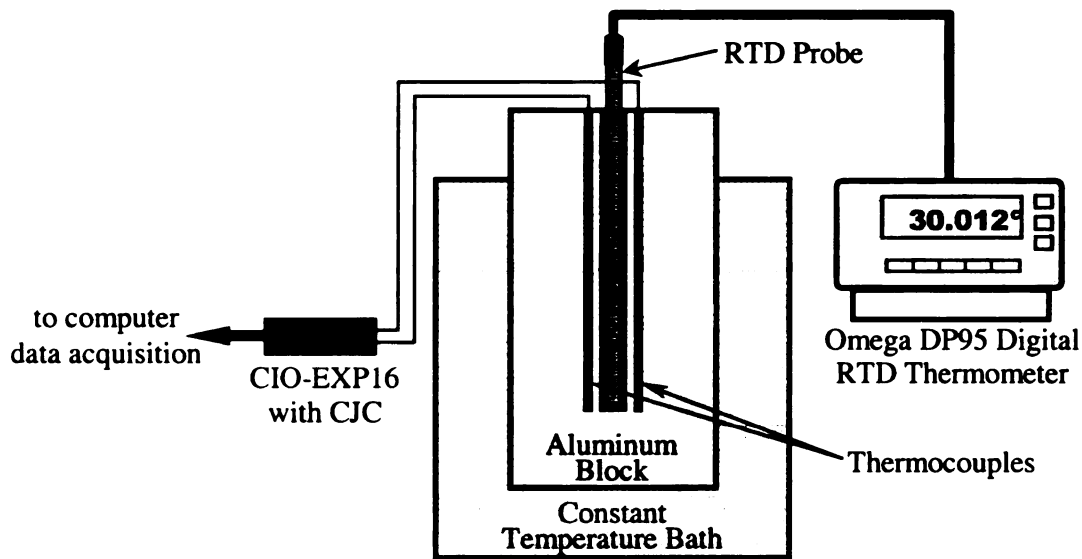


Figure 23. Setup for Thermocouple Calibration.

After the constant temperature bath reaches the set temperature and stabilizes for ten minutes, 200 data points were read at 20Hz rate with the CIO-DAS802/16 and CIO-EXP16 boards. The averages were calculated and the RTD readings were also recorded. These were repeated until measurements for all the desired set points have been performed. The measured data were compared with the RTD readings and the differences were adjusted in the thermocouple measurement program (TCDAQ.exe) for each input channel. The calibration block can accommodate a total of eight thermocouples, and the data acquisition board has sixteen input channels so only half of the inputs were used.

Two methods for attaching the thermocouple to the sample surface were investigated: Epoxy adhesive configuration and thin tape adhesive configuration (Figure 24).

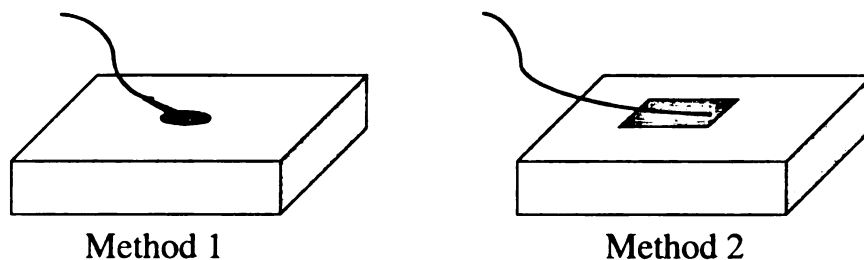


Figure 24. Attachment Methods for Thermocouples.

For method one, a tiny volume of Omega 101 A/B epoxy was applied to the tip of the thermocouple and carefully set onto the sample surface. The epoxy spot size is about 1mm wide and 0.5mm thick. Several problems were observed for such a method: (1) it was very sensitive to room/building air circulation. When the block is at about 75°C, the fluctuation is larger than 0.2°C. (2) The thermocouple wires near the tip revealed a fin effect (thermal drain) which introduced systematic error. At the same heater power level, this method measured approximately 2°C below the value obtained from method two when the block is at 75°C. (3) The epoxy permanently set the thermocouple onto the surface after it cures so that the calibrated thermocouple might not be reusable.

In method two (thin tape), the thermocouple tip was wetted by silicon heat sink paste before it was taped onto the sample surface using thin high temperature tape (by CHR/FURON Division). The heat sink paste ensures that the thermocouple is in good thermal contact with the surface. This approach reduced the temperature fluctuation to 0.1°C and provided thermal grounding for the thermocouple to eliminate the fin effect. A resistive network model was used to estimate the effect of the tape since it has the potential to introduce extra thermal resistance to the surface, as shown in Figure 25.

has to be sent back to the manufacturer which is time consuming and costly. Each fluorescent image was the average of three consecutive frames. Each intensity measurement was obtained by sampling at approximately 1 mm from the thermocouple tip. The measurement should be done as close to the thermocouple tip as possible to ensure both methods are measuring the same temperature, but not in the tape region where there is an abrupt intensity change due to the non-fluorescing tape. The calibration result is shown in Figure 26 with ORBIS camera operating at 12 bit mode. The measurement errors for the intensities were estimated in the following section. The fluorescent emission intensity decreases with increasing temperature, almost linearly. Most non-linearity occurs near room temperature (20°C) and at high temperature (80°C). This calibration relation was fitted with a seventh degree polynomial. The polynomial was then used to create an intensity ~ temperature table for the calibrated range with 0.01°C interval. This table will be used by the hybrid-linear search algorithm to determine temperature of future measurements.

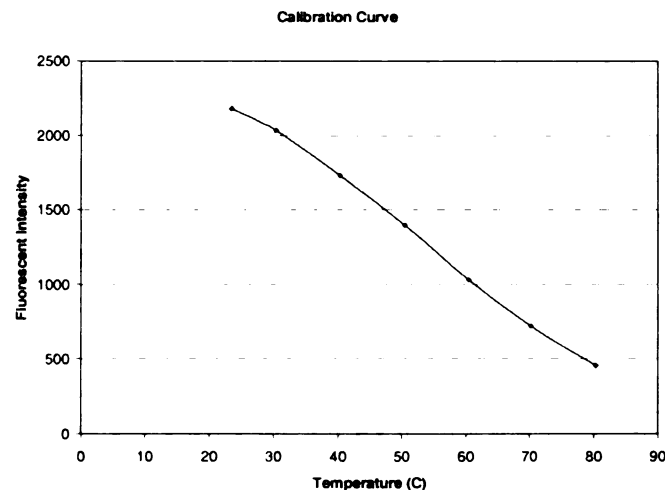


Figure 26. Calibration for Fluorescent Emission as a Function of Temperature.

4.6 Estimate of Temperature Measurement Errors

In order to derive temperature measurements using the ratiometric approach, measured fluorescent emission intensities will be compared with the calibration curve which describes the temperature-dependent behavior of the relative fluorescent emission intensities. Since the intensity measurements at the time of interest and the calibration relation both have uncertainties and the measurements are independently performed, they both contribute to the total measurement error:

$$\sigma_{total} = \sqrt{\sigma_{calib}^2 + \sigma_{test}^2}, \quad \text{Eqn. [9]}$$

with σ_{calib} being the error of the calibration and σ_{test} being the error of intensity measurement at time of interest.

σ_{test} is comprised of two components:

$$\sigma_{test} = \sqrt{\sigma_{intensity}^2 + \sigma_{TC}^2}, \quad \text{Eqn. [10]}$$

where σ_{TC} is the error of the thermocouple reading for the reference temperature and $\sigma_{intensity}$ is the temperature error associated with the intensity measurement error which can be determined from the following factors:

- Dark noise
- Shot noise
- Read noise
- Flicker noise (UV source)
- Background noise
- Digitizing error

$$\sigma_{intensity} = \sqrt{\sigma_{dark}^2 + \sigma_{read}^2 + \sigma_{shot}^2 + \sigma_{flicker}^2 + \sigma_{bg}^2 + \sigma_{digi}^2}; \quad \text{Eqn. [11]}$$

It has been shown that the dark noise signal grows proportionally with time. It will not become significant unless the exposure time exceeds 2 seconds since the ORBIS camera is cooled to -20°C , and equivalent noise of 1 DU will require approximately 193 seconds exposure time, which can easily be verified by the method used to evaluate the dark noise in previous section.

The read noise is less than one detector unit (DU) (section 4.1.1) since the CCD was design to read at relatively low speed (<1 Mbyte/s) as compared to ~ 15 Mbyte/s of ordinary video camera.

Calculation showed that shot noise can reach about 6 ~ 7 DU and it constitutes the major part of the total noises. It is the result of the limited electron potential well and the governing statistics. For given equipment, improvement can be obtained by increasing

the exposure time or averaging multiple frames. Both have the same effect of increasing sampling size to reduce error. The tradeoff is that it will take a longer period of time to obtain a measurement. As governed by statistics, the reduction in shot noise is proportional to $1/\sqrt{N}$, where N is the sample size.

Flicker noise is primarily determined by the quality of the UV source, as illustrated in section 4.2. Even a good UV source will drift in long term (~ 1 hour). It is advised to monitor the UV intensity if the measurement will be conducted for a relatively long period of time (> 10 minutes). By monitoring and compensating for the UV fluctuation, the flicker noise can be minimized to less than 1 DU.

The background noise depends on the characteristics of the background light source and the camera exposure time. To realize the full potential (dynamic range) of the CCD camera, it is advised to conduct measurement in low ambient light condition. Since the background is subtracted from the image to obtain net measurement, the noise effect is minimized and not significant. The background effect can become significant if it comprises a significant part of the total signal, especially when the exposure time is short (~ 0.01 s) since the background (room) light source is fluctuating at about 100Hz. In this study, the background level is approximately 5% of the total signal.

Digitizing noise will become significant when the signal is very faint or exposure time is too short. It represents the error introduced while quantifying a constant physical quantity (such as voltage) by the equipment with a numeric number. In the case of digital camera,

the magnitude of such error is always 1 DU, the smallest unit used to represent the intensity.

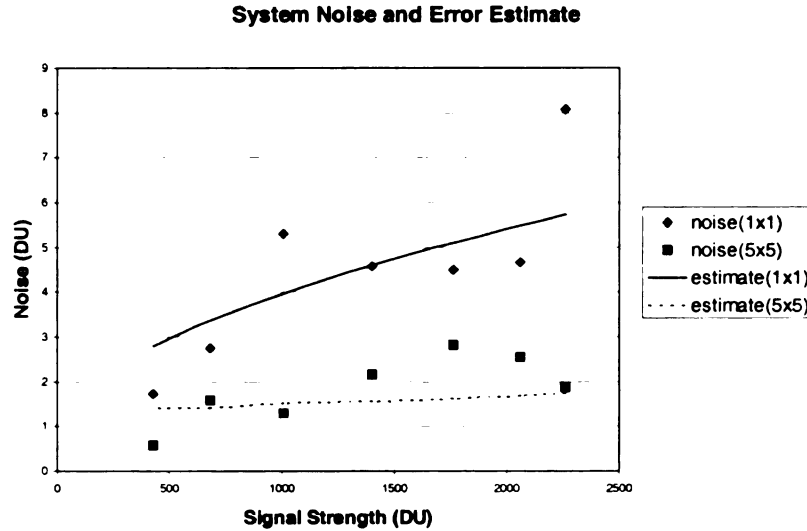


Figure 27. Comparison of Measurement Errors and Error Estimate Model.

To evaluate the error estimation model (Eqn. [9] to Eqn.[11]), results from experimental measurements of various gray scale intensities were compared to the values given by the estimation model, as shown in Figure 27. Seven intensity levels between 400 DU and 2300 DU were tested, which covers most of the intensity range used in this study. At each intensity level, ten images were taken from which statistical analysis was performed. The blue scattered data points were the standard deviation of ten measurements for a single pixel, while the data in red color were the standard deviation of ten measurements of 25 averaged pixels (5 x 5). The blue and red lines were the estimated errors for the above two cases. It can be seen that the magnitude of noise increased with signal strength, which is a characteristic of a shot-noise dominant system. Averaging reduces the noise level to some extent until other sources of error become dominant. The measurement results and the estimate model agree with each other fairly well.

In summary, the total noise of a single measurement (pixel) is approximately 8 DU with the CCD sensor near full scale (by extrapolating from the estimation model). By introducing averaging to reduce shot noise, the total noise can be reduced to ~ 3 DU (best case) when other noise sources become dominant.

For the calibration error, it will have all the above errors and possibly one additional source of error, the error introduced by the mathematical representation of the calibration relation. Since calibration is conducted only at discrete points (temperatures), a polynomial or other type of model is used to interpolate a value between adjacent points, which will introduce errors. The highest degree polynomial should be used for a given number of calibration points, e.g., a seventh degree polynomial will give a best fit for seven calibration points. The error given by such a model is less than 0.01°C. The errors given by polynomials of different degrees are illustrated in Appendix E.

With the above analysis, we can derive an estimate of the total temperature measurement error:

$$\sigma_{calib} (^{\circ}\text{C}) = \sigma_{calib}(\text{DU}) / \text{Slope_of_Calib_Curve}; \quad \text{Eqn. [12]}$$

$$\sigma_{test} (^{\circ}\text{C}) = \sigma_{test}(\text{DU}) / \text{Slope_of_Calib_Curve}; \quad \text{Eqn. [13]}$$

The following are calculations for the worst and best cases for $\sigma_{intensity}$:

$$\begin{aligned}
\sigma_{intensity}^{worst} &= \sqrt{(\sigma_{dark}^2 + \sigma_{read}^2) + \sigma_{shot}^2 + \sigma_{flicker}^2 + \sigma_{bg}^2 + \sigma_{digi}^2} \\
&= \sqrt{0.64^2 + 6.0^2 + (3000.0 * 0.001)^2 + 0.0^2 + 1.0^2} \quad \text{Eqn. [14]} \\
&= 6.8 (DU) = 0.24^\circ C
\end{aligned}$$

$$\begin{aligned}
\sigma_{intensity}^{best} &= \sqrt{(\sigma_{dark}^2 + \sigma_{read}^2) + \sigma_{shot}^2 + \sigma_{flicker}^2 + \sigma_{bg}^2 + \sigma_{digi}^2} \\
&= \sqrt{0.64^2 + 0.0^2 + (3000.0 * 0.001)^2 + 0.0^2 + 1.0^2} \quad \text{Eqn. [15]} \\
&= 3.2 (DU) = 0.11^\circ C
\end{aligned}$$

Taking into account the error of thermocouples ($\sim 0.1^\circ C$, Eqn. [10]), we can conclude that the best and worst case of total measurement errors are approximately $0.21^\circ C$ and $0.37^\circ C$. It can be observed from the equations that substantial frame averaging is required (> 25 frames) in order to approach the best case limit $0.21^\circ C$ (the shot noise term will decrease by a factor of $\sqrt{25} = 5$ which will make this term insignificant compared to the other terms).

4.7 Moisture Effects

Future applications of the fluorescence-based technique might require that the film be exposed to water moisture or even be in direct contact with water. The photo-bleaching experiment suggested that the $\text{Eu(hfa)}_3/\text{PMMA}$ system is not susceptible to normal room conditions, such as the presence of oxygen and the trace amount of moisture in the air, as contrast to the severe photobleaching behavior for the EuTTA system under the same

conditions [Caffrey, 1994; Barton, 1996]]. How the film behaves in extreme condition such as in water at room temperature will be the subject of this test. If significant change of its behavior is observed, further tests of intermediate moisture concentration levels may need to be investigated.

An aluminum block coated with a temperature-sensitive fluorescent film was placed in a container filled with distilled water where the fluorescent film was approximately 2 mm below the water surface. A thermocouple was attached to the surface to monitor possible temperature fluctuation of the film. The experimental setup is shown in Figure 28.

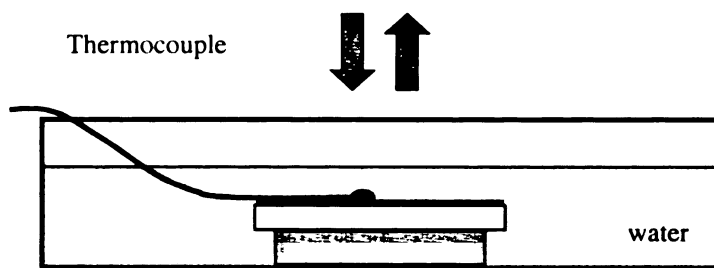


Figure 28. Schematic of Moisture Effect Experiment.

The UV excitation level used was approximately 1W/m^2 (typical for all experiments performed here) and no significant temperature change was observed during the test ($< 0.2^\circ\text{C}$) so that temperature variations will be ruled out as a parameter to cause any fluorescent intensity change. An image was taken every two minutes over a one-hour period. Three frames were averaged to obtain a measurement (image). The initial fluorescent emission intensity was approximately 2500DU at 12 bit resolution. The non-dimensional fluorescent emission intensities over time for an annealed and an unannealed

film are shown in Figure 29, and the percentile decreases in intensity over time are approximately 1.4% and 3.6%, respectively.

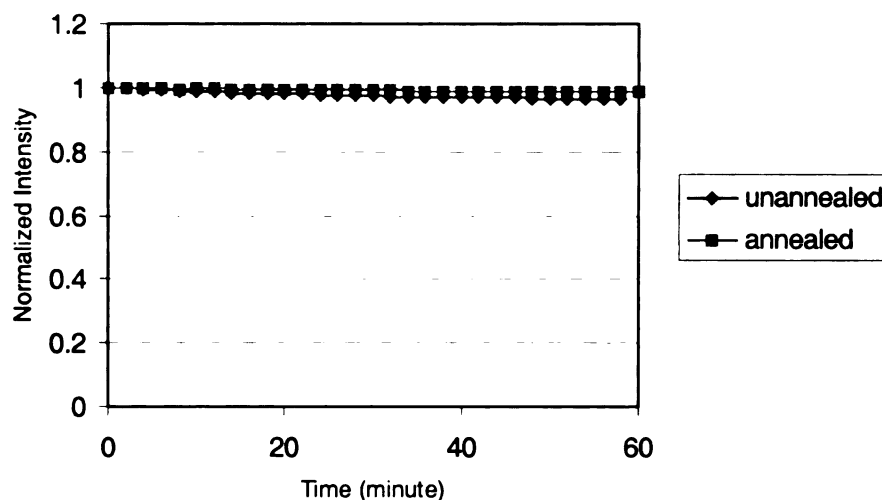


Figure 29. Moisture Effect on Fluorescent Emission Intensity.

The intensity decreased about 3.6% for unannealed film over a period of one hour and the percentile change is about twice that of the test conducted in ambient air (~2.0%).

Water molecules will compete with the ligands for the central ion (Eu^{3+}) which will result in a decrease in fluorescent intensity. The above test suggested that the temperature probe encapsulated by the polymer (PMMA: poly methyl-methacrylate) is effectively protected from moisture (water). This implies that the fluorescent film can be applied directly to an aqueous environment such as a water flow system and that special measures to account for variations in relative humidity need not be applied when accuracy better than 1~4% isn't required.

4.8 Reproducibility Study

4.8.1 Reproducibility between Neighboring Pixels

As an important aspect of thermographic system, the spatial response uniformity will need to be evaluated. This test aimed at evaluating the consistency of measurement results provided by individual CCD sensing element (pixel) at the given calibration points/conditions. It is desirable that all pixels produce similar calibration relations (fluorescent emission intensity as a function of temperature).

The reproducibility among neighboring pixels was investigated and the measurement locations are illustrated in Figure 30. A group of pixels (2 x 5) was chosen very close to the thermocouple junction tip. The intensities of these pixels for the range of calibration temperatures (20°C ~80°C) were measured.

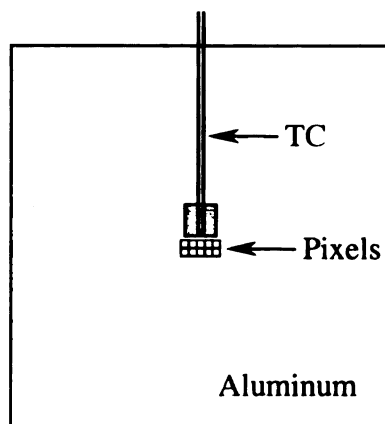


Figure 30. Measurement Locations for Neighboring Pixels.

Net fluorescent intensities were obtained by subtracting the background from the original image, then they were compensated for UV excitation fluctuation. Due to the slight non-uniform responsivity among pixels (even for the same illumination levels), the intensities of the ten pixels were scaled to the same starting intensity (at 23°C). The subsequent intensity variations among the ten pixels at different calibration temperatures are shown in Figure 31. The intensities of the ten pixels at the same temperature are grouped together, in temperature-wise increasing order, i.e., 23, 30, 40, 50, 60, 70, and 80. The variation changes from approximately 8 DU or 0.36% at high intensity (room temperature) to 4 DU or 0.87% at low intensity (high temperature ~80°C), which agrees with the error estimate for the system (shot-noise limited). This is not surprising since even though each pixel in this test behaves as an individual sensor, it shows a calibration relation similar to others since they are at the same temperatures.

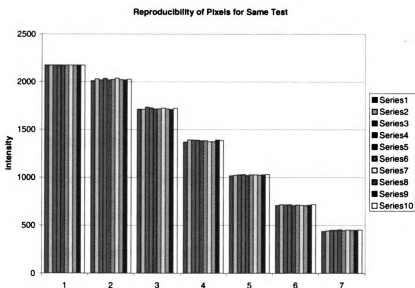


Figure 31. Reproducibility among Neighboring Ten Pixels.

4.8.2 Reproducibility Tests Before and After Annealing

The objective of these tests is to study the reproducibility of the calibration relation. The calibration test was repeated three times for the same sample, from room temperature to 80°C with a 10°C interval, before and after the film was thermally annealed. The results are summarized in Figure 32 and Figure 33, respectively.

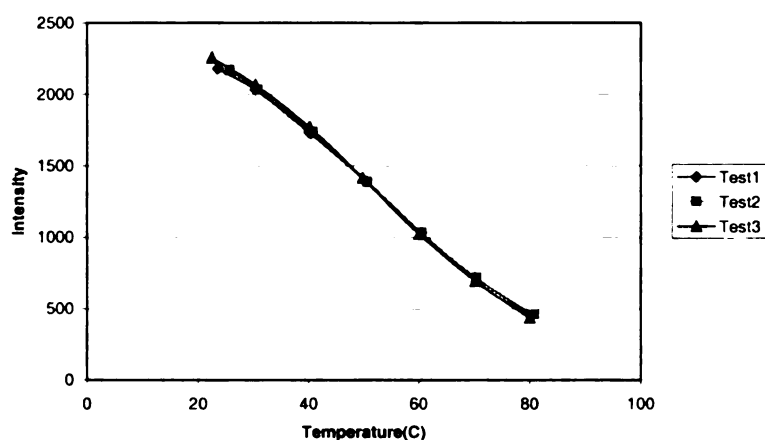


Figure 32. Reproducibility of Calibration Relation before Annealing.

Since the starting temperatures and fluorescent emission intensities are different, we chose to match the intensity at 50°C so that the shape difference between these calibration relations are most easy to observe. The calibration relation is fairly linear except for the low temperature and high temperature ends. The three repeated measurements overlap each other very well, which suggests good reproducibility. The slopes (absolute values) increase slightly from the first test to the last test. This might be explained by the annealing effect since repeated tests caused the fluorescent film to experience thermal

cycling close to the polymer glass transition temperature ($\sim 100^{\circ}\text{C}$), which made the calibration relation move slightly towards the behavior of a film that has been annealed. The slope is approximately $-1.42\% / ^{\circ}\text{C}$. To calculate the slope, the intensity is normalized by the initial intensity at room temperature.

The film was then annealed at 120°C (the glass transition temperature of PMMA is approximately 100°C) for approximately half an hour, followed by three repeated calibration measurements. Similarly, the intensity at 50°C is matched for the comparison. Linear behavior is observed from room temperature up to 60°C . The slope in this case is approximately $-1.55\% / ^{\circ}\text{C}$, which (absolute) is about 8.3% steeper than the unannealed case.

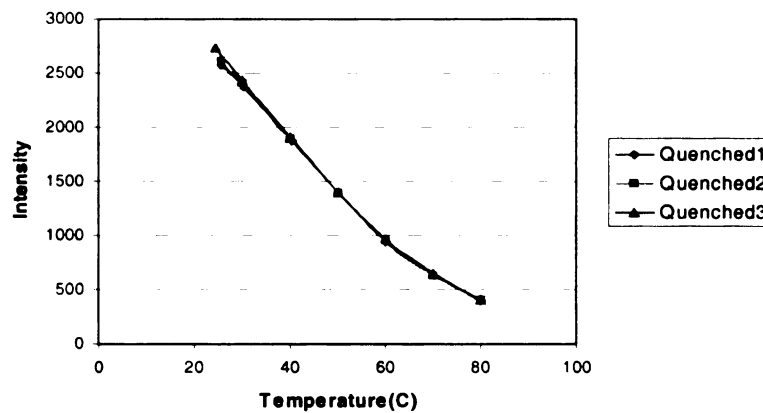


Figure 33. Reproducibility of Calibration Relation After Annealing.

The variations within the three calibration measurements of the annealed and unannealed films are approximately 19 DU and 23 DU respectively, which corresponds to errors of approximately 0.47°C and 0.67°C .

The slope determines the shape of the calibration relation and the system's temperature sensitivity. Even though good reproducibility was observed for calibration behavior before and after the quenching, care must be taken to ensure proper calibration is used for films which have undergone different thermal treatments. An unannealed film might behave like an annealed one if the test is conducted close to the glass transition temperature of the polymer. It is recommended that the fabricated films be annealed wherever the situation allows. Possible errors introduced by improper use of calibration relations for films with different annealing history will be discussed quantitatively in section 4.9.

The shape difference before and after annealing is more obvious by overlaying the two sets of data in dimensionless coordinates:

$$\text{Temperature}^* = (T - T_{\min}) / (T_{\max} - T_{\min});$$

$$\text{Intensity}^* = (I - I_{\min}) / (I_{\max} - I_{\min});$$

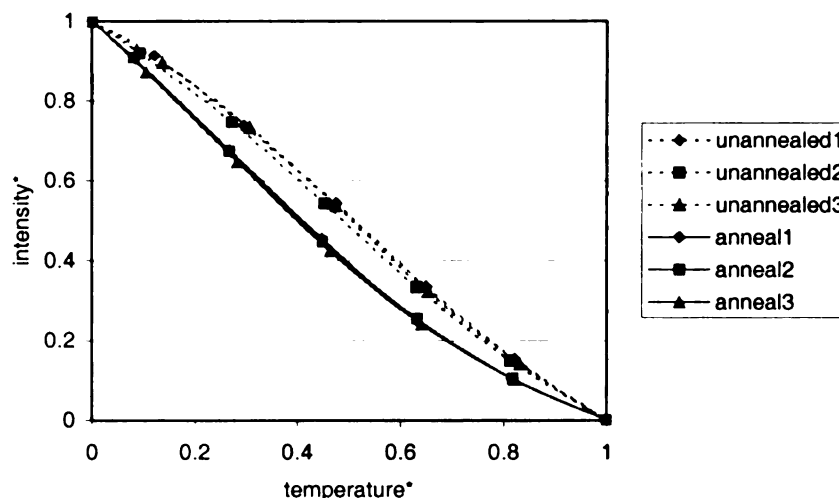


Figure 34. Effect of Annealing.

Annealing changes the shape of the calibration curves and different calibration relations should be used for films which have undergone different temperature treatments. An error as high as 5°C could be introduced if the inappropriate calibration relation is used, as explained quantitatively in the section 4.9 for the effect of annealing.

4.8.3 Hysteresis

Testing was also performed during which the annealed sample was first heated from room temperature up to 80C and then cooled back down to room temperature with 10C interval, to investigate the significance of any hysteretic behavior. For each measurement, it took approximately 15 minutes to reach the temperature setpoint and another ten minutes for it to stabilize. Each intensity measurement was average of three frames and

the

illu

The

mic

effe

sys

4.9

From

obse

the temperature was average of 100 data points sampled at 100Hz. The result is illustrated in the following figure.

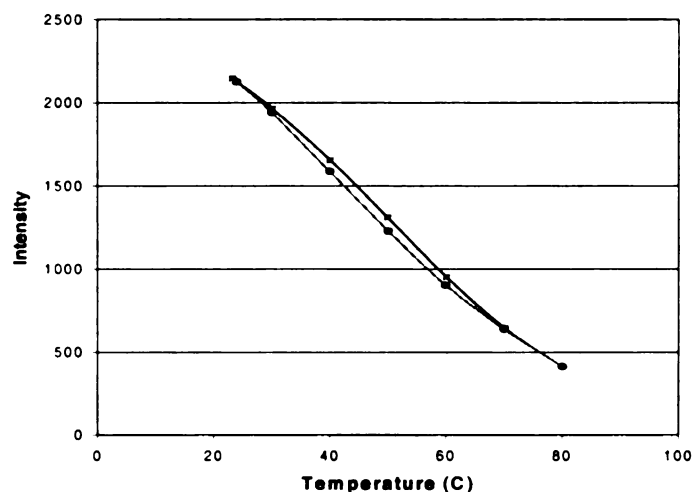


Figure 35. Fluorescent Emission as a Function of Temperature for a Heat-up and Cool-down Process.

The two curves for heating up and cooling down are matched fairly well except for the middle portion. More detailed investigation is recommended for the future in which the effects of temperature ranges and number of repeats on the hysteretic behavior should be systematically studied.

4.9 Annealing Effects

From the reproducibility experiments for the annealed and unannealed films, it was observed that annealing increases the slopes of the calibration curve over 8%, which is

significant. Failure to use the appropriate calibration table might result in temperature measurement error as high as 5°C for the entire temperature range of 60°C. The linearity of an annealed film near room temperature is better than that of an unannealed one, which is a desirable feature. Thermal cycling due to repeated tests on an unannealed specimen will have similar effects as annealing, especially if the test temperature is very close to the glass transition temperature of the polymer. This will create potential errors in temperature measurement since the unannealed calibration curve used to deduce temperature might not be valid. One should anneal the film (above the polymer glass transition temperature for approximately half an hour) whenever possible and use the appropriate calibration relation to derive accurate temperature measurements.

4.10 Effect of Fluorescent Probe Concentration

Studying the effect of fluorescent probe concentration on the calibration relation will help the user to choose an appropriate concentration level for particular applications, and it will also provide some insights regarding how possible probe non-uniformity might affect the final temperature reading. Fluorescent probe concentration is a determining factor for the fluorescent signal strength. Increasing the concentration has the potential to boost signal output level. However, an extremely high probe concentration may result in poor adhesion to the sample surface since the polymer acts as a primary binder to both the temperature probe and the surface of application. At high probe concentration, some of the surface area might be occupied by the probe molecules that would result in a weak bond.

Samples with probe concentrations of 50wt% and 12.5wt% were fabricated as compared to the test samples of 25wt% studied earlier. Calibration relations were measured for these two samples and compared.

The temperature-dependent fluorescent emission intensity of a quenched film with 50wt% is shown in Figure 36. The slope is approximately $-1.56\% / ^\circ\text{C}$.

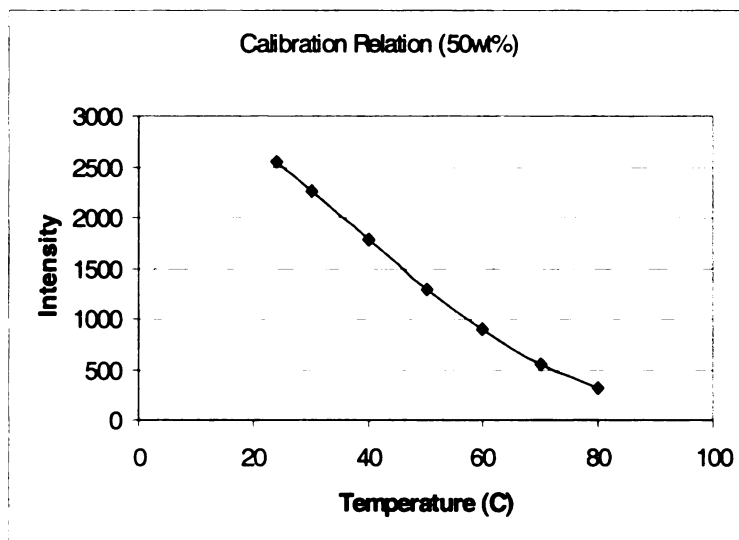


Figure 36. Calibration for Fluorescent Film of 50wt% Concentration.

Testing was also conducted for a quenched film with 12.5wt% probe concentration and the result is shown in Figure 37. The slope is $-1.54\% / ^\circ\text{C}$.

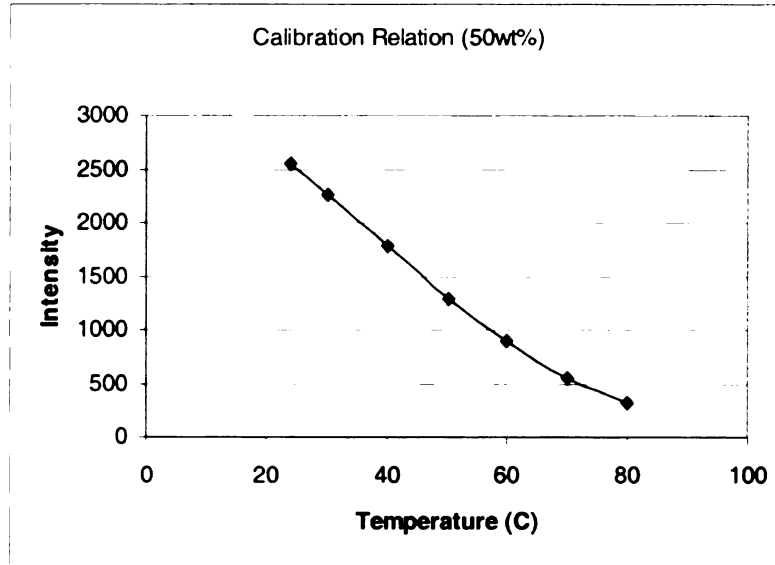


Figure 37. Calibration for Fluorescent Film of 12.5wt% Concentration.

Compared with the slope of calibration for the concentration range tested (12.5wt%, 25.0wt%, and 50.0wt%), there was a slight increase of the slope (absolute value) with increasing concentration but it was not significant among the three samples tested (difference less than 2%). Previous study conducted for very low probe concentration (0.01%) suggested a slope of approximately $-0.1\% / ^\circ\text{C}$.

Figure 38 shows the shapes of the calibration relations in dimensionless coordinates for the three different concentration levels tested. The two curves of higher concentration (25wt% and 50wt%) are very similar but the one with 12.5wt% deviates from the other two slightly.

4.1

Th

no

an

4

T

t

s

A

flu

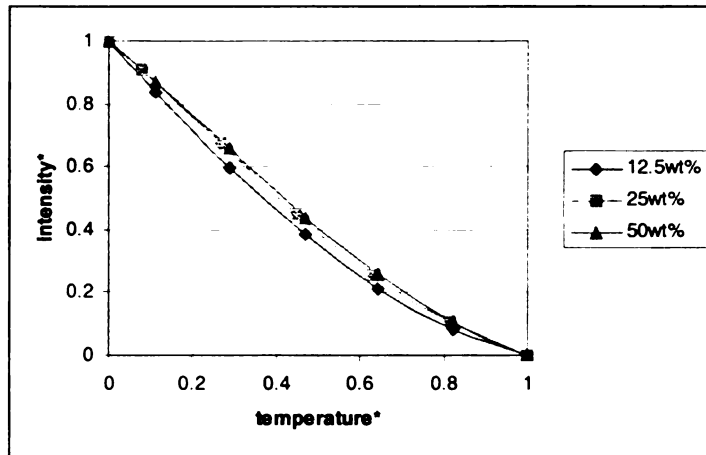


Figure 38. Effect of Temperature Probe Concentration.

4.11 Aging Effect

Three repeated measurement (Figure 32) were conducted over a period of one month and no significant aging behavior was observed, which is not surprising since photobleaching and moisture tests suggested the system is not sensitive to the ambient condition.

4.12 System Dynamic Response

The imaging system's dynamic response will determine how fast the system can capture time dependent phenomena. The FERIT system was applied to measure the time-varying surface temperature of a metallic (aluminum) thin film heated by a pulse source.

A thin metallic film (30mm x 8mm x 0.03mm) was coated with the temperature sensitive fluorescent film and its two ends were connected to a heating source, as shown in Figure

39. The film was initially at room temperature. The amplitudes of the square wave pulse are 1 VDC maximum and 0 VDC minimum. Three different pulse periods were tested: 10s, 5s, and 1s with 50% time at maximum and 50% at minimum. The DC current at 1.0 VDC was measured about 0.45 Amp, which is consistent with the heated foil resistance ($2.1\ \Omega$). The pulses were realized by sending timed high and low digital outputs through the data acquisition card to a solid state relay, which controlled the power to switch on and off. The ORBIS digital camera started taking images right before the pulsation began. Thirty frames were taken at 1.1s interval with an image size of 512x128 and exposure time of 0.5s. The image area (512x128) was chosen to be big enough (6"x1.5" in real space) to cover the whole metallic film but small to increase frame rate and save file storage space. This exposure time was chosen to obtain an initial (at room temperature) fluorescent intensity of approximately 70% (~ 2800 DU) of full scale (4095 DU).

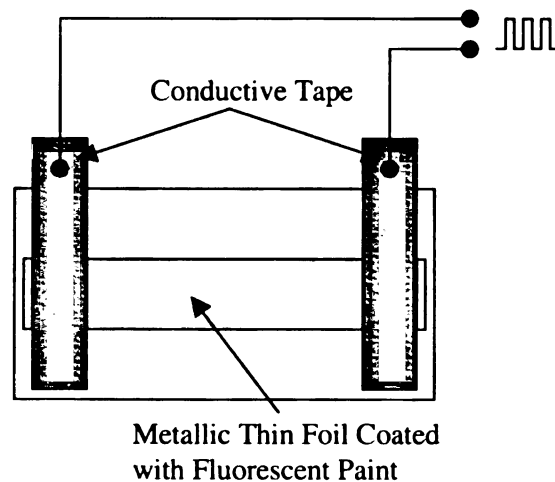


Figure 39. Dynamic Response Experiment.

The temperature of the foil surface over time was measured by FERIT for the three different pulse frequencies (0.1Hz, 0.2Hz, 1Hz). The results are illustrated in Figure 40, Figure 41, and Figure 42.

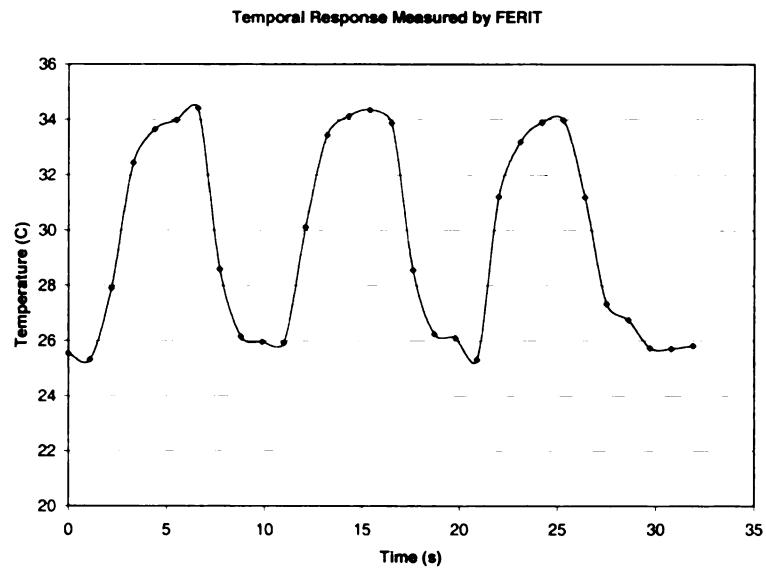


Figure 40. Time-Dependent Surface Temperatures - Pulse Period = 10.0s.

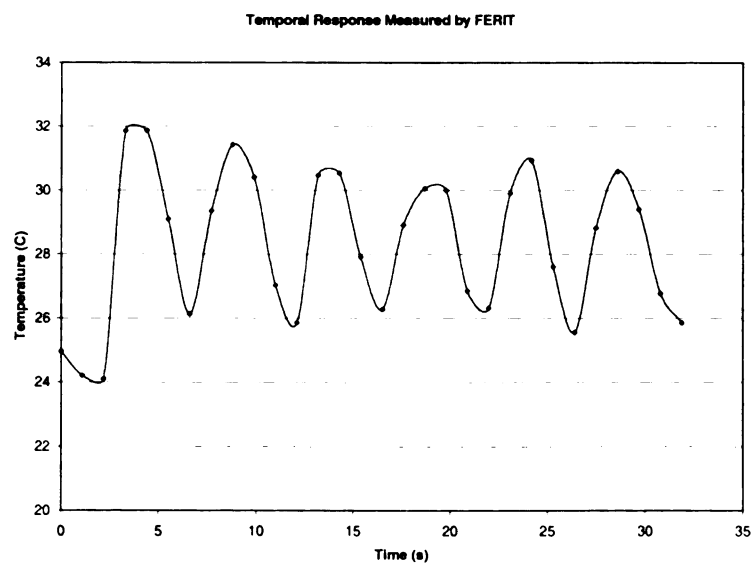


Figure 41. Time-Dependent Surface Temperatures - Pulse Period = 5.0s.

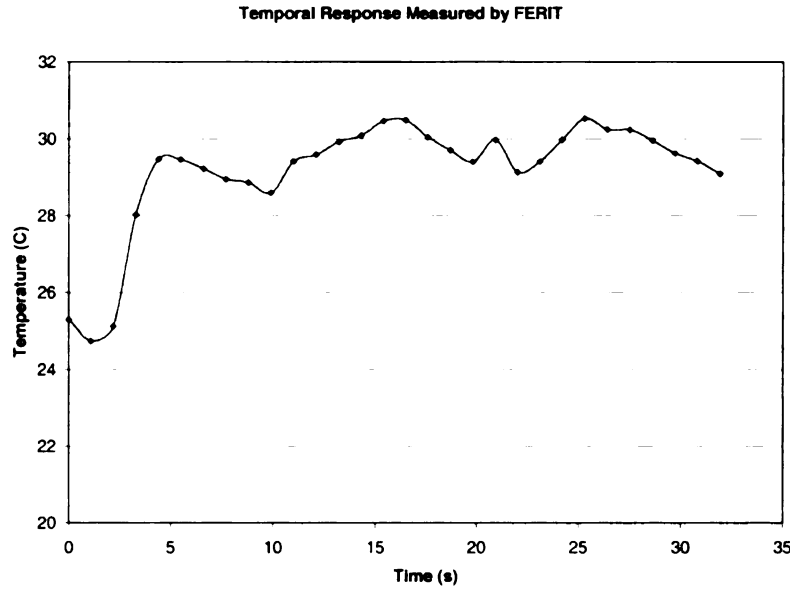


Figure 42. Time-Dependent Surface Temperatures - Pulse Period = 1.0s.

The system could resolve the slowly varying condition fairly well (Figure 40) since the frame period (1.1s) is much shorter than the pulse period (10.0s). When the pulse period was shortened to 5.0s, it barely caught the periodic characteristic of the heating (Figure 40). When the pulse period became comparable (1.0s) to the frame period (1.1s), the system was too slow to keep up with the changes.

The slow frame rate / dynamic response ($\sim 1\text{fps}$) of the system is primarily limited by the nature of full frame device used in this study, which can readily be improved (to $\sim 5\text{fps}$) by using frame transfer CCD. The operating principle of these two kinds of devices is explained in Chapter 6. Selecting smaller area of interest (AOI) might benefit the frame rate to some extent, but it will still be limited by the overhead of the mechanical shutter and slow exposure/readout sequence of full frame CCD.

Chapter 5

Applications

5.1 Temperature Distribution of Fin Cooled by Natural Convection

A rectangular aluminum fin with dimensions 6" x 1" x 0.027" was held by the calibration block at one end and the rest of the strip was exposed to ambient air. Temperature-sensitive fluorescent paint was deposited onto one side of the surface with an airbrush. The rig (base) was heated to various temperatures by a MINCO thin-foil heater (model: 2-HK5318R26.1L12A) and temperature gradients of different magnitudes were created along the fin by natural convection. One thermocouple was located at the center of the base (calibration rig) and six other thermocouples were spaced equally (20mm) along the exposed region, as shown in Figure 43.

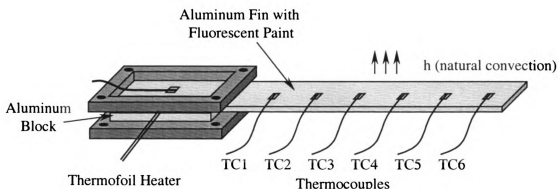


Figure 43. Extended Surface Cooled by Natural Convection.

The base temperatures were set from room temperature up to 80°C at intervals of 10°C by adjusting the power input to the heater. After the base temperature became steady, temperatures along the fin were measured by both the thermocouples and the FERIT method. Temperature distributions measured by the fluorescent method for $T_{\text{base}}=40^{\circ}\text{C}$ and $T_{\text{base}}=80^{\circ}\text{C}$ are shown in Figure 44 and Figure 45. Corresponding line profiles along the centerline of the fin are also plotted below the thermographic distributions.

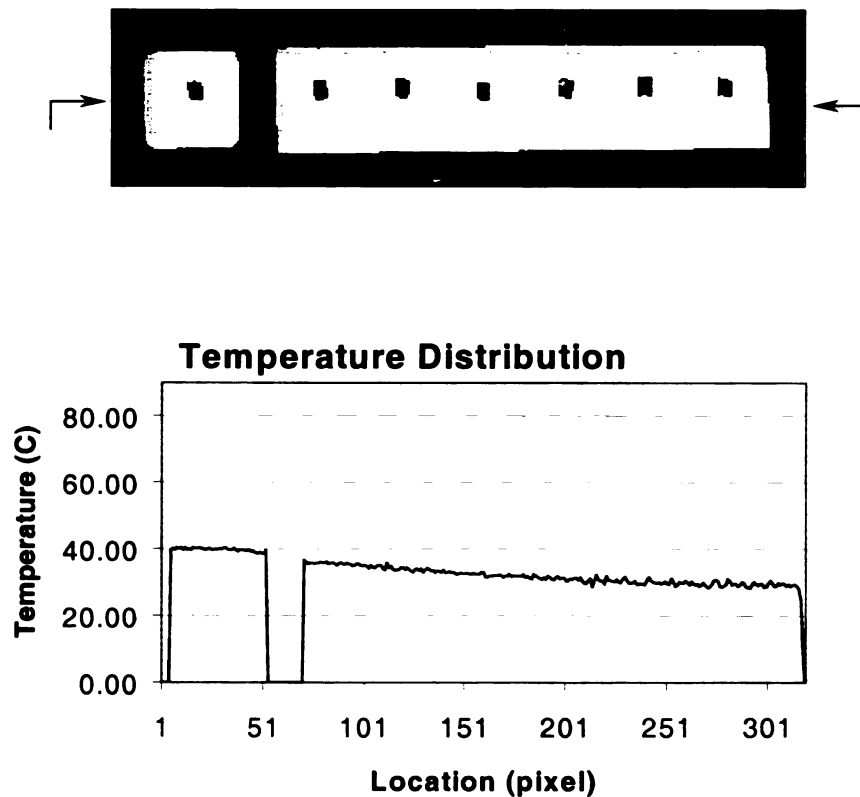


Figure 44. Temperature Distribution along Aluminum Fin - $T_{\text{base}} = 40^{\circ}\text{C}$.

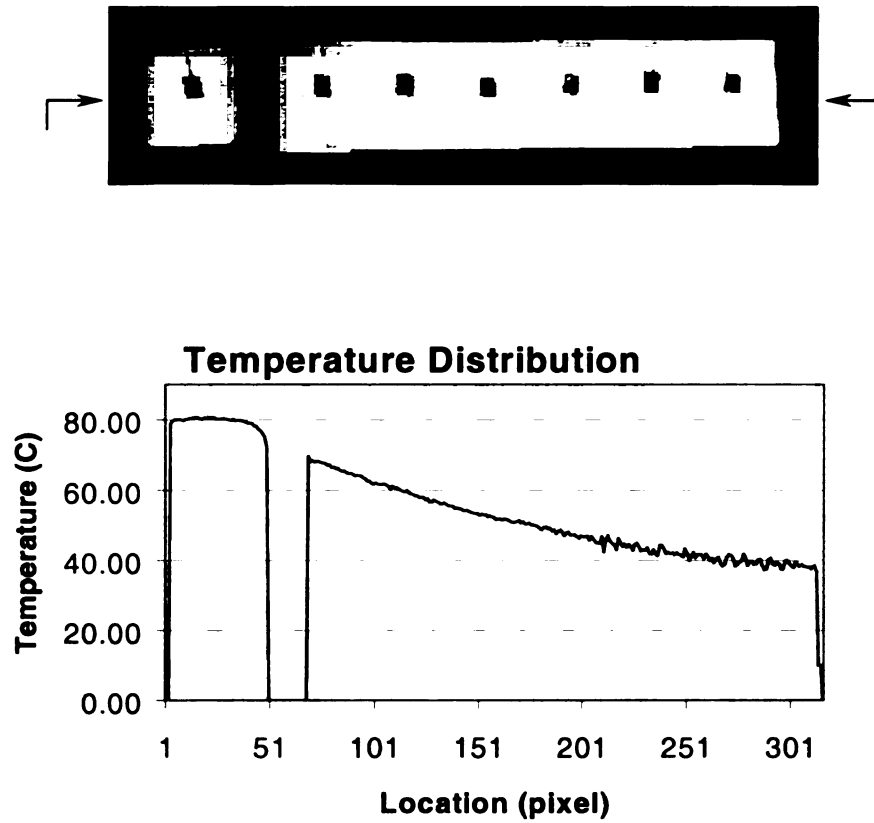


Figure 45. Temperature Distribution along Aluminum Fin - $T_{base} = 80^{\circ}\text{C}$.

Temperatures measured by thermocouples and FERIT at the six thermocouple locations are compared in Figure 46 for seven different base temperatures (from room temperature to 80°C at 10°C intervals).

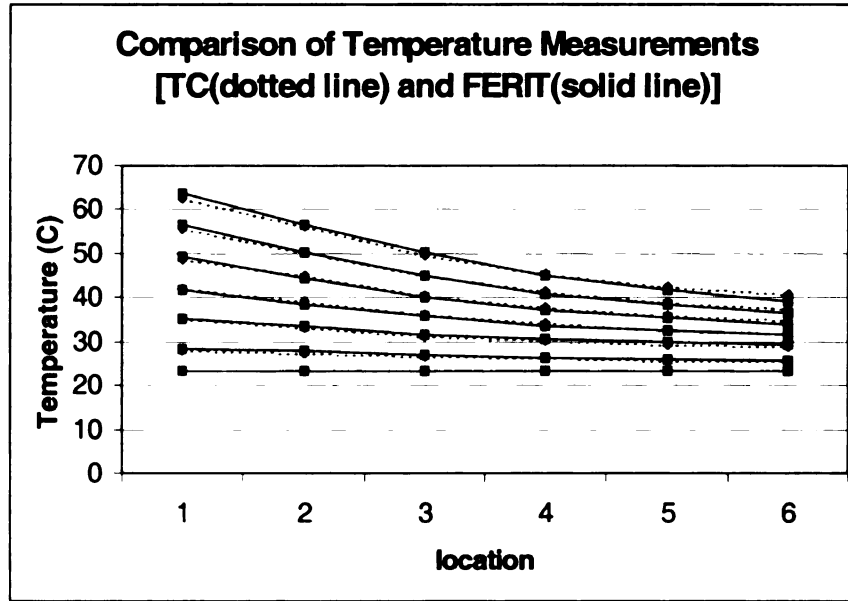


Figure 46. Comparison of TC and FERIT Measurements.

Each line denotes the temperature distributions measured by the six thermocouples (red: TC) or by FERIT at the corresponding locations (blue: FERIT). Location 1 corresponds to location closest (~20mm) to the heating source (base) and location 6 is the farthest point away from the base (~120mm). The temperature differences between these two methods for different temperature ranges are summarized in Table . The average difference between calibrated thermocouple readings and FERIT is about 0.45°C, which is consistent with the results given by the error estimation in the previous chapter. The differences at higher temperatures are slightly higher which might be attributed to the fact that the fin effect is more significant due to the larger temperature gradient between the surface and the ambient.

Table 3 . Temperature Measurement Difference at Different Temperature Ranges.

Range (°C)	Difference
20~30	0.38
30~40	0.44
40~50	0.45
50~70	0.51

5.2 Temperature Distribution of Micro-Structure by Joule Heating

To demonstrate the higher spatial resolution capability of the fluorescent technique over the infrared method and the possibility to obtain quantitative temperature data at the microscopic scale, the temperature distribution induced by joule heating of a microscopic device was measured using the fluorescent method. The heating elements are formed by an Indium Tin Oxide (ITO) film/microstructure deposited on the surface of a microscope slide. Their dimensions are shown in Figure 47. Electric current was carried by the thin gold strips (dark areas) to the ITO structures (light, rectangular areas). This induced localized heating. The electrical resistances for the two smaller ITO structures were 95Ω and 102Ω respectively. Even though there was a voltage drop across the gold film (approximately 3% of total voltage) due to its length, heating in the gold film was negligible compared to that in the ITO structures. Only the two smaller ITO structures ($20.8\mu\text{m} \times 24.6\mu\text{m}$) on the left and right of the larger one ($102.3\mu\text{m} \times 102.3\mu\text{m}$) were energized. The center to center distance of these two ITO structures is approximately 180

μm . The gap distances between the left and right smaller ITO structures and the larger one in the center are $45.5\mu\text{m}$ and $18.9\mu\text{m}$, respectively. The above measurements were calibrated using a 1.00mm micrometer on a microscope slide.

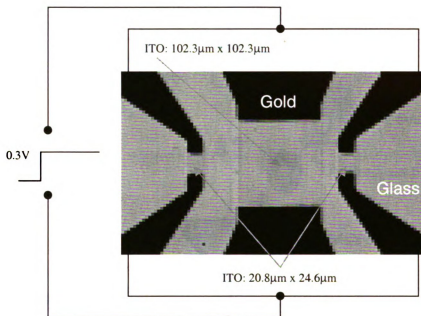


Figure 47. UCB Microstructure (Courtesy of Prof. A. Majumdar of UC Berkeley).

The test was conducted on a Nikon inverted microscope (Diaphot) as illustrated in Figure 48. The UV excitation was realized by passing the output from the Opti-Quip system through the UV filter, it was reflected by the dichroic mirror and reached the sample surface after passing through the microscope objective. The fluorescent emission was collected by the microscope objective and passed through the dichroic mirror, and was then directed to the red filter and ORBIS camera by the reflector. An imaging sequence was started right before the power was connected to the ITO structures. The exposure time used was 0.8s and the frame rate was 1.8s . The acquired intensity images were

converted to time-dependent temperature distributions with the temperature rendering functions of the FERIT software.

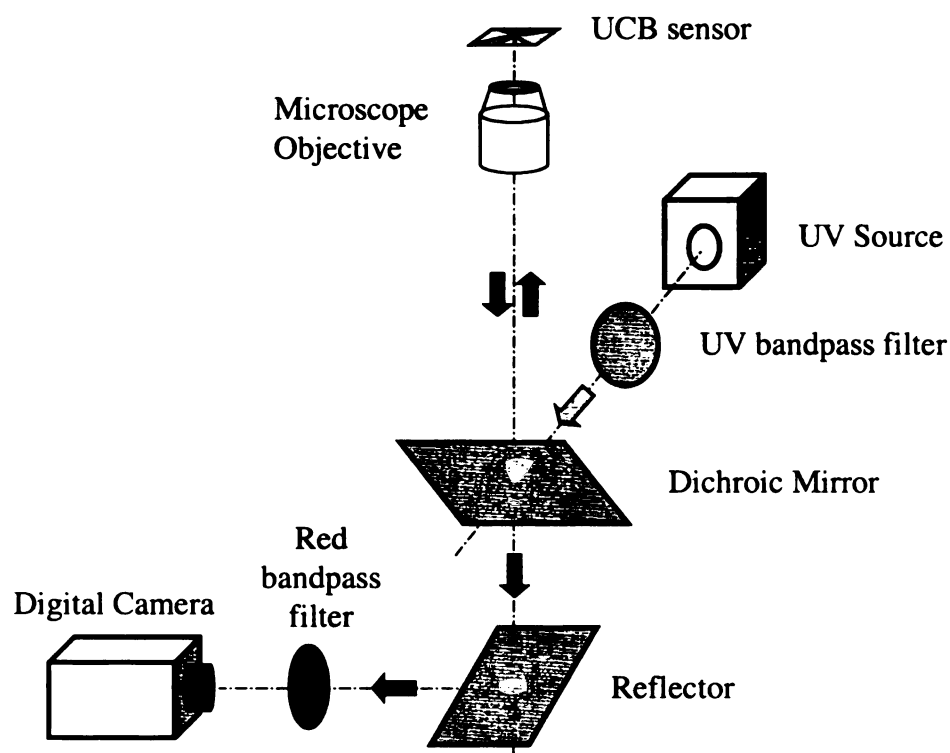


Figure 48. Schematic of Microscopic Heating Study of UCB microstructure on a Nikon Inverted Microscope.

Figure 49 shows the fluorescent emission intensity distribution of the microstructure at the reference (room) temperature. The intensity difference between the left and right portion of the image was entirely due to the non-uniform illumination by the UV. Since gold has a very high reflectivity at 620nm ($\sim 90\%$), areas with the gold leads had much higher (~ 1300 DU) intensity than areas of ITO and glass materials (700 DU). This suggested that the reflected signal constituted an important portion of the total signal. The

ratiometric approach will eliminate this optical effect, as shown in the following FERIT temperature measurement results.

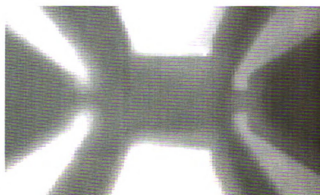


Figure 49. Fluorescent Intensity Distribution of Microstructure at Uniform Room Temperature (Image File: REF.TIF).

The temperature distributions measured by FERIT for the corresponding area (Figure 47) at $t=1.8s$, $12.6s$ and $27.0s$ are shown in Figure 50 to Figure 52. The temperature elevations near the two heating elements are obvious and relatively confined to the heating regions. Thermal diffusion in the neighborhood of these two rectangular heating elements became visible after ten seconds.

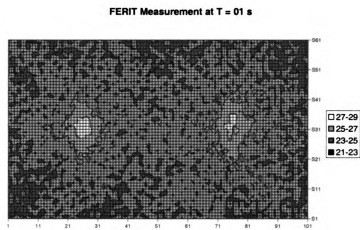


Figure 50. Temperature Distribution of ITO Microstructure Measured by FERIT at $t=1.0s$.

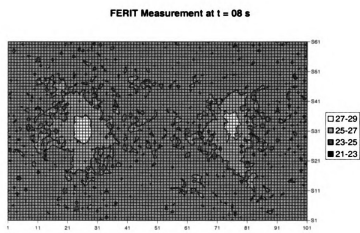


Figure 51. Temperature Distribution of ITO Microstructure Measured by FERIT at $t=8.0s$.

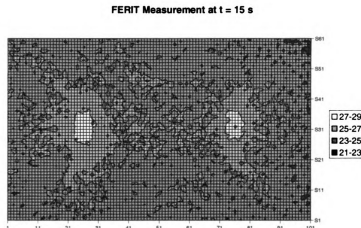


Figure 52. Temperature Distribution of ITO Microstructure Measured by FERIT at t=15.0s.

To verify the experimental results obtained by the FERIT method, a finite element simulation was conducted to derive numerical results for this test. The joule heating was modeled as constant heat flux boundary condition at the glass substrate. The result suggested that the temperature at the center of the ITO structure increases to about 6.7°C above ambient temperature after one second and increases very slowly thereafter, which was comparable to the results of the FERIT measurements.

The finite element model was constructed for a volume of 2.00mm x 2.00mm x 1.08mm in which the last dimension was the glass slide thickness, with the two heating elements located in the center on one of the surfaces (the 2.00mm x 2.00mm surface) of the block. The lateral dimension was chosen to be as small as possible but large enough so that the heat flux and temperature elevation was negligible at the boundary. This allows more finer elements to be concentrated in the heating regions. Element size increases gradually when moving away from the sources as shown in Figure 53, with the view vector

(pointing to the observer) set to (1, 1, 1). A total of 10,487 elements were used which is close to the maximum number allowed by ANSYS. A ten-node tetrahedral element type was used and the dimension of the heating elements was about four times the element size.

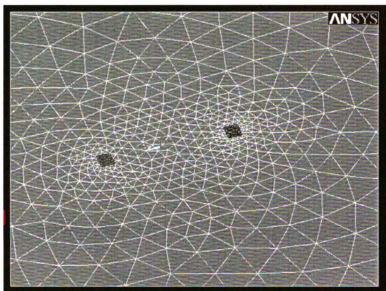


Figure 53. Finite Element Model for ITO Structures.

The ITO structure joule heating effect was represented as a surface heat flux. The heat flux was calculated by dividing the power input by the area of the two heating structures which are $704,000 \text{ W/m}^2$ and $670,000 \text{ W/m}^2$ respectively. Since they are much higher than the natural heat transfer coefficient ($\sim 5 \text{ W/m}^2$) and the time scale for the experiment ($\sim 20\text{s}$) is relative small, natural convection was neglected.

The predicted temperature profiles along the centerline of the two ITO structures at $t = 1\text{s}$, 8s and 15s are plotted in Figure 54, Figure 55 and Figure 56, along with those

measure

state af

measured by the FERIT method. The temperature distribution reaches a quasi-steady state after about one second (temperature increasing slightly after that).

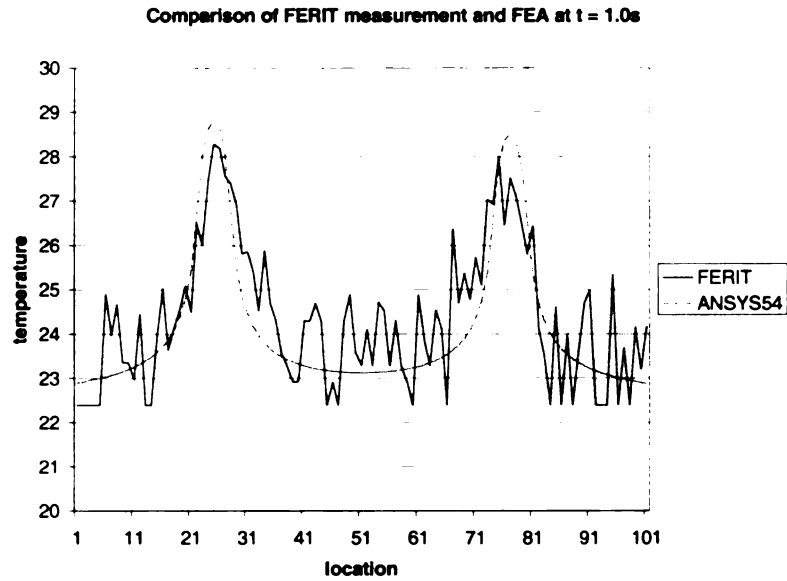


Figure 54. Comparison of Temperature Distribution - FERIT and ANSYS54 at t=1.0s.

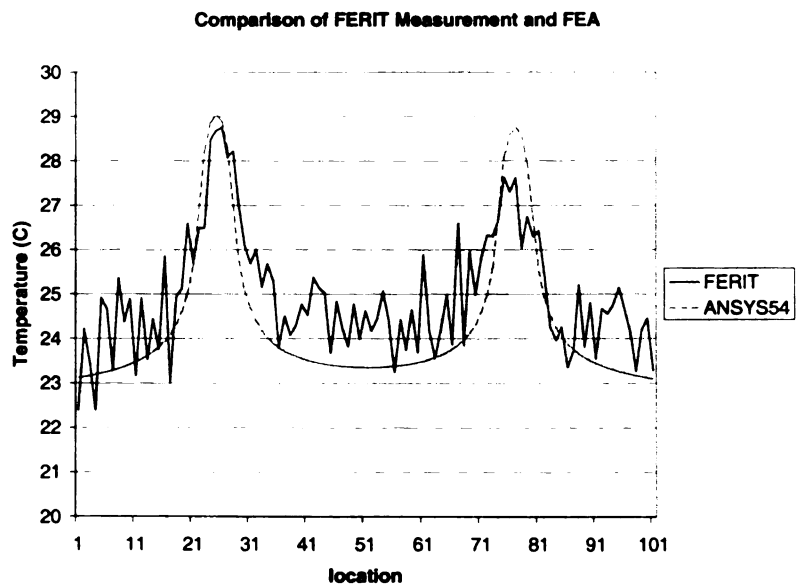


Figure 55. Comparison of Temperature Distribution - FERIT and ANSYS54 at t=8.0s.

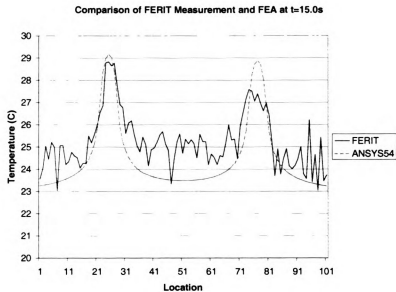


Figure 56. Comparison of Temperature Distribution - FERIT and ANSYS54 at t=15.0s.

The two dimensional temperature distribution at the surface predicted by the finite element analysis for t=15.0s is illustrated in Figure 57.

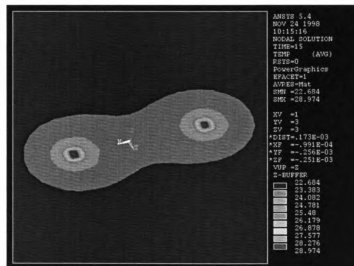


Figure 57. Surface Temperature Distribution at t=15.0s (Simulation - ANSYS54).

An infrared camera was also applied to measure the temperature distribution of the UCB microstructure under the same testing conditions.

Since there were three components on the ITO structure which have quite different emissivities: glass, ITO film and gold, a methodology described below was used to derive temperature distribution information after compensating for the spatial non-homogeneity of the emissivities .

The parameters of the Inframetrics 600 IR camera was set as follows: center temperature = 22.0C, room temperature = 22.0C, temperature span = 10.0C, emissivity = 1.0, frame averaging = 4. The IR camera was focused to infinity by adjusting the far-near control, then the zoom lens was added and the focus was adjusted to infinity again by adjusting the focusing ring on the zoom lens. Then the close-up lens was attached. The UCB device was moved back and forth along the optical axis of the IR lens to achieve optimal focus. An image was taken at room temperature, the apparent temperature was calculated and the emissivity map was derived by the following equation:

$$\varepsilon(i, j) = \left(\frac{T_{\text{apparent}}(i, j)}{T_{\text{ambient}}(i, j)} \right)^4 \quad \text{Equ. [16]}$$

The subsequent temperature distribution after the heating started was obtained by:

$$T(i, j) = T_{\text{apparent}}(i, j) / \varepsilon^{1/4} \quad \text{Eqn. [17]}$$

The emissivity map for the area corresponding to FERIT measurements (0.361mm x 0.216mm) are illustrated in Figure 58. Note that the scale of this figure matches (approximately) those of figure 47-52.

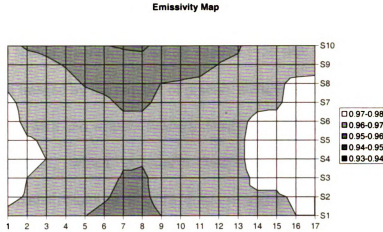


Figure 58. Emissivity Map of ITO Structure.

The emissivity is lower for the region with the gold coating (0.94) and higher for glass (0.98). Considering that pure gold has very low emissivity ($\varepsilon=0.18$ at 589nm, $\varepsilon=0.03$ at 2000nm) [Siegel, Howell,1992], the high value (0.94) in the gold coating region suggested that the polymer film (PMMA) containing the fluorescent probe for FERIT contributed significantly to the apparent emissivity.

The temperature measurement results using IR (again at the same scale as those in Figure 47-52) are shown in Figure 59. It is obvious that the IR results are very noisy even with four frame averaging and that the two individual heating spots are not resolved.

The highest temperature elevation within the region measured is just 0.75°C above ambient temperature, which is significantly lower than the predicted value ($\sim 6.7^{\circ}\text{C}$) and that measured by the FERIT method. Since the size of the ITO structure is already smaller than the spatial resolution of the IR camera ($\sim 50\text{ }\mu\text{m}$: calculated by dividing the actual dimension imaged by the number of pixels), the temperature reading is actually the average of regions with and without heating. Another factor is the slit response effect of the infrared method, which introduces temperature measurement errors while approaching its spatial resolution limit for a heated surface [Hoke, 1998]. Hoke showed that the slit response effect started to become significant at approximately 0.3mm . These results show the expected behavior. Specifically, the two heating structures separated by a distance of $180\mu\text{m}$ were not expected to be well resolved by the infrared imaging method when we knew that spatial resolution was problematic for objects separated by as much as $300\mu\text{m}$.

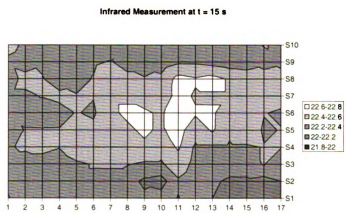
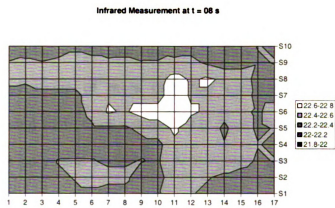
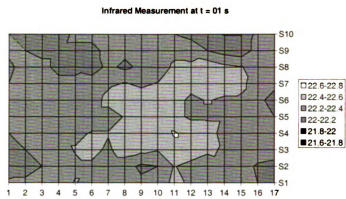


Figure 59. Temperature Distributions Measured by Infrared Method.

The infrared method failed to resolve the two heating elements and measured temperature incorrectly. A more elaborate emissivity mapping method and data processing model will not change this conclusion since the heating elements have the highest emissivity values.

5.3 Non-Destructive Evaluation

There has been increasing usage of composite materials in both aerospace and automotive industries due to potential weight and cost saving. However, composite manufacturing usually involves processing of more than one material component and multiple procedures / processing steps. Such complexity is more likely to introduce defects into finished parts. Take polymeric composites produced by liquid molding method as an example. Air bubbles and poor wetting of fibers by the matrix impose constant challenges to the product quality. Figure 60 shows the surface of a Reaction-Injection-Molded (RIM) Polyurethane/Glass composite with the above two types of defects, which are readily visible through the translucent matrix material (polyurethane).

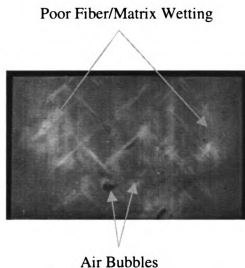


Figure 60. Product Defects of Reaction-Injection-Molded Composites.

In recent years, the thermographic (thermal wave) method has become a technology competing with the traditional ultrasound method for the non-destructive evaluation of defects. At the time of application, a high-energy pulse is uniformly deposited onto one of the surfaces and the temporal temperature distribution on the energized surface or the opposite surface is monitored. Due to the high temperature gradient in the thickness direction, thermal energy is dissipated through diffusion/conduction into the composites body until a uniform temperature is obtained, this energy is eventually dissipated through natural convection into the ambient air. If a defect is present within the composite, it will block the thermal diffusion path and create a temperature gradient on the surface (hot or cold spot). The magnitude of the temperature gradient depends on the pulse energy, defect size, depth, and material properties.

The FERIT method was applied to conduct a non-destructive evaluation of the sample shown in Figure 60. The sample is 2.3" x 1.4" x 1/8" in dimension, and one side was

painted black and the other was coated with the temperature sensitive fluorescent film. The sample was energized by a 1 kW Halogen lamp for 3 seconds and the temperature distribution was measured by the FERIT system on the opposite side. With such a setup, the location of a defect will have a lower temperature than its surroundings and will appear as a cold spot.

The temperature distribution of the composite surface before the pulse started ($t = 0.0s$) is shown in Figure 61. It is obvious that even though there was intensity non-uniformity due to surface condition (reflection) or UV non-uniformity, the FERIT's ratiometric processing eliminated these optical effects and provided uniform temperature readings (room temperature).

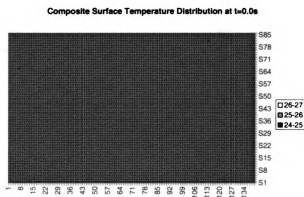


Figure 61. Composite Surface Temperature Distribution at $t = 0.0s$.

The temperature distributions measured by FERIT at $t = 21.0s$ and $t = 45.5s$ are shown in Figure 62 and Figure 63, respectively.

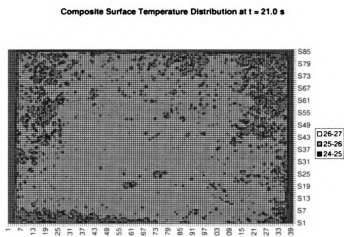


Figure 62. Composites Surface Temperature Distribution at $t = 21$ s.

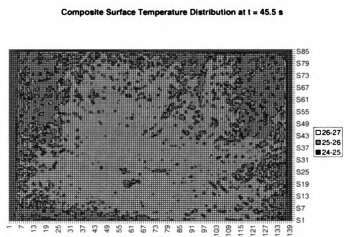


Figure 63. Composites Surface Temperature Distribution at $t = 45.5$ s.

The temperature gradient locations defined by the thermal wave method are consistent with visual determination of the locations of the air bubbles and poor wettings. At $t = 45$ s, the effects of lateral diffusion and ambient cooling start to set in.

This preliminary study demonstrated that the FERIT method could also be used for non-destructive evaluation of composites, even though it might not be as convenient as the infrared method since two coatings are needed for the FERIT method.

Tests were also conducted for plastic material (Acrylic) with simulated defects (cylindrical holes) to test the idea of conducting thermal wave experiment in reflective mode (energizing and detection on the same surface) since this is a prefer method for thermal wave method. A layer of black paint (for absorbing pulse energy) was applied to the sample surface first and followed by the deposition of a layer of fluorescent paint on top of black paint. The signal strength was very weak due to the strong absorption of the black paint to the fluorescent signal, the solvent for fabricating the fluorescent film was also observed to dissolve the dried black paint. With similar energizing power level, temperature distribution measured by FERIT on the surface was found to be very noisy and fluctuating from point to point dramatically ($>1\text{ }^{\circ}\text{C}$), which overwhelmed the temperature gradient created by the defects ($0.5\text{ }^{\circ}\text{C}$, estimated by numerical simulation). Low signal level and possible interaction between solvent/probe/black-paint may be the possible causes.

Chapter 6

Recommendations

6.1 System Considerations

6.1.1 Camera

Being the heart and soul of an imaging system, the camera is the most important component that will ultimately determine the performance characteristics of the system, such as dynamics, sensitivity, resolution, and noise.

A CCD (Charge-Coupled-Device) remains the primary choice as the sensing device, although other devices based on different operating principles are also available, such as CID, and CMOS sensors.

CCD imaging sensors can generally be classified into two categories: full frame and frame transfer devices.

The operation of a full frame device requires a mechanical shutter to control the start and stop of an exposure. There is a line of readout registers the same size as the number of

columns in the CCD and charges at each row of the CCD can be parallel-shifted to these registers and eventually be sequentially shifted to the output amplifier and digitized. The digitization is complete when the last row (farthest from the readout registers) is read out. An imaging cycle typically consists of the following steps (Figure 64):

- Clear the CCD
- Open shutter to start exposure
- Integrate for desired period of time
- Close shutter to end exposure
- Start loop for the number of rows:

Clear readout registers

Parallel shift one row of charges to readout registers

Sequentially shift the readout registers to the readout amplifier and digitize

- End

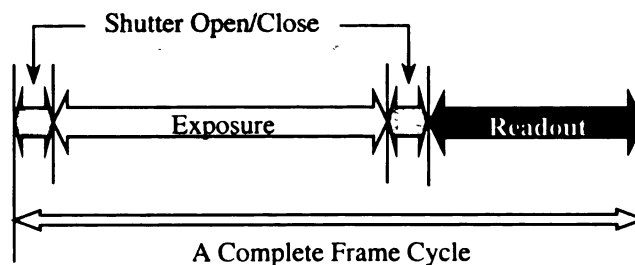


Figure 64. Frame Cycle of Full Frame Device.

This limits the frame rate of a full frame device to about 1s. Due to its relatively simple architecture, the cost of such system is low (a few thousand dollars) and it has become

very popular amount amateurs for astronomical observation. High end systems are also available which feature a cooling option to reduce the dark current (which is useful for faint signals that require long exposure times), scientific grade CCD, large CCD format and high resolution digitizer. The price for full frame systems can vary from \$5,000 to \$30,000. CCD sensitivity (back-illuminated or not), format (pixel count), grade (defect count), cooling option are the most important determining factors.

Contrary to the full frame device, the frame transfer device operates a bit differently since it has a buffer the same size as the sensing array to temporarily store the charges:

- Clear CCD
- Integrate for desired period of time
- Transfer charges to buffer
- Start loop for the number of rows:
 - Clear readout registers
 - Parallel shift one row of charges to readout registers
 - Sequentially shift the readout registers to the readout amplifier and digitize
- End

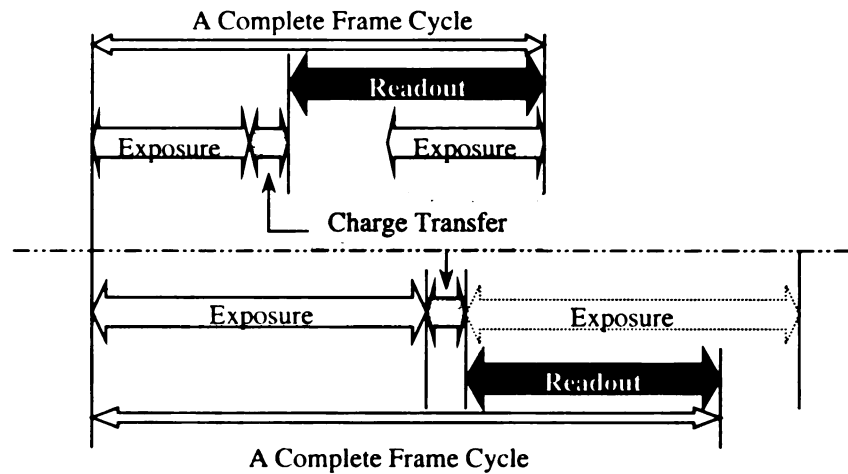


Figure 65. Frame Cycle of Frame Transfer Device.

This procedure not only eliminates the necessity for a mechanical shutter and the time overhead caused by the movement of the shutter blade (~5ms), it also allows charge transfer and digitizing to be performed simultaneously with exposure. If the digitization time is shorter than the exposure time, the dynamic capability of such a device is only determined by the exposure time itself. The above operations are illustrated in Figure 65. Such devices (especially those with back-illumination option of high QE) were limited to military use in the early and mid 90s. Civilian applications and scientific research with these CCDs are just getting started. Frame transfer systems still remain quite expensive and they usually cost \$20,000 ~\$50,000. The contributing costs are CCD sensitivity (back-illumination), format (pixel count) and grade (defect count).

In contrast to high volume production of CCD systems for surveillance and home entertainment, most CCD systems for scientific and quantitative imaging applications are custom-built in small batches to fit individual needs. Available options include imager

format/resolution, cooling option, full frame or frame transfer, intensifier options, digitizing resolution.

For most fluorescent imaging applications, the signal strength is relatively low. This is particularly true for microscopic specimen. The exposure time required is usually around one second for the sensor to get close to saturation. Full frame systems are attractive since they cost less and they are suitable for applications that will tolerate frame rates greater than 1 fps (frame per second). Sub-area imaging or a line-scan mode might not help much since the most dominant part of the total time is the exposure time. A frame transfer device works best for situations with high signal strength and high frame rate. Its advantage over a full frame device is not very significant for faint signals such as fluorescent emission since exposure time is much longer than data transfer time.

The cooling option is usually recommended, since it will not only reduce the dark current that could degrade the dynamic range, but it will also keep the CCD at a stable temperature so that consistent readings can be obtained. Usually cooling below -10°C ~ -20°C will be sufficient.

Since the noise or uncertainty of the detector is usually worse than 0.1%, selecting a system with 10 to 12 bit resolution would be enough for most situations (0.1% and 0.025% error, respectively). The 0.1% uncertainty is determined by the fact that most CCD sensors have a full well of electrons less than 10^6 , in which case the shot noise is $1/\sqrt{N} = 0.1\%$.

As to the CCD format (pixel count), a small or intermediate format is recommended (256x256 ~ 1K x 1K), since a larger format is much more expensive and it will also take a longer time to digitize the frame.

The following table is a partial list of CCD camera manufacturers and their product lines. The supported CCDs are also listed. Price ranges instead of prices for specific configuration (CCD, cooling, resolution) are given due to the many possible combinations. The low end price usually is for a small format, full frame device with low resolution and low frame rate options, while the high end price tends to be for a large format, frame transfer device with high resolution and high frame rate options. The cost of a system of intermediate capabilities can be interpolated based on options.

Table 4. Digital Camera Manufacturers.

Manufacturer	Model	CCD	Cooling	Resolution	Price
SpectraSource Instruments	ORBIS, Teleris	FF: Kodak, SITE, FT: TI, EEV	Yes	12, 16	Teleris: \$4,000~\$10,000 ORBIS: \$8,000~\$25,000
Princeton Instrument	PentaMax, ICCD series,	FF: Kodak, PI, SITE FT: EEV	Yes	8, 12, 16	\$35,000~\$60,000
Hamamatsu		FF: SITE FT: SONY	Yes	10, 12	\$33,000~\$50,000
Cooke	SensiCam	FT: SONY Intensifier Option	Yes	12	\$17,000~\$50,000
PixelVision		FF: SITE, FT: EEV, TMD	Yes	12, 16	\$27,000~\$50,000

The specifications of the ORBIS 1 system used in this study are listed as follows:

CCD

- Model: SI-502AB (back-illuminated) Scientific-Grade

- Manufacturer: Scientific Imaging Technologies, Inc.
- Format: 512 x 512
- Pixel Size: 24 μm x 24 μm
- Array Size: 12.3 mm x 12.3 mm
- Optical Full Factor: 100%
- Quantum Efficiency: 82% at 450nm, 86% at 550nm, 88% at 650nm
- Charge Transfer Efficiency: 0.99999 (at 50KHz Digitizing Rate)
- Full Well Capacity: 350,000 e/pixel
- Read Out Noise: 7 e at -90°C
- Dark Current: 12.75 e/pixel/sec at -30°C

Camera Head

- Resolution: 12 and 16 bit A/D Converter
- Wide Dynamic Range: 94 dB (16bit, 50 kHz), 81 dB (12 bit, 1 MHz)
- CCD Temperature: -20°C (Two Stage TEC) $\pm 0.1^{\circ}\text{C}$
- Exposure Time: 0.01 second to hours
- Interface: PCI bus

Software

- Camera Control: Exposure, Subframe, Sequence, Multiple Frame
Average
- Display Analysis: Gray Scale and False Color, Line Profile,

Photometric Measurements

- Image Processing: Flat/Bias/Dark Field Compensation
Basic Frame Arithmetic
- File Formats: FITS

6.1.2 UV Source

A stable UV source is highly recommended since a highly stable UV lamp (~\$4,000) is not that much more expensive than a poor one (\$100~\$2,000), and it is not a major part of the investment for the overall system. Although flicker noise of an unstable UV source can be monitored and compensated, the complexity and cost introduced by extra electronic hardware needed to accomplish that might cost more than the saving on the UV lamp. Utilizing an UV source with less than 0.1% noise does make test and data processing easier since the flicker noise can be neglected.

6.1.3 Photodiode

Even with a highly stable UV source, its output will also drift one or two percent over a period of several hours. For example, to obtain a calibration relation, the fluorescent film will be set to different temperatures for its emission intensities to be measured. Such an experiment can take as long as five hours depending on the number of set points. In such a case, a photodiode sensitive to UV should be employed to monitor the UV intensity

change so that the fluorescent intensities can be compensated. The OPT301M photodiode from Burr-Brown has a silicon sensor and preamplifier integrated and is very convenient to use. The wiring diagram and conversion formula are listed in Appendix B.

6.1.4 Total System Cost

FERIT system component and total cost can be summarized as follows:

• Camera:	ORBIS TE-Cooled 12/16 bit digital (SI502AB)	\$13,800
• UV Source:	Opti-Quip™ 770U lamp and 1600 power supply	\$4,500
• Computer:	Dell Dimension™ with 300 Mhz Intel Pentium II™	\$2,500
• DAQ:	ComputerBoards™ DAS802/16 and CIO-EXP16	\$700
• PhotoDiode:	BurrBrown™ OPT301M	\$30
• UV/red filters:	Omega Optical™ interference filters	\$500
<hr/>		
Total:		\$22,030

The cost of the system is comparable to that of the liquid crystal method, but is approximately half the cost of the infrared equipment (>\$50,000).

6.2 The Influence of Film, Surface Dimension, and UV Intensity

6.2.1 Fluorescent Films

The low signal strength is always an important factor that limits the dynamic system response since the CCD has to be integrated long enough to obtain sufficient enough light. One solution would be to manipulate the film parameters to maximize its output. This can usually be accomplished in two ways: (1) Increase the probe concentration; (2) Increase the film thickness. The concentration used in our study is already very high (25wt%) and there is not too much room to increase it. The second approach will work but it has some adverse effect on the surface temperature distribution and the dynamic response of the surface being measured. If the film is too thick, first of all, it has the potential to alter the surface temperature distribution since it introduces one more conduction path across the surface. Secondly, since a polymer film is a poor thermal conductor, its thermal resistance might be significant in the thickness direction, especially when convection is important. In addition, it might also affect the dynamic response of the surface due to the finite thermal mass of the film. The following table illustrates the response time scale for different film thickness (Acrylic):

Table 5. Dynamic Response as a Function of Film Thickness.

$t \sim L^2/\alpha$, $\alpha=\kappa/\rho C_p$; $\alpha \approx 1.0e-7$ for Acrylic					
L (micron)	1000.0	100.0	10.0	1.0	0.1
t (s)	10.0	0.10	0.001	1.0e-5	1.0e-7

As one can expect, the thicker the film, the slower the response one will get. The films we made are usually around 10 μm thick, the corresponding response time (1ms) is much less than the camera frame period (>0.2 s). The film thickness can be estimated by scratching the film with a sharp blade, and the notch formed can be analyzed under a microscope with an objective of very narrow depth of field. The corresponding thermal resistance (L/k) is about $5\text{e-}5$ $\text{m}^2\text{K/W}$, which is much smaller than that of natural convection $1/h = 0.2$ $\text{m}^2 \text{K} / \text{W}$.

6.2.2 Optical Consideration

For a given film thickness and UV excitation level, the optical and geometric characteristics also play important roles in determining the signal strength. The following calculations consider measurements made for both large (inches) and small (mm) dimensions.

From the following equation:

$$V_{\text{out}}(i, j) = [k \text{ QE}_{\text{ccd}}] * T_{\text{optical}} * \Omega * [1+R(\lambda)] * [I_{\text{uv}} D_{\text{probe}} A_{\text{element}} * \text{QE}_{\text{probe}}(T) \Delta t]$$

$$\sim \Omega * A_{\text{element}}$$

The following calculations provide some idea in a relative sense about how optics determines signal strength, assuming constant UV excitation intensity.

Parameters:

CCD: Pixel Size: 24 x 24 microns, format: 512 x 512

Optical Lens: Diameter $D_1 = 10.0$ mm, focal length $f = 25.0$ mm

Microscope Objective: Magnification=10X, working distance=5mm, diameter $D_2 = 5$ mm

Case 1: Optical Lens

Object distance $L = 0.5$ m, $A_{\text{element}} = (512 * 24 * L / f)^2 = 0.0604 \text{ m}^2$

$$\Omega = \pi (D_1/2)^2 / L^2 = 0.000314$$

$V_{\text{out}} = 1.9 \text{ e-}5$ (surface dimensions: 0.245m x 0.245m)

Case 1: Microscope Objective

Object distance $L = 5$ mm, $A_{\text{element}} = (512 * 24 / M)^2 = 1.5 \text{ e-}6 \text{ m}^2$

$$\Omega = \pi (D_2/2)^2 / L^2 = 0.785$$

$V_{\text{out}} = 1.2 \text{ e-}6$ (surface dimension: 1.22mm x 1.22 mm)

The above calculations show that for the same fluorescent film and UV excitation level, a decrease in surface dimension by 20-fold will result in a decrease of the signal strength by one order of magnitude. That is why microscopic fluorescent imaging usually requires a fairly long exposure time (> 1 s).

6.2.3 UV Intensity

One other option to enhance the fluorescent signal output is to increase the UV excitation level. Experimental study has shown that very good linearity is obtained for the excitation level tested ($< 5 \text{ W/m}^2$). Applying very high UV excitation has two implications: (1) the response might move towards saturation; (2) surface heating effect becomes significant. Keeping the UV excitation level below 1 W/m^2 is recommended.

Chapter 7

Future Work

7.1 Application Extensions

The fluorescent imaging method can be applied to other applications in heat transfer analysis that require surface temperature measurements, for example, surface convective heat transfer coefficient mapping, wind tunnel experiments, electronic packaging and cooling analyses. Brief comments about the above applications using FERIT in comparison to other techniques (infrared, liquid crystal) are provided in the following paragraphs.

To use FERIT to measure convective heat transfer coefficient, one influencing factor could be the ambient light, which can reduce the system dynamic range since the ambient background could be a major part of the total signal. This problem can be resolved partly by using opaque screens to block out the ambient light. Since an airbrush can be used to fabricate the fluorescent film, it is more advantageous than the liquid crystal method, which has problems to cover large or curved surfaces.

For wind tunnel applications, FERIT can be adapted readily to conduct temperature measurement. Since the emission is in the UV-visible region, the only requirement is that an optically transparent window is available so that UV can be directed to the area of interest and that the red emission can be captured. Quartz glass is a good candidate as a material for such windows since it has high transmittance for both wavelengths. Fluorescent paint can be spray-painted onto the inner surface of the wind tunnel. FERIT has obvious advantages over infrared methods in these applications since FERIT employs a ratiometric approach, which is not very sensitive to the properties of most window materials, while using infrared the window absorption has to be compensated. In addition, infrared transmitting optics and windows are very expensive.

It is very likely that it is in the area of electronic cooling that FERIT will demonstrate its advantages regarding many aspects of thermographic methods. For board level applications, both infrared and liquid crystal have difficulties in one way or the other. For the infrared method, the wide range of emissivity values of electronic components will give false information about the temperature; i.e., metallic leads usually have very low emissivity and the temperature will appear low. However, other packaging materials such as plastics have fairly high emissivity and their temperature reading will be more realistic. Applying a layer of black paint might solve the emissivity problem. Nevertheless, the black paint has to be relatively thick ($\sim 50\text{ }\mu\text{m}$) so that the surface will be fully covered. This would inevitably alter the surface thermal resistance and dynamic response. Another drawback for the infrared method is its limited spatial resolution, it becomes problematic when a structure is smaller than $300\mu\text{m}$ [Hoke, 1998], which makes

it inapplicable to the microstructures of many modern electronic devices. Even though the liquid crystals are also available as spray paint, the temperature response uniformity and calibration accuracy is not as good as the regular flat sheet product.

In contrast, fluorescent films can be fabricated either by spray painting or spin-coating. They can be made as thin as the sub-micron level so that they can be used to discern very small structures. As the semiconductor industry is pushing toward smaller device and high switching frequency/power consumption, FERIT will become an economic and practical choice for thermal management and heat transfer analysis of such devices. The precaution for the FERIT method is to make sure the solvent will not interact with the components of the circuit board.

7.2 Fluorescent Probes for Low and High Temperature Applications

The FERIT system developed can be transferred readily to other temperature probe systems that have different operating ranges. However, there are more complications for both high and low temperature applications.

If the application temperature is higher than the melting temperature of the polymer base, other carrying media needed to be considered to replace the polymer since it has a relatively low melting temperature (PMMA: $\sim 200^{\circ}\text{C}$).

For low temperature application, fogging and frosting could be a problem at the time of calibration and application since fogging and frosting would tend to develop over time and would scatter the excitation and emission signals.

7.3 Further Study in Microscopic Scale

For heat transfer at the microscopic level, there is one more complexity associated with the calibration relation, for film application on metallic surfaces. The metallic surface will act as a mirror and create an image dipole for each excited fluorescent molecule. The interaction between the original dipole and its mirror image will change its lifetime in the excited state, which eventually affects the relaxation behavior of the excited molecules. This effect is most significant for molecules near the metallic surface (within 1000 nm) [Chance, Prock, Silbey, 1978].

Systematic study is necessary for this particular case to yield more insights: metallic film materials and thickness, fluorescent film thickness and concentration, surface quality (oxidation, roughness, etc.). It is desirable to design experiments with the above parameters in a controlled manner and conduct calibration measurements for fluorescent emission intensity as a function of temperature. Such tests would require expertise and facilities in many areas, including surface chemistry, quantitative film characterization, optical measurement, and even chemical synthesis.

Since our study concentrates on the length scale from centimeter to micrometers, the fluorescent film is relatively thick for the above phenomena to become significant. No further efforts were devoted to a detailed investigation of this area. However, it remains an interesting and challenging work for applications in microscopic scale (< 1 micron).

Chapter 8

Conclusions

A fluorescent-based thermographic system has been successfully developed and evaluated. The system is capable of performing field temperature measurement of surfaces. The presented work identified, investigated and characterized several important aspects of a fluorescent emission imaging technique for surface temperature measurement. Starting from fundamental fluorescent emission and optical imaging theory, we proposed the temporal ratiometric approach which eliminates optical features caused by excitation and film thickness variation by ratioing the intensity at a point of interest with the intensity at a known reference temperature.

The system developed represents an integration of hardware and custom-built software to accomplish imaging, temperature rendering, data visualization and storage. The hardware consists of a cooled digital camera, highly stable UV source, UV monitoring photo-detector, 300Mhz personal computer, and data acquisition / temperature measurement and digital control boards. The approximately total cost of this system is \$22,000. The software includes two Windows-based application software programs for general-purpose data acquisition and temperature measurement, as well as FERIT.EXE, the custom-developed Windows-based application software which handles interactions with imaging hardware, creates an image display and performs temperature conversion. The custom-

built software utilized image control library functions and a more common file format (tiff) which allows more flexibility. This software also makes it possible to realize simultaneous UV excitation monitoring and digital control for other hardware.

Calibration relations for the temperature dependent fluorescent emission intensity have been obtained and integrated into the temperature rendering algorithm for efficient temperature conversion.

The system also demonstrated advantages over previous temperature probe systems in terms of photobleaching and resistance to moisture, which make it a robust choice for many application situations.

The measurement errors of the system were also identified and evaluated, including read noise, dark noise, shot noise, flicker noise, digitizing noise. Among these the shot noise was found to be the major contributing factor. Based on the estimate of these noise sources, the system noise was estimated to be approximately 0.4°C , which is about a factor of 2 better than that of system developed by another group [Liu, Campbell, and Sullivan, 1995].

Several applications of surface temperature measurement were design to illustrate the capabilities of the developed system, for both the large scale (inch) and the microscopic level (μm). The measurement results were compared with traditional methods

(thermocouples) and a numerical model. Good agreement was observed. Better spatial resolution was observed for FERIT compared to the infrared technique.

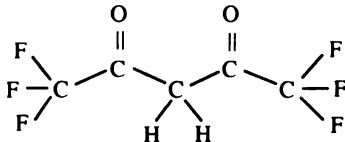
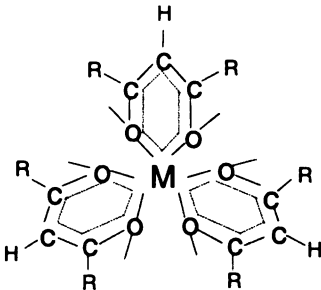
Recommendations for setting up such a system were also given based on the knowledge acquired through the development stage, in terms of costs, dynamic response, resolution, etc.

In Summary, the system developed is capable of provide quantitative surface temperature measurement at both large (inches) and small (mm) scales. The system has a temperature resolution of approximately 0.2°C (based on the reproducibility of intensity measurement of the CCD camera). The system has an accuracy of 0.4°C , which is comparable to its infrared and liquid crystal counterparts. The frame rate achieved is approximately 1 fps (with a full frame device) which can be further improved by using a frame transfer device (10 fps). The system has a temperature operating range of approximately 80°C . Compared with the infrared method, it has the advantage of higher spatial resolution (μm), easier data interpretation, and lower costs. Compared with the liquid crystal technique, the system has higher spatial resolution and wider operating range, easier data interpretation, and it is easier to apply to surfaces. Compared with the previous fluorescence-based systems, the developed system has better photo-bleaching behavior which greatly reduces the calibration difficulties and makes it applicable to both transient and steady state conditions. The introduction of UV monitoring improves the measurement accuracy, while the newly developed temperature rendering algorithm is more efficient and accurate than the traditional polynomial or exponential fit methods.

APPENDICES

APPENDIX A

Procedures for Synthesis of Temperature Sensitive Probe

Reactants	Product
1,1,1,5,5,5,- hexafluoroacetylacetone	Tris(1,1,1,5,5,5-hexafluoroacetylacetone) Europium (MW=773.11)
<div>C₅H₂F₆O₂</div> <div></div>	<div>R=CF₃ M=Europium</div> <div></div>
Molecular weight: 208.06	
Amount (gram): 1.000	
Europium(III) Chloride Hexahydrate	
Eu(III)Cl ₃ .6H ₂ O	
Molecular weight: 366.41	
Amount (gram): 0.587	
<div>Procedure:</div> <div><div>1. Dissolve the europium compound into 50ml of distilled water;</div><div>2. Increase the pH to 8.5 by adding ammonium hydroxide;</div><div>3. Stoichiometric amount of ligand (hfa) is added while stirring;</div><div>4. Allow solution to react overnight while stirring;</div><div>5. Filter the precipitate and dry for 24 hours at 70°C.</div></div>	

APPENDIX B

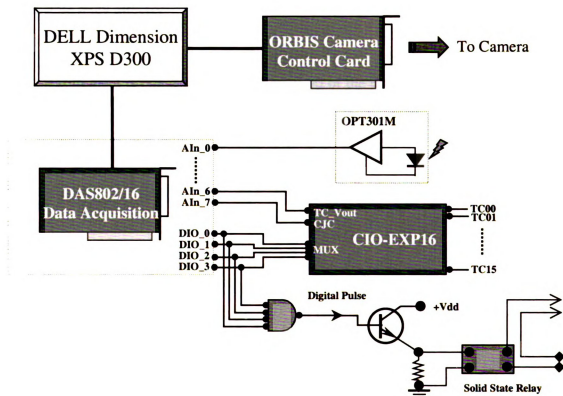
Fluorescent Film Fabrication

1. Weigh the paint bottle of the airbrush kit.
2. Re-zero balance and add the specified amount (0.15g) of PMMA to bottle
3. Re-zero balance and add the specified amount of Methyl-Ethyl-Ketone (MEK, 10g) to the bottle.
4. Seal the bottle opening with aluminum foil.
5. Place the bottle on top of heater/stirrer.
6. Set the heater at about 70°C (scale 1) and stir for about 20 minutes or until all the PMMA pellets dissolve in the solvent.
7. Shut off the heater and keep stirring for another 10 minute for the solution to cool back down to room temperature.
8. Add the specified amount (0.05g) of temperature probe Eu(hfa)_3 to the mixture and stir for another five minutes.
9. Connect the airbrush air inlet nozzle to regulated compressed air (If compressed nitrogen tank is used, close the fine adjust valve and open the main valve all the way; open the fine adjust valve slowly until desired air flow is obtained; close the main valve).
10. Place the cap cover of the bottle tightly and attach it to airbrush.
11. Open the main valve and test painting on a test surface, adjust flow if necessary.
12. During painting, shake the bottle slightly to maintain uniform paint distribution.

13. Adjust the paint flow control knob on the airbrush to obtain desired paint/air mixture.
14. Aim the airbrush to the surface at about 5 inches distance and move the airbrush in left/right steady motion.
15. Clean airbrush using MEK solvent.
16. If possible quench the finish surface at approximate 120°C for half an hour to allow solvent molecules from the deeper layer to escape.

APPENDIX C

System Electronics Wiring Diagram



The above electrical diagram summarize the connectivity of camera and data acquisition and temperature measurement boards, as well as peripheral electronic design for UV intensity measurement, digital control for external power sources (high power halogen lamp, heaters).

The default configuration for the temperature measurement utilizes CIO-DAS802/16 board's channel 06 for thermocouple output and channel 07 for cold junction compensation. The four digital lines are connected to an AND gate to provide digital controls (all highs: short, otherwise: open; for the solid state relay). The transistor acts as a current buffer for the digital port since their output isn't enough to drive the Greyhills solid-state relay directly.

UV measurement is connected to the channel 00 of the data acquisition board. The other input channels (01 to 05) are available for future use.

APPENDIX D

Photo-detector and wiring diagram

Burr-Brown Integrated Photodiode and Amplifier – Model OPT301M

Features:

- Photodiode size: 0.090 x 0.090 inch
- 1M Ω Feedback resistor
- High Responsivity: 0.47 A/W (at 650 nm)
- Improved UV response (0.15 A/W at 365 nm)
- Low dark errors: 2 mV
- Wide Supply Range: $\pm 2.25\text{V}$ to $\pm 18.0\text{V}$
- Bandwidth: 4 kHz
- Low quiescent current: 400nA
- Excellent linearity: 0.01%

Conversion from output Voltage U (in V) to Intensity I (in W/m²):

$$I = (U / 10^6 \Omega) / 0.15 \text{ A/W} / (0.002286\text{m})^2 = 1.2757 * U \text{ W/m}^2.$$

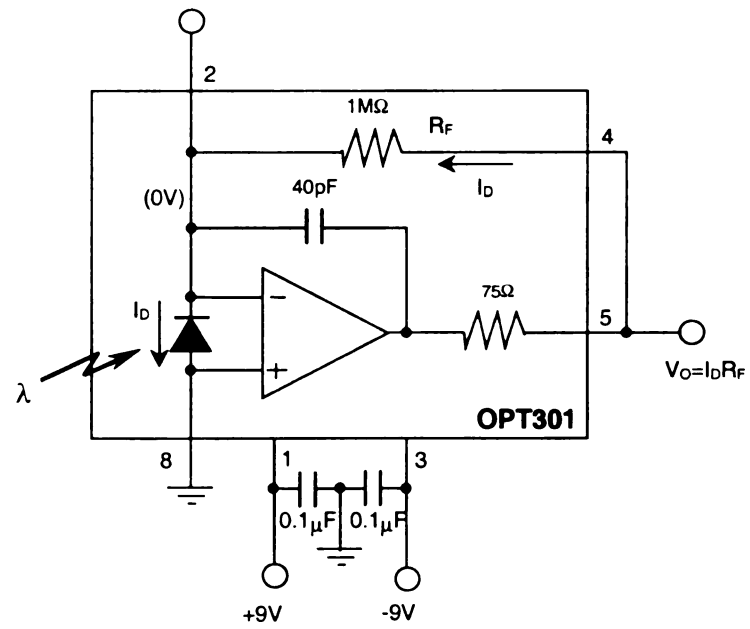


Figure 66. Wiring Diagram for OPT301M Integrated Photodiode and Amplifier.

APPENDIX E

Error of Mathematical Model

While using a polynomial to describe the fluorescent ~ temperature behavior (calibration), an error can be reduced by employing a polynomial of an appropriate degree. The following MATAB script gives an estimate of the possible error for different cases:

```
clear all;
temperature =
    [ 23.499431
      30.381219
      40.340126
      50.516041
      60.448514
      70.215188
      80.385338];

intensity =
    [ 2179.73
      2031.4607
      1727.6707
      1391.8878
      1032.6153
      718.93476
      454.10963];

N=7;
```

```

[P,S] = polyfit(temperature,intensity,N); /* get polynomial coefficients */
T = [23.5:0.1:80.5];

[out, delta] = polyval(P,T,S); /* interpolation results and error */

error1=max(abs(delta))

error2=(sum(abs(delta)))/length(T)

```

Table 6. Errors of Polynomial Fits.

Degree	1	2	3	4	5	6	7
Max_Error (DU)	43.61	52.67	8.62	10.71	16.10	N/A	0.32
Ave. Error (DU)	40.02	45.66	7.45	9.56	13.59	N/A	0.16
Max Error (°C)	1.44	1.74	0.28	0.35	0.53	N/A	0.01
Max Error (°C)	1.32	1.50	0.25	0.32	0.45	N/A	0.005

Remark: (1) $\text{Error}(C) = \text{Error}(\text{DU}) / \text{Slope_of_Calib_Curve} = \text{Error}(\text{DU}) / 30.34$.

(2) Polynomial of degree 6 caused singularity in error estimate parameters.

APPENDIX F

Excitation Filter and Adapter

The excitation filter was manufactured by Omega Optical (365HT25) which allows only the UV components near the central wavelength 365nm to pass through. The bandwidth is 25nm. The spectral transmittance is illustrated in the following figure:

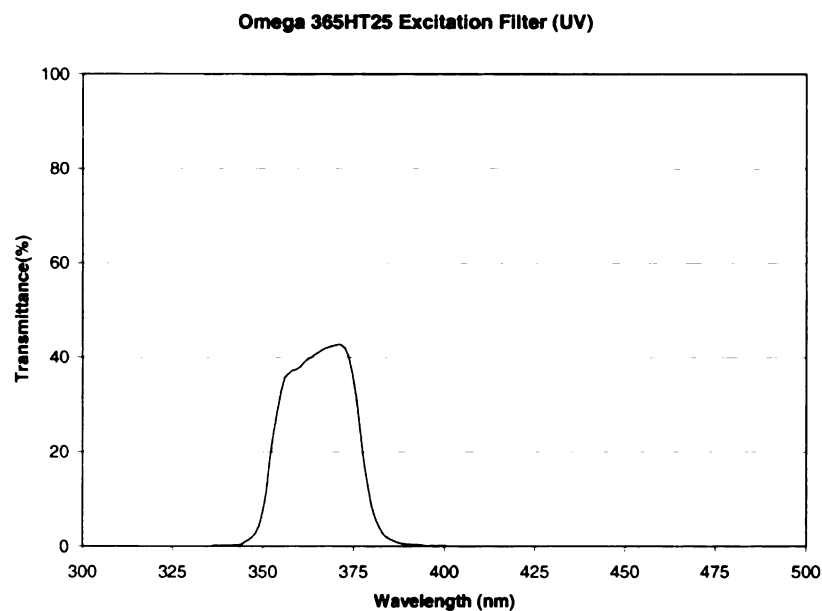


Figure 67. Spectral Transmittance of Excitation Filter (UV).

Since this UV source is used for both large scale and microscopic experiments, an adapter was designed to accommodate such requirements. One end of the adapter can be attached to Opti-Quip 770U lamp house and the other end matches the UV port on the

Nikon microscope. An “U” shaped plate in the adapter can be used to accommodate a 2”x 2” neutral density filter to obtain desired excitation level. In this study an O.D. = 0.2 neutral density filter was used.

APPENDIX G

Emission Filter and Adapter

The emission filter was manufactured by Omega Optical (620BP30) which allows only the red component near the central wavelength 620nm to pass through. The bandwidth is 30nm. This filter features very high transmittance at the central wavelength (~90%). The spectral transmittance is illustrated in the following figure:

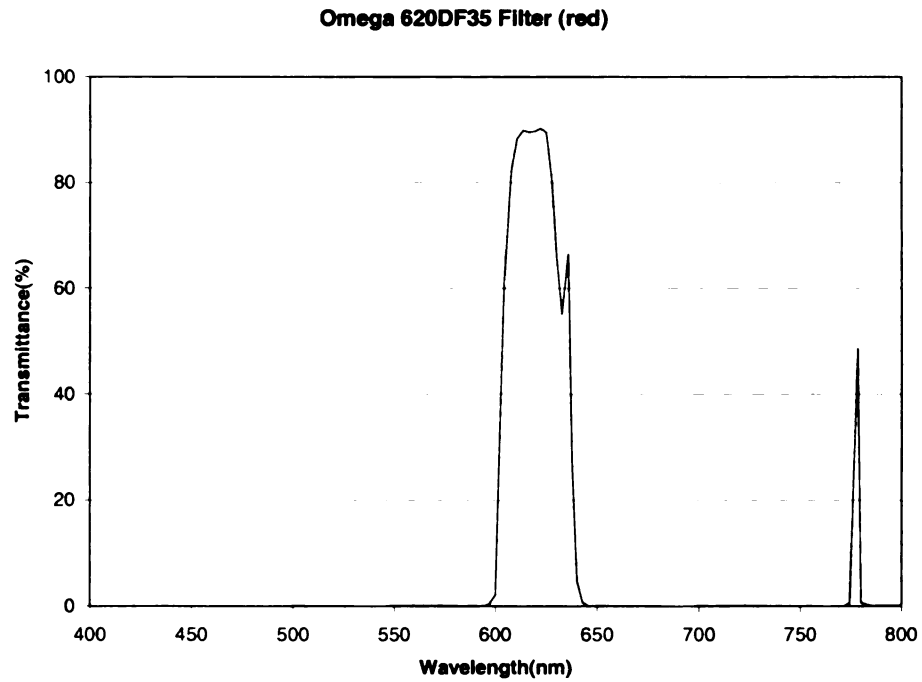
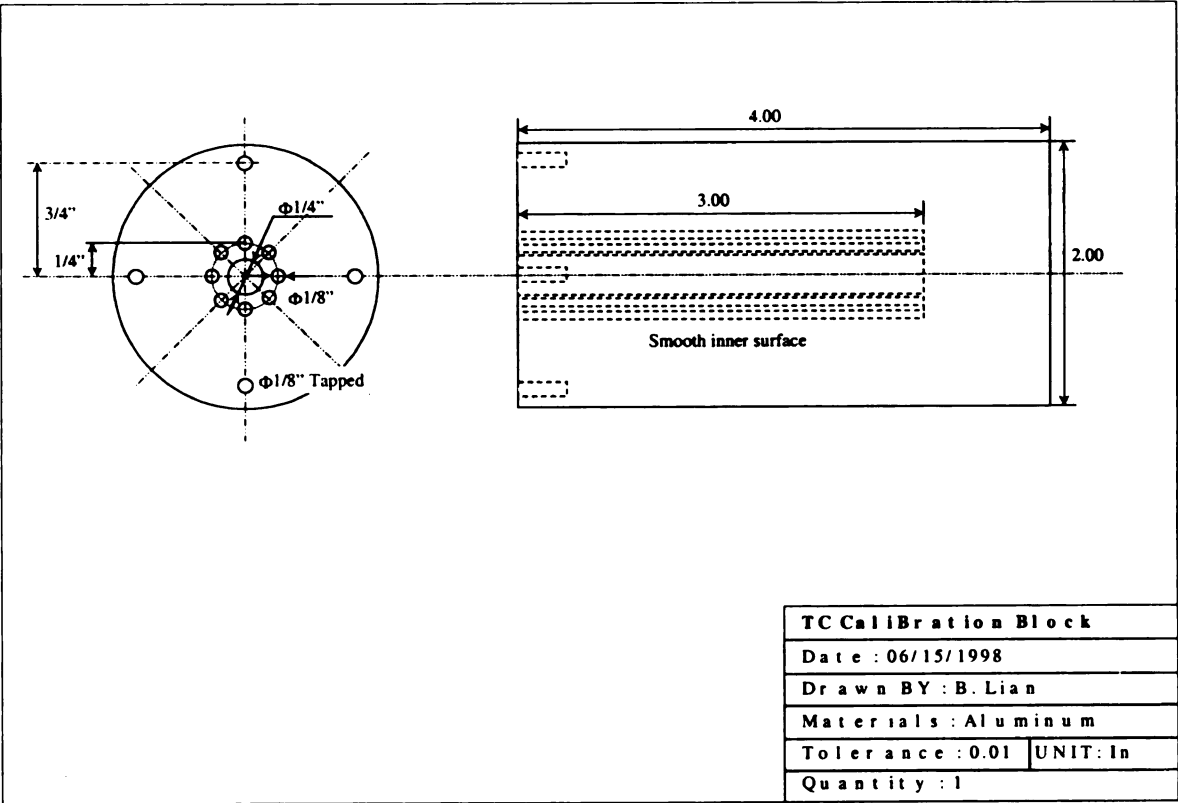


Figure 68. Spectral Transmittance of Red Filter (620nm).

APPENDIX H

Calibration Block for Thermocouples



APPENDIX I

Software User's Guide


FERIT – An Imaging, Temperature Rendering and Visualization Software




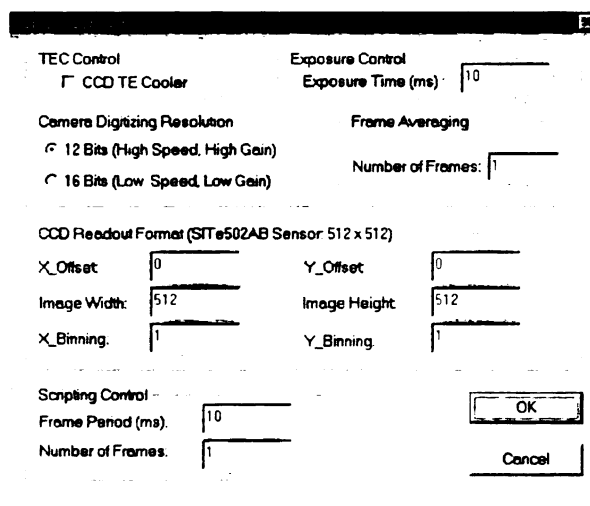
As an integral part of the FERIT system, a Microsoft Windows-based application software program was developed to accomplish camera control, imaging, data acquisition and digital I/O, measurement, temperature rendering, and visualization.

The software was created with Microsoft Visual C++ and features a multi-document graphic user interface. Supported operations are grouped according to their functionality:

- (1) File Handling: Similar to most Windows applications, the software support common file functions such as **New, Open, Save, Save As..., Close, Print, Print Previews, Print Setup** and **Exit**. The software implemented Tagged Image File Format (TIFF) as its internal file format which makes it possible to use other image processing software such as Image-Pro Plus to manipulate images created by FERIT. The resolution can be set to 12 or 16 bit.
- (2) Camera Control: The cooled digital camera must be initialized before it can be used to take images. This is accomplished by selecting the **Initialize**


command under the **Camera** menu or by pressing the quick access button .

After initialization, the camera should be configured for the operating parameters: Cooler On/Off, Resolution 12/16 bit, Exposure Time (in ms), Frame Averaging, Image Format/Size, Offsets, Binning, Multi-frame Acquisition. Select **Config** under the **Camera** menu or press the corresponding quick access button , to activate the Configuration panel:







The software will perform an automatic range check for the parameters such as image size, and a warning will be given if they are out of bounds or a negative value is entered.


(3) Imaging:

Imaging can be performed in single frame mode or multiple frame mode. To obtain a single image, select **Acquire** under the **Image** menu or press the quick access button . If the *Number of Frame*

variable in the *Frame Averaging* option box is greater than one, the camera will acquire the specified number of images and return the averaged result as a single frame.

For FERIT specific application (thermography), a scripting mode is provided to help the user to step through the required steps: acquiring background image, acquiring the reference image, starting sequence. The steps are accomplished by selecting commands under the **Script** menu. For background image, select **Background** command under the menu or press the  button. For reference image, select **Reference** command under the menu or press the  button. To start the measurement sequence for the experiment, select **Start Sequence** or press the  button. This will bring up a dialog to confirm the action. Press the **Start** button in the dialog box to start the acquisition.

(4) Temperature: After the images have been acquired (bg.tif, ref.tif, image##.tif), the temperature distribution can be obtained using the temperature rendering commands. The punch sign denotes the index of the image acquired at a specified moment. With at least the above three files opened, the temperature corresponding to image##.tif can be converted to temperature. The **Settings** command under the **Process** menu (or the  button) allows the user to input the


reference temperature and the desired temperature range to be displayed. Temperature Conversion can be activated by the Temperature command under the Process menu (or the  button) and a new image containing the thermographic information will be created (therm##.tif). To view a temperature, select **Temperature** under the **View** menu.

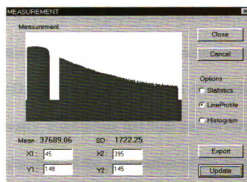
(5) View: Several visualization modes are provided, which **includes Gray Scale**, pseudo **Color** (green-yellow-red), **Default** (no 16 to 8 bit conversion, useful to get higher frame rate), and **Temperature** for viewing the temperature distribution. The temperature is represented internally as 16 bit data (to comply with TIFF file format) which is related by the following equations:

$$\text{Intensity} = \text{Temperature(C)} * 100 + 32767;$$

$$\text{Temperature} = (\text{Intensity} - 32767) / 100.0.$$

(6) Measurement: Two measurement methods are provided with the software. A single point measurement is given in the status bar (at the bottom portion of the application window) which indicates the intensity or temperature (depending on the View mode) at the location of the mouse pointer. A more advanced measurement tool is also provided to facilitate intensity and statistical measurements for a line profile and an area of interest. The measurement template can

be activated by selecting the **Measurements** command under **Process** menu (or using the  button):



Measurement modes (Statistics, Line-Profile, and Histogram) can be selected by clicking the selection buttons. Coordinates of two end points are defined in the four editable input fields. The measurement can be performed by pressing the **Update** button. The statistical measurement results (average, standard deviation) will be displayed below the plot area. After the measurement has been updated, the results can be output to an external ASCII file “output.txt”. For example, if the measurement mode is Line-Profile, the value of pixels along the line segment connecting the two specified end points will be exported as a column of numbers. If the Mode is set to Statistics, the pixel values within the rectangle defined by the two end points will be exported as a two dimensional matrix. The **Close** button will save the current

measurement configuration so that they can be used in future measurements without the need to re-enter them.

(7) DAQ Control: The software also provides control for extra hardware such as data acquisition and temperature measurement. The commands under the **DAQ** menu can be used to activate the simultaneous UV intensity monitoring function and an output digital pulse to control the duration of the application of the heating source.

TCDAQ – A Temperature Measurement Virtual Instrument

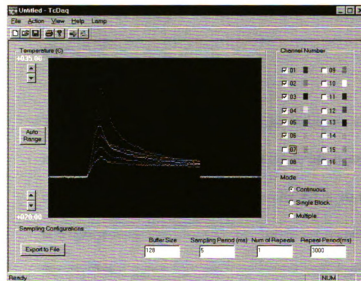


Since temperature measurement using thermocouples is necessary in order to conduct calibration and provide reference temperature, a Windows-based software TCDAQ.EXE was developed to integrate data acquisition and temperature measurement hardware (CIO-DAS802/16 and CIO-EXP16) and software library (Cbw32.dll), as well as to provide visualization for the acquired data.

The CIO-DAS802/16 and CIO-EXP16 boards (from Computerboards) are both needed to conduct temperature measurement. The CIO-DAS802/16 is a data acquisition board with 8 input channels and four digital output channels. The CIO-EXP16 is an extension board with on-board amplifier and cold junction compensation (CJC) sensor for temperature measurement which it has 16 inputs. The four digital lines of the CIO-DAS802/16 select

which input channel to read by sending digital controls to the multiplexer on the CIO-EXP16. The thermocouple and CJC outputs occupy two of the eight inputs to the CIO-DAS802/16 (channel 7 and 8, they can be re-configured by rearranging the jumpers on the extension board CIO-EXP16) and reading from the corresponding input channels.

The software was created with Microsoft Visual C++ and features a single-document graphic user interface. Supported operations are fairly straightforward since the application interface emulates a virtual instrument:



- (1) File Handling: Instead of implementing an internal data structure to represent temperature, an export function was incorporated to output ASCII format data since they are readily read by data processing software such as Excel.

(2) Display Area: Data being measure or previously measured are display in the display area as colored pixels. The display upper and lower temperature ranges are shown in the top and bottom left of the plot area. Two display modes are supported, the auto or manual range. In the Auto-Range mode, the software checks the maximum and minimum values of the acquired data in the buffer and appropriately changes the display range so that all data will fit in the display area. In the Manual-Range mode, the range can be changed manually using the buttons near the numeric range displays. The triangle within the button indicates the direction of change.

(3) Channels: The CIO-EXP16 extension board has 16 inputs which are reflected in the channel selection area in the application software. A channel can be activated by clicking in the checkbox so that a check mark is displayed for that channel. To deactivate a channel, simply click the checkbox again and the check mark will disappear, which will terminate the measurement and display for that channel. A warning message will be given if the user is trying to start the acquisition without specifying at least one input channel.

(4) Modes: Three measurement modes are provided: Single block, Continuous, and Multiple-Blocks.

In the Single Block measurement mode, the application will not return and the results will not be displayed until the specified number of data points has been obtained. A message box will notify the user that the acquisition is completed.



In the Continuous mode, data acquisition and display are concurrent so the acquisition rate is limited. The software uses a circular buffer to hold the data which means it will over-write the beginning of the buffer if it reaches the end of it. All the data in the buffer will be output starting from the most recently acquired ones, if the **Export** button is pressed.

In the Multiple-Blocks mode, the software will acquire a block of data at the specified rate, and will wait for a specified amount of time before starting to acquire another block of data, until the specified number of blocks of data has been obtained. This feature is useful for repeated measurements such as long term stability analysis.

(5) Configuration: The parameters for acquisition are controlled by the user inputs for acquisition rate, buffer size (number of samples), number of

multiple blocks, and multiple block interval which are located in the lower right corner of the interface. For multi-channel acquisition, the sampling rate is for all channels, saving the user the effort of calculating the actually rate if the rate is per channel based.

(6) Export: The export file is in ASCII format so that it can be imported to other programs for further analysis. At the beginning of the file is information regarding the acquisition parameters such as sampling rate and number of samples. Data are listed as columns with channel number indicted at the beginning of each column. In multiple blocks mode, there is a blank line separating two blocks of data and each block of data is marked by a block number at the beginning of that block.

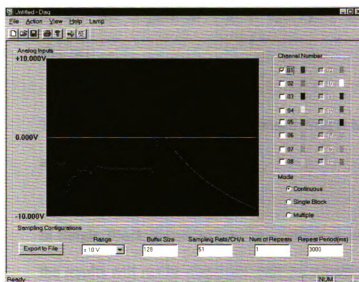
(7) Action Control: Two simple action controls are provided to control the acquisition: Start and Stop. The Start command under Action menu or the  button can be used to initiate an acquisition. The Stop command under the Action menu or the  button is used to stop a continuous acquisition at any time.

DAQ – A General Purpose Data Acquisition Virtual Instrument



This program is very similar to the TCDAQ program except that it is a general purpose data acquisition instrument which will work with CIO-DAS802/16. It can read 8 analog input channels and has 4 digital input/output lines. In our application, its first channel was used to measure UV excitation fluctuation with the integrated photodiode and amplifier (OPT301M).

The software was created with Microsoft Visual C++ and it features a single-document graphic user interface. Supported operations are fairly straightforward since the application interface emulates a virtual instrument:



(1) File Handling: Instead of implementing an internal data structure to represent temperature, an export function was incorporated to output ASCII format data since they are readily read by data processing software such as Excel.

(2) Display Area: Data being measured or previously measured are displayed in the display area as colored pixels. The display ranges are shown in the top and bottom left of the plot area.

(3) Channels: A channel can be activated by clicking in the checkbox so that a check mark is displayed for that channel. To deactivate a channel, simply click the checkbox again and the check mark will disappear, which will terminate the measurement and display for that channel. A warning message will be given if the user is trying to start the acquisition without specifying at least one input channel.

(4) Modes: Three measurement modes are provided: Single block, Continuous, and Multiple-Blocks.

In Single Block measurement, the application will not return and the results will not be displayed until the specified number of data points has been obtained. A message box will notify the user that the acquisition is completed.

In Continuous mode, data acquisition and display are concurrent so the acquisition rate is limited. The software uses a circular buffer



to hold the data which means it will over-write the beginning of the buffer if it reaches the end of it. All the data in the buffer will be output starting from the most recently acquired ones, if the **Export** button is pressed.

In Multiple-Blocks mode, the software will acquire a block of data at the specified rate, and wait for a specified amount of time before starting to acquire another block of data, until the specified number of blocks of data has been obtained. This feature is useful for repeated measurement such as long term stability analysis.

(5) Configuration: The parameters for acquisition are controlled by the user inputs for ranges, acquisition rate, buffer size (number of samples), number of multiple blocks, multiple block interval, which are located in the lower right corner of the interface. For multi-channel acquisition, the sampling rate is for all channels, saving the user the effort to calculate the actually rate if the rate is per channel based.

(6) Export: The export file is in ASCII format so that they can be imported to other programs for further analysis. At the beginning of the file is information regarding the acquisition parameters such as sampling rate and the number of samples. Data are listed as columns with channel number indicted at the beginning of each column. In

multiple blocks mode, there is a blank line separating two blocks of data and each block of data is marked by a block number at the beginning of that block.

(7) Action Control: Two simple action controls are provided to control the acquisition: Start and Stop. The Start command under Action menu or the  button can be used to initiate an acquisition. The Stop command under the Action menu or the  button is used to stop a continuous acquisition at any time.

APPENDIX J

Instructions for Temperature Measurement with FERIT

1. Arrange instrument hardware (camera, UV source, sample, DAQ box, Lamp). Make sure the camera head and UV lamp housing are securely placed.
2. Check connections of all equipment: (1) **camera**: power to TEC control unit, TEC control unit to camera head, camera head to PC control card, PC control card to camera head; (2) **UV source**: connection from lamp housing to 1600 power supply, power cable to 1600 power supply; (3) **DAQ**: 37 pin connection between CIO-DAS802/16 and CIO-EXP16, thermocouple connection to CIO-EXP16 if needed, connection to digital output from CIO-EXP16 (Heating source control) and analog input to CIO-EXP16 (UV monitoring) if needed; (4) **Heating Source**: power to halogen lamp or other heating source for NDE type of application.
3. Place the UV filter/adaptor in front of the UV source and an absorbing block in front of the adapter. Power up the lamp, turn the adjustment knob of the condenser lens to change the spot size so that uniform illumination is obtained across the sample surface. The spot size can also be adjusted by moving the lamp housing towards or away from the sample. The lamp usually needs 40 minutes to one hour to become stable. Block the UV illumination when the adjustment is completed.
4. Start FERIT.EXE and power up the TEC unit. From the Configuration panel of FERIT, turn on the cooler and set the exposure time to minimum (10 ms, default). Check the lens to the camera head and confirm that the red filter is properly installed,

open the aperture control (IRIS) to maximum (1.4) to allow maximum signal throughput. Adjust focus of the system by taking a few snapshots of the sample surface, adjust the sample location or focus if necessary. The camera usually requires approximately 20 minutes to stabilize.

5. Switch off room light and other ambient light sources. Open the UV source, and acquire an image. If the signal strength is too low, increase the image intensity gradually by changing the exposure time setting in the Configuration panel so that the maximum signal is about 70%~80% of full scale. Block the UV source.
6. Set appropriate imaging parameters (frame averaging, image format, multi-frames).
7. Set analog and digital controls with the DAQ menu to enable UV excitation monitoring, heating duration, and switch on power to the DAQ box.
8. Acquire background image (without UV).
9. Acquire reference image (with UV).
10. Start heating/cooling of test structure to induce fluorescent emission intensity change, and heating pulse if needed.
11. Start acquiring image sequence at specified time interval.
12. Save all files.
13. With bg.tif and ref.tif opened, set temperature conversion parameters (reference temperature, display range), select image of interest (image##.tif), activate conversion. Select View Temperature to visualize temperature distribution. Save the created thermographic files (therm##.tif).
14. After the test is completed, switch off the UV power but wait at least ten minutes before disconnecting its power cord to allow for discharging. Turn off TEC cooling

from the Configuration panel (but not the power switch on the back of the TEC control unit), wait until the TEC reading get back to room temperature and turn the power of the TEC control unit off. This precaution will keep the cooling fan running to prevent rapid temperature change of the CCD sensor since the camera head is very hot and the CCD sensor is very cold at the end of usage.

BIBLIOGRAPHY

Bibliography

1. Jacobs H.R. and Hartnett J.P. (Editors), "Thermal Engineering: Emerging Technologies and Critical Phenomena", Workshop Report, CTS-91-04006, 1991.
2. Hudson, R.P., "Thermometry", Encyclopedia of Physics, VCH Publishers, Inc., edited by Lerner, R.G. and Trigg, G.L., 1991, pp. 1272-1276.
3. Brager, S.D., "IR Temperature Measurement Fundamentals", Measurements and Control, Sept. 1995, pp172-181.
4. Lerner E.J., "Infrared Detectors Offer High Sensitivity", Laser Focus world, June, 1996, pp155-164.
5. Wallin B., "Solving Temperature Measurement Problems in PCB Inspection", Photonics Spectra, March 1990, pp167-170.
6. Merchant J., "Blackbody Calibration Sources Function as Standards", Laser Focus World, April 1995, pp105-110.
7. Lerner E.J., "Infrared Array Detectors Create Thermal Images", Laser Focus world, September, 1996, pp105-110.
8. Sarath Gunapala,, Mani Sundaram, Sumith Bandara, "Quantum Wells Stare at Long-Wave IR Scenes", Laser Focus World, June, 1996, pp. 233- 240.
9. Santa Barbara Research Center (SBRC), "SBRC: Technological Innovations", http://www.sbrc.com/tech_innovations.html, 1999.
10. Abuaf N. et al., "Convection Thermography", Technical Information Series, September, 1985.

11. Simonich J. C. and Moffat R. J., "New Technique for Mapping Heat Transfer Coefficient Contours", Rev. Sci. Instr., Vol. 53, No. 5, May, 1982, pp678-683.
12. Akino N., et al., "Improved Liquid Crystal Thermometry Excluding Human Color Sensation", Journal of Heat Transfer, Vol. 111, May 1989, pp558-565.
13. Akino N., Kunugi, T., Shiina, Y., Ichimiyia K., Kurosawa A., "Fundamental study on Visualization of Temperature Fields Using Thermosensitive Liquid Crystals", Proceeding of the Fifth International symposium on Flow Visualization. Pp.87-92, august 21-25, 1989, Prague.
14. Moffat, R.J., 1990, "Experimental Heat Transfer, Keynote Paper", KN11, Proceeding of 9th International Heat Transfer Conference", Jerusalem, Israwl, Vol. 1, pp. 187-205.
15. Simonich J. and Moffat R., "New technique for mapping heat transfer Coefficient Contours", Rev. Scientific Instruments, Vol. 53, No. 5, May, 1982.
16. Urbach, F., "Measurement of Temperature Distribution on the Surface of Solid Bodies", U.S. Patent No. 2,551,650, May 8, 1951.
17. Bradley, L.C., "A Temperature-Sensitive Phosphor Used to Measure Surface Temperature in Aerodynamics", Rev. Sci. Instr., Vol. 24, 1953, pp.219.
18. Brenner, D.J., "A Technique for Measuring the Surface Temperature of Transistors Using Fluorescent Phosphor", NBS Tech. Note, No. 591, 1971.
19. Kolodner P. and Tyson A., "Microscopic Fluorescent Imaging of Surface Temperature Profile with 0.01°C Resolution", Applied Physics Letters, Vol. 40, No. 9, May, 1982.

20. Kolodner P. and Tyson A., "Remote Thermal Imaging with 0.7 μ m Spatial Resolution Using Temperature-Dependent Fluorescent Thin Films", *Applied Physics Letters*, Vol. 42, No. 1, May, 1983.
21. Wickersheim K.A. and Alves R.B., "Recent Advances in Optical Temperature Measurement", *Industrial Research and Development*, December 1979, pp82-89.
22. Wickershelm K. and Mei S., "Phosphor and Fiber Optics Remove Doubt from Difficult Temperature Measurements", *Research and Development*, November, 1985, pp114-119.
23. Bizzak D. and Chyu M., "Rare-Earth Phosphor Laser-Induced Fluorescence Thermal Imaging System", *Reviews of Scientific Instruments*, 65(1), January, 1994.
24. Liu T., Campbell, B.T. and Sullivan J.P., "Fluorescent Paint for Measurement of Heat Transfer in Shock – Turbulent Boundary Layer Interaction", *Experimental Thermal Fluid Science*, vol. 10, 1995, pp101-112.
25. Barton D. and Tangyungyong P., "Fluorescent Microthermal Imaging - Theory and Methodology for Achieving High Thermal Resolution Images", *Microelectronic Engineering*, Vol. 31, February, 1996, pp271-279.
26. Tangyungyong P. And Barton D. L., "Photon Statistics, Film Preparation and Characterization in Fluorescent Microthermal Imaging", unpublished work, 1995.
27. Crofcheck C. and Scranton E., et al., "Temperature Sensitive Luminescence of Tris(b-diketone) Europium Chelates For Monitoring High Speed Cationic Photopolymerization", *Journal of Polymer Science, Polymer Chemistry*, 1994.

28. Nelson E.W., Carter T.P. and Scranton A.B., "Fluorescence Monitoring of Cationic Photopolymerizations: Divinyl Ether Polymerizations Photosensitized by Anthracene Derivatives", *Macromolecules*, Vol. 27, 1994, pp1013-1019.
29. Halverson F., Brinen J.S., and Leto J.R., "Luminescence of Europium Hexafluoroacetylacetonate", *The Journal of Chemical Physics*, Vol. 40, (10), May 1964, pp. 2790-2793.
30. Sager W.F., Filipescu N., Serafin F.A., "Substituent Effects on Intramolecular Energy Transfer. I. Absorption and Phosphorescence Spectra of Rare Earth β -Diketone Chelates", *The Journal of Physical Chemistry*, Vol. 69, (4), April 1965, pp. 1092-1100.
31. Simons A.J., McClean I.P. and Stevens R., "Phosphors for Remote Thermograph Sensing in Lower Temperature Ranges", *Electronics Letters*, February 1996, Vol. 32 No. 3, pp253-254.
32. Cheryl Caffrey, Master Thesis, "Digitized Fluorescent Film Thermography", East Lansing, Michigan State University, 1994.
33. Bhaumik M.L., "Quenching and Temperature Dependence of Fluorescence in Rare-Earth Chelates", *The Journal of Chemical Physics*, Vol. 40, No. 12, June 15, 1964, pp3711-3715.
34. Wicks, Z.W., Jones F.N., Pappas S.P., "Organic Coatings: Science and Technology", Wiley-Interscience Publication, Vol. II, 1994, pp.65-81.
35. J. D. Ingle, Jr., S. R. Crunch, "Spectrochemical Analysis", Prentice-Hall, 1988, pp.438-458.

36. Drexhage K.H., Kuhn H. Shafer F.P., Bunsenges. Phys. Chem., Vol. 72, 1968, pp. 329.
37. Alivisatos A.P., Waldeck D.H., Harris C.B., "Non-classical Behavior of Energy Transfer from Molecules to Metal Surfaces: Biacetyl($^3n\pi^*$)/Ag(111)", Journal of Chemical Physics, 82(1) 1, January 1985, pp. 541-547.
38. Chance R.R., Prock A., Silbey R., "Molecular Fluorescence and Energy Transfer Near Interfaces", Advances in in Chemical Physics, vol. 37, 1978, pp. 1-65.
39. Kurczewska H. And Bassler H., "Energy Transfer Across an Anthracene-Gold Interface", Journal of Luminescence, Vol. 15, 1977, pp. 261-266.
40. SpectroSource Instruments, Inc. "CCD Imaging System Installation and User's Guide", 1998.
41. David J. Kruglinski, "Inside Visual C++, version 5", Microsoft Press, 1997.
42. Incropera F. P. and DeWitt D. P., "Introduction to Heat Transfer", Wiley, New York, 1990.
43. Nordling C. and Osterman J., "Physics Handbook", Chartwell-Bratt, 1980.
44. Chance R.R., Prock A., and Silbey R., "Molecular Fluorescence and Energy Transfer Near Interface", Advance in Chemical Physics, Vol 37, 1978, pp. 1-65.
45. Siegel R. and Howell J.R., "Thermal Radiation Heat Transfer", third edition, Hemisphere Publishing Corporation, 1992, pp. 118-130.
46. Hoke P. B., "Experimental Measurement of The Slit Response Function and Corrected Infrared Thermographic Measurements", Master's Thesis, Michigan State University, East Lansing, 1998.

MICHIGAN STATE UNIVERSITY LIBRARIES



3 1293 02334 8174